Universität Hamburg

Experimental Application of QCD Antennas

Diplomarbeit am Institut für Experimentalphysik
Department Physik
Universität Hamburg

von

Sergei Bobrovskyi

Betreuer:

Prof. Dr. Peter Schleper
JProf. Dr. Johannes Haller

27. März 2009

Zusammenfassung

Untergrund durch QCD-Multijet-Ereignisse ist eines der ernstzunehmenden Probleme bei der Suche nach Neuer Physik am LHC. Die vorliegende Arbeit wendet zum ersten Mal den Formalismus der auf der SPHEL Näherung der QCD Matrixelemente basierenden QCD Antennen Variablen auf experimentell rekonstruierte Jets zwecks Unterscheidung zwischen QCD und supersymmetrischen Prozessen an. Die neuen Observablen liefern, im Vergleich mit den herkömmlichen Event Shape Variablen, ergänzende Informationen über die Struktur der Ereignisse. Trotz Korrelation mit der experimentell bestimmten fehlenden transversalen Energie, können die Variablen zur Verbesserung des Signal zum Untergrund Verhältnisses verwendet werden.

Abstract

A serious problem in searches for new physics at the LHC is the rejection of QCD induced multijet events. In this thesis the formalism of QCD antenna variables based on the SPHEL approximation of QCD matrix elements is applied for the first time on experimentally reconstructed jets in order to discriminate QCD from supersymmetric processes. The new observables provide additional information with respect to traditional event shape variables. Albeit correlated with experimentally measured missing transverse energy, the variables can be used to improve the signal to background ratio.

Contents

Introduction

The Standard Model of particle physics (SM) remains unmodified as the underlying theory of the microcosm for more than 30 years. No high energy physics experiment carried out so far, has found a contradiction to the predictions of the SM. However, the SM is by construction incomplete and cannot be the truly fundamental theory of everything, since the gravitational interaction is not taken into account. Furthermore, the astrophysical observations of the last decades revealed the existence of new matter (the so called dark matter, proposed already in the 30'th) and energy content (the so called dark energy) of the universe, which cannot be explained by the standard model.

The tension between the lack of the direct evidence from the high energy experiments and the theoretical certainty that the SM should be extended to include gravity and other phenomena, led to new theories, which are not only unsupported by experimental evidence, but are probably not even falsifiable. This situation provoked some physicists to speak about the "crisis in fundamental physics" [1, 2].

The situation can change this fall, with the start of the operation of the Large Hadron Collider (LHC) a proton-proton accelerator at CERN - the European laboratory for elementary particle physics. The LHC centre of mass energy of 14 TeV[1] enables the exploration of the physics at the TeV scale. Theoretical arguments [3] suggest that new evidence for the physics beyond the SM should be found at this scale.

Supersymmetry (SUSY) is the most promising extension to the SM providing a natural dark matter candidate. It introduces furthermore additional heavy particles, which should be found at the TeV scale, since otherwise the SUSY would lose the desired properties.

The CMS experiment is one of the two general purpose particle detectors at the LHC. Besides the search for the last missing element of the SM, the Higgs boson, CMS searches for physics beyond the SM, in particularly for SUSY. There are many different possibilities how SUSY can be realised. A popular model is based on the minimal supergravity (mSUGRA) with R-parity conservation. The new processes

---

[1]This thesis uses natural units: $\hbar = c = 1$.

and particles predicted by this model could be first discovered in CMS SUSY searches based on the signature of large missing transverse energy and high p_T jets [4, 5].

Multijet processes due to strong interaction are one of the largest backgrounds for SUSY searches in the all-hadronic channel mentioned above. Although considerable research has been devoted to the suppression of the various backgrounds, rather less attention has been paid to the possible discrimination between supersymmetric and strong processes, based on their different theoretical characteristics.

This thesis investigates the characteristics and the possible fields of use of discriminating variables, whose definitions are motivated by the theoretical knowledge of the structure of tree-level scattering amplitudes with many final state partons due to the strong interaction. These variables are called antenna variables, and they are sensitive to the topology of the momenta and to the invariant masses present in the event.

As an example of use the antenna variables are applied to the SUSY searches in the all-hadronic channel. It will be presented how the characteristics of these variables change after the correlations with other discriminating variables like missing transverse energy are taken into account, and how these variables can improve the understanding of the difference in the topological aspects of the supersymmetric and the strong processes.

This thesis starts with the summary of the SM in the chapter 2, with emphasis on the theory of the strong processes. A short introduction to supersymmetry is given in the following chapter 3. After an overview of the CMS experiment in the chapter 4, the computational tools used in the present approach are reviewed in chapter 5. Chapter 6 deals with the description of the strong processes at hadron colliders, in particular with the approximative description of the tree-level scattering amplitudes, which is the basis of the variable definition presented in chapter 7. This chapter compares the distribution of the variable computed from the simulated events to the theoretical prediction for the case of the $gg \rightarrow gg$ process. Furthermore the effects of jet reconstruction and resolution on the antenna variables are examined. Chapter 8 deals with the possible use of the variable for the discrimination between SUSY and strong interactions in the all-hadronic channel. The thesis will finish with a conclusion and an outlook.

1

The Standard Model

The Standard Model of particle physics (SM) is a physical theory of the microcosm formulated in the framework of quantum field theory (QFT). The realm of the SM are elementary particles which are considered to be fundamental building blocks of matter and interactions between them. The SM describes three of four empirically known forces: the strong, the weak, and the electromagnetic force. Gravitation is excluded, since the General Theory of Relativity (GRT) - the highly successful theory of gravitational interactions - could not be hitherto incorporated in the framework of QFT. The SM consists of two parts: Quantum Chromodynamics (QCD) as the theory of the strong interaction and Weinberg-Salam theory as the theory of the electroweak interaction.

No effect contradicting the predictions of SM have been found so far, the agreement between theoretical and experimental values is often even amazingly good. The paradigmatic example is the magnetic moment of the electron: the discrepancy between calculated and measured value occurs at the tenth decimal place [6]:

$$\left(\frac{\mu}{\mu_0}\right)_{theo} = 1.0011596524460(127)(75), \tag{1.1}$$

$$\left(\frac{\mu}{\mu_0}\right)_{exp} = 1.001159652200(40). \tag{1.2}$$

The errors of the theoretical value are due to the uncertainty of the fine-structure constant (127) and due to the numeric inaccuracy in the computations of the coefficients of the perturbation series.

In spite of this success, the SM reveals many shortcomings rooted either in the conceptual background of QFT or in the aesthetic considerations and requirements imposed on it. This chapter provides a very short introduction to QFT and to the Standard Model with particular emphasis placed on QCD, since it is the part of the SM relevant for this work.

1.1   Quantum field theory

There is no single agreement upon a standard formulation of QFT [7], and there is even no standard definition what quantum field theory precisely is [8]. A certain perspective could be the statement that QFT *aims* at a synthesis of quantum physics with the principles of classical field theory, in particular the principle of locality [9].

The basic starting point are the axioms of Special Relativity (SRT) and the axioms of Non-relativistic Quantum Mechanics (NRQM) which should be combined in one theory. If one proceeds further along this line of thought one arrives at axiomatic approaches to QFT in which fundamental physical principles any QFT should obey are stated, and attempts to explicitly build models according to these principles are made. A possible set of axioms for a quantum theory of *fields* could be [10]:

- Space-time is a classical manifold with the geometry of Minkowski space $\mathcal{M}$. Its symmetry group is the "Poincaré group", generated by translations and Lorentz transformations.

- Pure states are described as "rays" in a Hilbert space $\mathcal{H}$, equipped with a positive definite inner product. Observables are self adjoint operators acting in $\mathcal{H}$. (This axiom ensures the superposition principle for quantum states and the probabilistic interpretation of expectation values.)

- A symmetry is implemented by a "ray representation" of the symmetry group. In the case of the Poincaré group $\mathcal{P}$ this is equivalent to a representation of the covering group $\tilde{\mathcal{P}}$ by unitary operators. (From this axiom follows, that for instance infinitesimal generators of translations P^μ may be interpreted as observables corresponding to the total energy-momentum. Furthermore, an irreducible representation with positive energy describes the state space of a single stable particle.)

- The spectrum of the energy-momentum operators P^μ in $\mathcal{H}$ is restricted to the closed forward cone $\bar{V}_+ = \{p : p_0 \geq |\mathbf{p}|\}$. There is a unique ground state Ω, the vacuum.

- The basic dynamical variables, in terms of which all operators in $\mathcal{H}$ should be expressed, are fields. (A field is an "operator valued distribution" on a suitable defined domain in $\mathcal{H}$.)

- The theory is completely described by a finite number of covariant fields each having a finite number of components. The notion of fields allows encoding of the relativistic causal structure of space-time in the theory as stated in the next postulate.

- Field quantities in regions which lie space-like to each other either commute or anticommute.

Relying on these axioms powerful global theorems like CPT and the Spin-Statistics theorem could be stated. However, no quantum theory of interacting fields in four dimensional space time have been explicitly constructed so far. It is further unclear whether any *nontrivial* QFT's satisfy the stated axioms, even though all theories constructed in two or three space-time dimensions satisfy them. Hence, the

critical discussion of the fundamental principles is itself an issue of the axiomatic approach [9].

The main approach to QFT treated in all textbooks [11] is perturbation theory based on the idea of "quantisation of a classical field theory". Perturbation theory produces formal power series expansion in a coupling constant. The series should be asymptotic to a QFT yet to be constructed, and therefore the couplings should be weak. The starting point of the scheme is the Lagrangian of classical field theory, which should be separable in a "free" and "interaction" part. In the "canonical approach" field variables and their conjugates are then identified with the canonical variables on which canonical commutation relations are imposed. The Hamiltonian as a functional of the canonical variables in the Heisenberg picture is derived in the next step. Afterwards transition to the interaction picture takes place. Assuming that long time before the interaction ($t \rightarrow -\infty$), and long time after the interaction ($t \rightarrow \infty$) all particles are well separated in space and can be treated as free, a scattering matrix (operator) or S-matrix connecting the asymptotic states is introduced. The S-matrix is an array of complex probability amplitudes for all possible transitions between all "in" ($t \rightarrow -\infty$) and "out" ($t \rightarrow \infty$) states. These states do not inhabit two different Hilbert spaces. They differ only in labelling, hence any "in" state can be expanded as a sum of "out" states, with expansion coefficients given by the S-matrix [12]. The S-matrix is constructed from an Hamiltonian in the interaction picture (essentially being the time-evolution operator in the limit of very large t [11]) and can be computed as a power series[1]:

$$ S = 1 + (-i) \int_{-\infty}^{\infty} dt_1 \, H_I(t_1) + (-i)^2 \int_{-\infty}^{\infty} dt_1 \int_{-\infty}^{t_1} dt_2 \, H_I(t_1) H_I(t_2) + \cdots . \quad (1.3) $$

The introduction of diagrammatic methods like "Feynman diagrams" [13] simplifies the calculation of the terms. It is convenient to single out the part of the S-matrix corresponding to the actual interactions : $S - 1$, and write it as a delta function-free amplitude (or in other words matrix element) $\mathcal{T}$ times other factors (delta function). To link this theoretical quantity with experimental results, differential transition rate (probability for a transition between the states per unit time) per flux - the *cross section* is introduced. The cross section is proportional to the absolute square of the matrix element : $|\mathcal{T}|^2$.

While the leading order results for the matrix elements are in good agreement with experiments, there is a need to "renormalise" the single higher terms of the expansion which would lead to infinities otherwise. This procedure fixes the parameters of the theory to their physical values, since "bare" values appearing in the Lagrangian are not measurable but only the sum of these values and all radiative corrections. The renormalisation should be achieved without the introduction of infinitely many new parameters, since all predictive power will be lost otherwise. This necessity restricts the form of the Lagrangian. Experiments have revealed the relevance of vector (spin 1) couplings : Parity violation in the weak interactions can be explained by a V-A (Vector-Axialvector) but not by scalar and tensor couplings [14, 15]. The idea that vector couplings are mediated by vector fields lies at the basis of the SM. It can be shown, for example in [16], that the only successful way to incorporate

---

[1]The treatment in this section is brief and simplified. It provides a basis for a further discussion of the SM.

vector fields into a perturbative QFT is to treat them as gauge fields, with couplings which are necessarily gauge couplings. Thus the gauge principle enters QFT through the inherent limitations of the perturbative scheme. However, gauge invariance forbids explicit mass terms of the gauge bosons and introduces unphysical degrees of freedom. The first problem was solved by introducing a spin-0 Higgs field with "spontaneous symmetry breaking", while for the latter an explicit gauge has to be chosen or general advanced methods (BRST theory) have to be used.
Predictions of perturbative QFT are in a good agreement with the data, as it was outlined in the introduction to this chapter.

In spite of the success of perturbative QFT, which is the foundation of the SM, the theory is not fully consistently completed, and comparison with experiments relies often on heuristic considerations with unsettled correctness [6]. It is possible that the power series is not an asymptotic expansion of the full theory as it could be shown for a low-dimensional model [7, 17–19]. This could be the case for Quantum Electrodynamics (QED) - a QFT model of pure electrodynamic interactions, which can be separated from the SM. On the other hand the field concept itself is problematic in the quantum case, since contrary to the classical physics the fields are not observable, it is impossible to associate each field with a particle species in general case (many auxiliary fields are introduced merely as a tool to quantise classical theory), and quantum fluctuations of localised observables (vacuum expectation values of field products) diverge in the limit of pointlike localisation [9]. Thus the statement that QFT is necessarily a quantisation of a classical field theory is questionable.

The problems mentioned here will be discarded in the following sections which will introduce the SM. But it is important to know that they exist, since the failure of the axiomatic approach up to now may indicate either that the problems with the SM and gravity lie deeper in the foundations of NRQM or even SRT or that the space-time has a lattice-structure. This section shows how the formalism (like Lagrange densities) which will be introduced in the following sections fits into the framework of QFT.

1.2   Gauge theories

To avoid "action at a distance" local interactions with fields were introduced already in classical electrodynamics. For instance the interaction between a relativistic particle and an electromagnetic field is described by an additional term in the action containing the charge of the particle and the vector-potential of the field [20] at a given point. But the vector-potential is an auxiliary quantity and is not observable, since it can be altered by a four gradient of a scalar function which depends on space and time coordinates. This additional term leads to a total derivative in the action leaving the equations of motion invariant. This symmetry called "gauge symmetry" is a redundancy in the description and the states related by (local) gauge transformations are to be identified. As it was stated in the previous chapter experiments suggested that vector fields are responsible for weak interactions, and the only way to incorporate them into perturbative QFT is to treat them as gauge fields analogous to the vector potential in electrodynamics. To quantify the last statement spin-one fields $A_\mu^a(x)$, where μ is the Lorentz index and a counts the number of field types $a = 1, \ldots, N_V$, have to be examined. First of all, the energy (Hamiltonian) in the

classical theory should be bounded from below and as a result of this demand *every* vector field theory must have at high energies and momenta Lagrangians as given by the following eq. 1.4 (full derivation can be found in [16]):

$$\mathcal{L} \rightarrow -\frac{1}{4}F_{\mu\nu}^a F^{a\mu\nu}, \qquad F_{\mu\nu}^a = \partial_\mu A_\nu^a - \partial_\nu A_\mu^a. \qquad (1.4)$$

But from this form of Lagrangian follows that any field A_μ^a that can be written as a space-time gradient contributes neither to the Lagrangian nor to the Hamiltonian, since $F_{\mu\nu}^a = 0$ in this case. After quantisation such fields would represent particles and forces without energy. To avoid such entities, field replacements of the type:

$$A_\mu^a \rightarrow A_\mu^a + \partial_\mu \Lambda^a(x) + \dots{}^2 \qquad (1.5)$$

should not affect the physical state at all . It follows that a theory with spin-1 fields should be invariant under local gauge transformations, the dimension of the local gauge group being equal to N_V, the number of vector fields present. To ensure renormalisability of quantised theory the gauge theory has to be exact [16].

In order to construct a theory with gauge fields, scalar and spinor fields of the theory, whose excitations will be identified as particles, have to transform as (sets of irreducible) *representations* of some symmetry group under consideration, which means that the fields possess internal degrees of freedom on which the group acts. In case of $SU(n)$ gauge groups one is lead to following transformation property:

$$\psi'(x) = \Omega(x)\psi(x); \qquad \Omega(x) \in SU(n) \qquad (1.6)$$

The gauge fields $A_\mu^a(x)$ are introduced by requiring the possibility of constructing gauge invariant gradients of the spinor and scalar fields above. These gauge fields are $n \times n$-matrices, one for each μ and x. Each $A_\mu^a(x)$ has two suppressed matrix indices. The gradients are constructed with the following ansatz:

$$(D_\mu\psi(x))' = \Omega(x)D_\mu\psi(x), \qquad D_\mu\psi(x) = (\partial_\mu - gA_\mu)\psi(x), \qquad (1.7)$$

g being an arbitrary coupling constant. From the ansatz and the covariance condition for the gradient follows the transformation law of the gauge field:

$$A_\mu' = \Omega(x)A_\mu\Omega(x)^{-1} + g^{-1}(\partial_\mu\Omega(x))\Omega(x)^{-1} \qquad (1.8)$$

The transformation property of the gauge field has the following meaning: The gauge field of a $SU(n)$ gauge theory is a vector field $A_\mu(x)$ with values in the lie algebra **su(n)**. The lie algebra is the tangential space at the identity element of the group: a n-dimensional real vector space with a product structure which is a commutator in the case of matrix groups. The gauge fields transform according to the adjoint representation of the gauge group and receive an additional **su(n)** term if the transformation is local.

To construct the Lagrangian of the gauge theory one has to replace all derivatives by the covariant gradients and add the kinetic term for the gauge fields, which was introduced in the beginning of this chapter, but now with all derivatives being

---

[2]Extra terms not contributing to the bilinear part of the Lagrangian are allowed here.

covariant. The field strength $F_{\mu\nu}$ can be constructed explicitly by computing the commutator of covariant derivatives:

$$F_{\mu\nu} = \frac{1}{g}[D_\mu, D_\nu] = D_\mu A_\nu - D_\nu A_\mu \qquad (1.9)$$

The underlying mathematical structure of gauge theories is the differential geometry of fibre bundles. The gauge fields are connections of some principal bundle and matter fields are sections in associated vector bundles. The strength tensor $F_{\mu\nu}$ is the curvature.

The considerations above lead to following picture: Whenever a field (the discussion dealt only with classical fields so far) possesses an internal symmetry that means a symmetry which is not connected with its space-time coordinates, one has to demand that physical meaningful quantities do not depend on the orientation of the field in the internal space. The orientation in this internal space can furthermore change by an amount that depends on the position in ordinary space (local transformations). For example distinction between the left-handed components of the electron and the electron neutrino (cf. section 1.4.1) can be abandoned by assuming that this components are just different orientations of the underlying entity in the internal space (weak-isospin space). The internal space in this case would be two dimensional and complex, being the fundamental representation space of the group $SU(2)$ responsible for rotations in two complex dimensions. There is one such space (fibre) "above" every space time point, which makes the whole internal manifold a fibre bundle. The classical field is a cross-section since it assigns to every space-time point one orientation in (vector from) each internal space. The derivative should be able to compare fields at different space-time points and to do so it should first parallel transport it from the fibre over the one point to the fibre over the other. The connection enables the parallel transport and transforms the cross-section during it to the orientation in which it would be if it were at the point to which it is transported. The connection hence has its values in the lie-algebra of the symmetry group. It can be expanded in the basis of the algebra, which leads to three fields in the case of $SU(2)$. All linear combinations of these fields are allowed as transformations in the weak-isospin space and associated particles are on an equal footing. One particular combination of the fields has interesting properties: one of this gauge fields rotates upper components of the weak iso-spin into the lower ones (neutrino→electron) the second performs the inverse rotation, while the third component changes nothing but multiplies upper isospin component with 1/2 and the lower with -1/2. These fields resemble the properties of the weak-force. After performing a local $SU(2)$ transformation one will find out that physical quantities build in an appropriate way (all mass terms are forbidden) out of fields and covariant derivatives are left unchanged. Furthermore the $SU(2)$ group acts during this transformation on its own lie-algebra, the lie-algebra being in the adjoint representation. If the group is abelian (e.g. $U(1)$ of electrodynamics) the representation is trivial, but in the non-abelian case interactions among the gauge fields are introduced in their kinetic term. In the $SU(2)$ case one gets second, third, and fourth powers of the gauge fields.

1.3   Spontaneous symmetry breaking

Spontaneous symmetry breaking occurs if the ground state of the QFT is not invariant under a symmetry transformation which leaves the equations of motion invariant.

In this case the ground state must be degenerate, since there is a continuous infinity of the solutions with the same energy, if the considered symmetry was continuous. To build excitations of the ground state which are identified as particles one particular ground state has to be chosen. Once this choice is made and the Lagrangian is expressed in terms of the fields whose quanta correspond to excitations above this vacuum, the original symmetry of the action is no longer manifest - it is *spontaneously broken*. This phenomenon is important to the SM, since gauge symmetry prohibits explicit mass terms of gauge bosons which can be generated only via the Higgs mechanism, that is interconnected with spontaneous symmetry breaking (c.f. next section). If Q is a generator of a symmetry (internal or one of the generators of the Poincaré group) the condition of the symmetry breaking stated above can be rendered more precise: the symmetry is spontaneously broken, unless

$$e^{i\alpha Q} |0\rangle = |0\rangle , \tag{1.10}$$

or equivalently,

$$Q |0\rangle = |0\rangle . \tag{1.11}$$

The symmetry transforms the operators $\mathcal{O}$ acting on the states as,

$$\mathcal{O}' = e^{i\alpha Q}\mathcal{O}e^{-i\alpha Q} \approx \mathcal{O} + i\alpha[Q,\mathcal{O}], \tag{1.12}$$

where the last equality holds for an infinitesimal transformation. If one computes the vacuum expectation value for the change of the operator $\mathcal{O}$ under the symmetry transformation the condition from equation 1.11 becomes:

$$\langle 0| \, i\alpha[Q,\mathcal{O}] \, |0\rangle = 0. \tag{1.13}$$

In QFT dynamical variables $\mathcal{O}$ are field operators. The condition above states that the symmetry is spontaneously broken if one of the field operators transforming non-trivially under this symmetry acquires vacuum expectation value (VEV). Only spin zero fields may acquire a VEV such that the Poincaré invariance is left unbroken.

1.4   The Standard Model

The SM is a non-abelian gauge theory based on the group $SU(3)_C \times SU(2)_L \times U(1)_Y$, with $SU(2)_L \times U(1)_Y$ spontaneously broken to $U(1)_{em}$. Colour $SU(3)_C$ is assumed to be unbroken. The spontaneously breaking of $SU(2)_L \times U(1)_Y$ is due to a VEV of a weak iso-doublet of spin zero fields. The lower indices on the groups refer to the quantum numbers associated with each group. The quantum number is assigned to every particle[3] and corresponds to the representation of the group in which the particle transforms. L stands for weak-isospin, C for colour and Y for the hypercharge ($\frac{i}{3}$ was chosen as basis vector of the lie algebra in this case - this choice can be justified since it allows that the quantum numbers of the particles associated with the unbroken $U(1)_{em}$ are their measured (or postulated) electric charges).

The matter content of the SM (spin-1/2 particles) consists of leptons (from Greek "leptos" for light) which do not take part in the strong interactions and quarks which are strongly interacting, and is organised in 3 generations. Additionally, there is a

---

[3]From here on the notion of fields and particles is used interchangeable if not stated otherwise.

spin-0 Higgs field and one associated massive Higgs boson. Every generation has the same pattern of quantum numbers, but by construction the masses of the particles rise from generation to generation. The first generation is responsible for the non-exotic matter in the universe and contains: electron, electron neutrino, and up and down quarks. The second generation consists of the muon, the muon neutrino, the charm, and the strange quark. The tau lepton and tau neutrino as well as the top and the bottom quark constitute the third generation. The gauge quantum numbers of the first generation and of the Higgs boson are shown in table 1.1.

Field	$SU(3)_C$	$SU(2)_L$	$U(1)_Y$
$L = \begin{pmatrix} \nu_L \\ e_L \end{pmatrix}$	**1**	**2**	-1
e_R	**1**	**1**	-2
$Q = \begin{pmatrix} u_L \\ d_L \end{pmatrix}$	**3**	**2**	$\frac{1}{3}$
u_R	**3**	**1**	$\frac{4}{3}$
d_R	**3**	**1**	$-\frac{2}{3}$
$\phi = \begin{pmatrix} \phi^+ \\ \phi^0 \end{pmatrix}$	**1**	**2**	1

Table 1.1: The first generation of matter fields and the Higgs field with associated Standard Model quantum numbers [3].

1.4.1 Weinberg-Salam theory

Chiral structure is the distinctive feature of weak interactions, which means that they maximally violate parity conservation. To incorporate this structure into the SM, left and right handed components of lepton and quark fields transform in different representations of $SU(2)_L \times U(1)_Y$, the right handed components being not affected by $SU(2)_L$ transformations. Massive spin-1/2 fields obey the Dirac equation which interconnects two Weyl-spinors transforming in different representations of the Lorentz group (c.f. chapter 4.2). If the mass term is set to zero the equation decouples to two Weyl equations each for one of the spinors. Examining the behaviour of the plane wave solutions one finds, that the spin direction of one of the spinors is always antiparallel with respect to the direction of motion - this spinor is called *left-handed* - and vice-versa for the other solution. Dirac equations couples both spinors and one has to use projection operators to get the desired component.

The classical Lagrangian of the Weinberg-Salam Theory is given by

$$\mathcal{L}_{WS} = \mathcal{L}_{gauge} + \mathcal{L}_{matter} + \mathcal{L}_{Higgs} + \mathcal{L}_{Yukawa}, \tag{1.14}$$

where the first term is the kinetic term of gauge fields presented already in the section on gauge theories, the matter term consists of appropriate covariant derivatives of the fields (interactions of matter and gauge fields via minimal coupling), the Yukawa

term describes couplings of leptons and quarks to the Higgs field, and finally the Higgs term consisting of the kinetic part and the Higgs potential:

$$\mathcal{L}_{Higgs} = |D_\mu \phi|^2 + \mu^2 \phi^\dagger \phi - \lambda (\phi^\dagger \phi)^2. \tag{1.15}$$

The last term is needed, since the range of weak interactions (10^{-18} m) is inconsistent with gauge bosons being massless. The masses of weak bosons are generated via the Higgs mechanism [21, 22]: the Higgs potential has a classical minimum not at $\phi = 0$, the Higgs field acquires VEV and breaks the $SU(2)_L \times U(1)_Y$ symmetry, since it defines a particular direction in the internal group space. However, one residual $U(1)_{em}$ symmetry remains and the single unbroken generator is identified with the electric charge. Since three generators of $SU(2)_L \times U(1)_Y$ are spontaneously broken, three massless Goldstone bosons are expected due to Goldstone's theorem [23]. This theorem can be however circumvented as the massless Goldstone modes provide longitudinal degrees of freedom for the massless long-ranged vector fields of the theory since they share the same quantum numbers.

The Higgs mechanism selects randomly particular linear combinations of gauge fields out of the manifold, one of the combination, which corresponds to the unbroken generator, remains massless and is identified as the photon:

$$A_\mu = \sin \theta_W W_{3\mu} + \cos \theta_W B_\mu. \tag{1.16}$$

The terms are $\sin \theta_W = g'/\sqrt{g^2 + g'^2}$, $\cos \theta_W = g/\sqrt{g^2 + g'^2}$, g and g' are the couping constants of the $SU(2)_L$ or $U(1)_Y$ group respectively. W's are gauge bosons of the former and B is the gauge boson of the latter group. Other selected combinations are charged massive spin 1 bosons $W^\pm$:

$$W_\mu^\pm = (W_{1\mu} \mp i W_{2\mu})/\sqrt{2}, \tag{1.17}$$

and a massive spin 1 neutral boson Z^0:

$$Z_\mu^0 = -\cos \theta_W W_{3\mu} + \sin \theta_W B_\mu. \tag{1.18}$$

There remains also one scalar massive dynamical field - the Higgs boson H.

1.4.2 QCD

QCD is a gauge theory based on the group $SU(3)_C$ with colour triplet quark matter fields. The selection of the gauge group was based on the following constraint: after the idea of three quarks arose from the observations of the spectra of low mass mesons and baryons (quarks as physical manifestation of $SU(3)$ flavour symmetry), and spin 3/2 baryons were interpreted as three quarks bound states with symmetric spin- as well as space- and flavour-wave functions, a new degree of freedom had to be introduced in order that the complete state description obeyes Fermi-Dirac statistics. Each quark can carry a colour index with three possible values (red, green, and blue) and the baryon wave functions are totally antisymmetric in this new index.

A further restriction imposed on the gauge group is the requirement that it must admit complex representations to be able to distinguish quarks from antiquarks as constituents of the meson (quark antiquark) states, since no quark quark bound

states were found. Following simple groups have this last desired property: $SU(N)$ with $N \geq 3$, $SO(4N + 2)$ with $N \geq 2$ and $E(6)$ [24]. The choice of $SU(N = 3)_C$ is confirmed by many processes measuring N, particularly by the Ratio R of the e^+e^- total hadronic cross section to the cross section for the production of muons $e^+e^- \rightarrow \mu^+\mu^-$. At low energies only up, down and strange quarks each in three possible colours can be excited leading to the ratio of 2, assuming fractional charges of quarks (up +2/3 and down -1/3 and equivalent in other generations). If the centre of mass energies exceed 10 GeV charm and bottom quarks can also be produced and so the ratio becomes 11/3. The idea of quarks as pointlike constituents inside hadrons was confirmed by the deep inelastic scattering experiments performed at SLAC [25].

The theory has however a drawback since the spectrum of physical states does not resemble the set of the fundamental fields and does not include coloured states. This phenomenon is called *confinement*. It is postulated that only colour neutral states can occur in nature - the colour is confined inside the hadrons. Confinement could not be proved in QCD up to now. It is believed that the energy between colour charges grows linear with distance $E(R) = kR$, k being the string tension coefficient, because the gluon field between the quarks contracts to a tube (string) with energy proportional to its length. If the separation between the sources becomes large enough, the string between the quarks breaks up and a light quark-antiquark pair is created screening the sources [25, 26]. Quarks produced in scattering events turn via this (*hadronisation*) process into many hadrons which are detected as *jets* emerging in the direction of the original quark in the detectors. The running of the coupling constant (described in a later section) makes confinement probable, since interaction becomes strong and not perturbative computable at large distances.

The Lagrangian of QCD is given by:

$$\mathcal{L}_{QCD} = \mathcal{L}_{classical} + \mathcal{L}_{gauge-fixing} + \mathcal{L}_{ghost}. \tag{1.19}$$

The first part is the classical Lagrangian of the theory, while the other two parts are needed for perturbation calculations after quantisation. The gauge fixing term is a constraint that picks up only one representation from the whole gauge orbit (all field configurations related by gauge transformations) and thus eliminates zero modes. A definition of a gluon propagator without this term is impossible. To provide unitarity of the amplitudes an additional ghost term has to be added to the Lagrangian in case of non abelian theories. Ghosts proliferate in loops (higher order diagrams) and since only tree-level diagrams (diagrams without closed loops of gluon or quark lines) will appear in this work, the term is abandoned in further discussion [26] [25]. The expression for the classical term is:

$$\mathcal{L}_{classical} = -\frac{1}{4} F^A_{\alpha\beta} F^{\alpha\beta}_A + \sum_{flavours} \bar{q}_a \left(i\not{D} - m \right)_{ab} q_b, \tag{1.20}$$

and this work follows [27] in choosing 't Hooft Feynman gauge:

$$\mathcal{L}_{gauge-fixing} = \frac{1}{2} \left(\partial_\alpha \mathcal{A}^{\alpha A} \right). \tag{1.21}$$

The first term describes interactions of spin 1/2 quarks of mass m and massless spin 1 gluons (gauge bosons of strong force). The indices a, b and A are colour

labels, lower case letters run from 1 to 3 being quark colour indices while the upper case letters run from 1 to 8 being gluon colour indices. Covariant derivatives and curvature (field strength) of the $SU(3)$ manifold are defined in the following way:

$$(D_\mu)_{ab/AB} = \partial_\mu \delta_{ab/AB} + ig \left(T^A\right)_{ab/AB} \mathcal{A}^A_\mu, \tag{1.22}$$

$$F^A_{\mu\nu} = \partial_\mu \mathcal{A}^A_\nu - \partial_\nu \mathcal{A}^A_\mu - gf^{ABC} \mathcal{A}^B_\mu \mathcal{A}^C_\nu. \tag{1.23}$$

The f^{ABC} $(A, B, C = 1, \ldots 8)$ are real structure constants of the $SU(3)$ group and g is the coupling constant which determines the strength of the interaction. The quarks are in the fundamental three dimensional representation and the gluons in the adjoint eight dimensional representation, the representation matrices $(T^A)_{ab/AB}$ are in one of the both representations respectively (indicated here as different indices for each case). The matrices satisfy following relations:

$$\left[T^A, T^B\right] = if^{ABC} \left(T^C\right), \tag{1.24}$$

$$f^{A_1 A_2 A_3} = -2i \left\{ Tr\left(T^{A_1 A_2 A_3}\right) - Tr\left(T^{A_3 A_2 A_1}\right)\right\}, \tag{1.25}$$

while the structure constants satisfy the Jacobi-identity:

$$f^{ABX} f^{XCD} + f^{CBX} f^{XDA} + f^{DBX} f^{XAC} = 0. \tag{1.26}$$

Further, the following relations hold:

$$\left(T^A\right)_{ab} \left(T^A\right)_{cd} = \frac{1}{2} \left[\delta_{ad}\delta_{cb} - \frac{1}{N}\delta_{ab}\delta_{cd}\right], \tag{1.27}$$

$$Tr\left(T^{A_1} T^{A_2}\right) = \frac{1}{2}\delta^{A_1 A_2}, \tag{1.28}$$

$$\delta^{AA} = N^2 - 1 \qquad \text{and} \qquad \delta_{aa} = N, \tag{1.29}$$

where N stands for the total number of colours and is equal to 3 in the QCD case. Summation over repeating indices has to be performed.

The Feynman rules for QCD (figure 1.4.2) can be derived from the Lagrangian density given above. Following these rules, scattering amplitudes[4] for processes involving quarks and gluons can be constructed.

1.4.2.1 Asymptotic freedom

The Feynman rules derived so far include *bare* constants (coupling g and masses m) which were used to define the theory via the Lagrangian density. These constants are theoretical constructs and are not measurable as already stated in 1.1. All physical quantities have to be expressed in terms of *renormalised* parameters which depend on the ultraviolet cutoff Λ_0, the bare coupling constants, and an arbitrary scale μ - the point at which the measurement of the physical quantities, which are then associated with the couplings, takes place. Generally, loop corrections (and ghost fields) have to be taken into account and exact propagators and vertices can be defined. If the scale μ is larger than external momenta and quark masses it can be shown that exact propagators and vertices have the same colour and Lorentz structure as the bare ones. Bare and renormalised quantities are connected

---

[4]The term amplitude is used interchangeable with the term matrix-element or S-matrix element.

Figure 1.1: Feynman rules for QCD in 't Hooft Feynman gauge without ghost fields. The $i\epsilon$ prescription was also removed from the propagators, since only tree level amplitudes are considered.

via various renormalisation factors Z which are numbers and which depend on the bare coupling g_0, bare gauge parameter (chosen 1 in the scheme presented here), and the dimensionless ratio Λ_0/μ^2. The renormalisation factors are not arbitrary but satisfy *Slavnov-Taylor* identities which state, that the strength of the coupling $Z_{inv}g_0^2$ extracted from the all different vertices of the theory coincides even after renormalisation [26].

If one considers physical effective charges $g^2(\mu)$ and $g^2(\mu')$ at two different scales and if one assumes $\mu' \gg \mu$ it follows:

$$g^2(\mu) = Z_{inv}\left(\ln\frac{\Lambda_0^2}{\mu^2}, g_0^2\right) g_0^2, \tag{1.30}$$

$$g^2(\mu') = Z_{inv}\left(\ln\frac{\Lambda_0^2}{\mu'^2}, g_0^2\right) g_0^2, \tag{1.31}$$

$$\tag{1.32}$$

with one and the same invariant function Z_{inv}. Logarithms occur due to the fact, that integrations over higher order (loop) contributions have to be peformed, which are logarithmically divergent. A crucial observation is the possibility to treat μ' and $g^2(\mu')$ on the same footing as Λ_0 and g_0^2. Having the value of the coupling at some high scale μ' it is possible to derive the value of the coupling and other observables at the lower scale, since the larger scale plays the role of the ultraviolet cut-off scale as far as momenta less than the large scale value are concerned. It follows that Z_{inv} satisfies a functional equation:

$$Z_{inv}\left(ln\frac{\Lambda_0^2}{\mu^2}, g_0^2\right) = Z_{inv}\left(ln\frac{\mu'^2}{\mu^2}, g^2(\mu')\right) Z_{inv}\left(ln\frac{\Lambda_0^2}{\mu'^2}, g_0^2\right). \tag{1.33}$$

This equation defines the renormalisation group, which tunes the effective charge when the scale is changed. The tuning factor depends only on the ratio of two scales and on the charge defined at the upper scale but not explicit on the scale. The functional equation above restricts the form of the function. If the relation of charges defined at two different scales is written as:

$$g^2(\mu) = Z_{inv}\left(\ln\frac{\mu'}{\mu^2}, g^2(\mu')\right)g^2(\mu'), \qquad (1.34)$$

and then differentiated with respect to $\ln\mu$, the differential equation for the evolution of effective charge reads (after setting $\mu = \mu'$):

$$\mu\frac{dg^2(\mu)}{d\mu} = \beta\left[g^2(\mu)\right], \qquad (1.35)$$

where

$$\beta(g^2) = -2g^2\left.\frac{\partial}{\partial L}Z_{inv}(L, g^2)\right|_{L=0} \qquad (1.36)$$

is called *Gell-Mann-Low function* or β function and $L = \ln(\Lambda_0^2/\mu^2)$. The β function can be expanded into a series in g^2. The first term in the series can be inferred from the one-loop result for $g^2(\mu) = Z_{inv}g_0^2$. This term is equal to:

$$\beta(g^2) = -\frac{b_0 g^4}{8\pi^2} + O(g^6), \qquad \text{with} \qquad b_0 = \frac{11N}{3} - \frac{2}{3}N_f, \qquad (1.37)$$

where N_f is the number of active quark flavours and N is the dimension of gauge group, which is three in QCD case. If only the leading term is taken into account equation 1.35 can be integrated. First the strong constant α_s is defined as:

$$\alpha_s = \frac{g^2}{4\pi}, \qquad (1.38)$$

than the integration is performed, and in this process an integration constant enters the terms. This constant is called Λ_{QCD}, and the solution reads:

$$\alpha_s(\mu^2) = \frac{2\pi}{b_0 \ln\frac{\mu}{\Lambda_{QCD}}}. \qquad (1.39)$$

The value of Λ_{QCD} can be determined since at the cut-off energy scale Λ_0, the coupling constant should attain its bare value. This demand fixes Λ_{QCD} to:

$$\Lambda_{QCD} \equiv \Lambda_0 \exp\left(-\frac{8\pi^2}{b_0 g_0^2}\right). \qquad (1.40)$$

The result 1.39 does not depend on unphysical bare parameters, but rather on their combination Λ_{QCD} which is a true physical parameter for QCD. It represents the scale at which the perturbation theory breaks down since the coupling diverges. The numeric value of the parameter can be obtained by fixing the value of the coupling via measurements at some scale in perturbative domain, usually $\mu = M_Z$ and evaluating it with the renormalisation group equations (1.34) to the value at which perturbation theory breaks down (coupling with the order of magnitude of 1). Depending on the precision of the corrections one arrives at a value of about 200

MeV. Thus α_S becomes large and the perturbation theory starts to fail for scales compatible with the masses of light hadrons, i.e. $1\ GeV$. This result is no surprise since Λ_{QCD} carries a dimension and hence determines all dimensionful quantities in QCD, in particular hadron masses [26]. On the other hand, as mentioned in the introduction to this section, the growth of the coupling at low scales and breaking of perturbative regime makes confinement probable [25]. The phenomenon that the scale Λ_{QCD} carries a dimension contrary to the bare coupling g is called *dimensional transmutation* and it results from the breaking of the conformal symmetry of the tree level action (involving only dimensionless g) by quantum effects [26].

In contrast to behaviour at low scales the effective charge decreases when the characteristic energy grows. It means that with growing energy and decreasing distances perturbation theory becomes more and more justified. This behaviour is called *asymptotic freedom* and it is opposite to the behaviour of the coupling constant in QED which tends to infinity for ever smaller distances. The last property is called Landau-pole of QED and it indicates that the theory is probably not self-consistent. Asymptotic freedom can be linked with non-abelian structure of QCD which is responsible for gluon self interactions.

1.5   Beyond Standard Model

As it was mentioned several times no experimental evidence from particle physics contradict predictions of the SM, the precision measurements of the CERN LEP (Large Electron Positron Collider) collider rather established that radiative corrections as predicted in the SM are necessary to achieve agreement with data. Nevertheless, the SM possesess some internal problems as it was mentioned in the section on QFT. Even discarding formal QFT issues, it must be concluded, relying on astrophysical experiments, that the SM is incomplete. It turns out that neutrinos have masses (which can be incorporated ad hoc in the SM), there is cold *dark matter* (non relativistic matter with no electromagnetic interactions) in the Universe as it was suggested already in 1933 by Fritz Zwicky [28] from application of virial theorem, and finally the Universe is filled with constant energy density called *dark energy* which causes accelerated expansion as inferred from observations of supernovae type Ia. The strongest argument from experimental side is the existence of gravity, since it is completely neglected by the SM [3].

There are also some aesthetic considerations which suggest that the SM should be derived from some broader framework: the SM possesses a large number of free parameters (19) including masses of particles and mixing angles, the SM gauge group was chosen to fit the data and was not derived from first principles, and finally electroweak symmetry breaking is incorporated per "hand" and does not follow from some underlying principle.

The statements above suggest that the SM should be viewed as some kind of effective field theory valid up to energy scales accessible to current colliders (several TeV). It approximates the truly fundamental theory which remains probably valid until the scale of quantum gravity or it approximates some other approximation which has also bounded domain. The effects of this superior theory which could be found with the next generation colliders like the LHC (c.f. section 3) are called physics beyond the Standard Model.
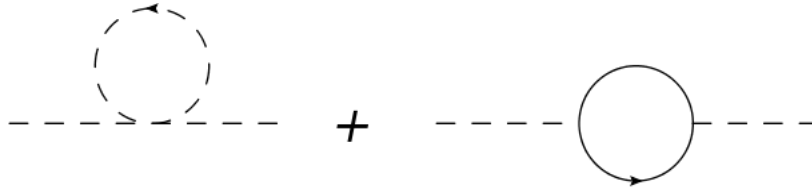
Figure 1.2: Quantum corrections to m_H^2

Scalar Higgs field introduced to break electroweak symmetry can provide a hint on the scale at which physics beyond the SM should enter the considerations. The mass of the Higgs boson should be also renormalised, but since it is a scalar particle the leading divergence of the corrections is not logarithmic but quadratic:

$$m_H^2(renorm) \simeq m_H^2 + \frac{c}{16\pi^2}\Lambda^2. \tag{1.41}$$

The constant term c depends on various parameters of the SM and Λ can be interpreted as the scale at which the SM ceases to be valid. To compute this loop corrections, diagrams like 1.2 have to be evaluated. Generally bosonic and fermionic loops as well as momentum independent energy shifts like the first diagram in 1.2 lead to quadratic divergences, however bosonic and fermionic contributions have different signs. If the typical energies exceed the scale Λ something "new" should happen, it is possible that new heavy particles can be created or, that the SM breaks down because some unknown interaction has its strong regime at this scale. Λ is bounded from above with the reduced Planck scale of order 10^{18} GeV at which quantum gravity corrections become important [3].

The left hand side of the equation 1.41 - the physical Higgs boson mass - should be below 1 TeV in order to maintain unitarity (preservation of probability) in processes involving massive gauge bosons [29]. Now a constraint on possible values of Λ can be imposed, since otherwise the SM would be affected by the *fine tuning problem*, which means that the value of the bare Higgs mass should be limited to some extreme accurate large number in order to cancel higher order corrections. Such tuning would lead to a situation where small changes of the underlying parameters would lead to extreme differences in the predictions of the theory for the TeV scale.

To avoid such problems one can conclude that $\Lambda \leq O(1\,TeV)$ and that one would expect to find new degrees of freedom in high energy collisions at the TeV scale. The next chapter of this work should provide an answer to the question what would be a promising theory that can appear at this scale.

2

Supersymmetry

Supersymmetry (SUSY) is a hypothetical symmetry of nature relating fermions and bosons. It was introduced independently by two Russian groups in 1971-1972 [30, 31], and then also independently in the west by Julius Wess and Bruno Zumino [32] in 1974. Simultaneously SUSY was used in two dimensions (as a symmetry of string world-sheet) within string theory [33, 34]. The Wess-Zumino model had the biggest impact on particle physics, leading to the formulation of the Minimal Supersymmetric Standard Model (MSSM) in 1981 [35].

The genuine desirable feature of SUSY is the unavoidable cancellation of the fermionic and bosonic loop contributions to scalar masses, leading to the solution of the *fine-tuning problem* of the SM, q.v. section 1.5. However, this feature was not the motivation for the development of SUSY in the 70's, and hence it is an impressive result that a theory developed for a couple of different reasons can additionally solve one of the crucial problems of the SM. In the 90's it was furthermore shown [36], that the contributions of the supersymmetric particles change the coefficients of the renormalisation group equations in such a way, that the values of the coupling constants of the SM interactions meet at high energy ($E \approx 2 \cdot 10^{16} \ GeV$). SUSY can also solve one of the astrophysical problems by providing a natural dark matter candidate [37].

Regarding the points above, SUSY is believed to be the most promising extension of the SM. The introduction of SUSY to the SM implicates however addition of new particles, since it is impossible to relate existing SM particles to each other. The masses of these new particles would equal the masses of their SM partners in case of unbroken SUSY. Since none of the superpartners has been discovered so far, SUSY must be broken. In order to retain the desired SUSY features, the masses of these additionally introduced particles must lie within the upper limit of $\sim 1 \ TeV$. If the so called *weak scale supersymmetry* is realised in nature, it should be discovered at the Large Hadron Collider, which starts the operation in 2009, q.v. next chapter.

This chapter provides a short introduction to SUSY with particular emphasis of the aspects relevant for SUSY searches with the CMS detector.

2.1 Supersymmetry algebra

A supersymmetry transformation turns a bosonic state into a fermionic state and vice versa. The generator of such transformations is called conventionally Q and satisfies following relation:

$$Q \left| Boson \right\rangle = \left| Fermion \right\rangle, \qquad Q \left| Fermion \right\rangle = \left| Boson \right\rangle. \qquad (2.1)$$

From this relation follows, that the generator is an anticommuting and hence fermionic object changing the spin by half-odd amount and changing the statistics. The generator Q is thus a spinor (q.v. chapter 4), and since spinors are intrinsically complex, the hermitian conjugate $Q^\dagger$ of Q is also a symmetry generator. Both generators carry spin angular momentum $1/2$ and thus SUSY is obviously an additional space-time symmetry. SUSY circumvents the Coleman-Mandula theorem [38], stating that every symmetry of the S-matrix must be a direct product of the Poincaré group and an internal symmetry group (if there is a mass gap), by introducing anticommuting generators. The Coleman-Mandula theorem was extended by Haag, Lopuszanski and Sohnius [39] to the case of Lie superalgebras and this extension restricts the possible forms of supersymmetries for interacting quantum field theories. It follows that the generators Q and $Q^\dagger$ have to satisfy following commutation and anticommutation relations [3]:

$$\left\{ Q_\alpha, Q_{\dot{\alpha}}^\dagger \right\} = -2\sigma_{\alpha\dot{\alpha}}^\mu P_\mu, \qquad (2.2)$$

$$\{ Q_\alpha, Q_\alpha \} = 0, \qquad \left\{ Q_{\dot{\alpha}}^\dagger, Q_{\dot{\alpha}}^\dagger \right\} = 0, \qquad (2.3)$$

$$[Q_\alpha, P_\mu] = 0, \qquad \left[Q_{\dot{\alpha}}^\dagger, P_\mu \right] = 0, \qquad (2.4)$$

P_μ being the generator of the space-time translations, and $\sigma_{\alpha\dot{\alpha}}^\mu$ being the spin tensor introduced in the section on Weyl spinors in chapter 4.

The single-particle states of a supersymmetric theory fall into an irreducible representations of the supersymmetry algebra, called supermultiplets. Each supermultiplet contains fermionic and bosonic states, whereas the number of the fermionic degrees of freedom equals the number of bosonic degrees of freedom. The particles from one particular supermultiplet are called superpartners and have the same mass. Since the generators of the supersymmetry commute with the generators of the gauge groups, all superpartners have also the same internal quantum numbers (el. charge, isospin, colour).

2.2 The minimal supersymmetric standard model

As it was mentioned in the beginning of this chapter, the introduction of the SUSY into the SM can solve the fine-tuning problem. If every SM fermion is supplemented with a scalar superpartner and they both have the same coupling strength to the Higgs boson ($c = \lambda_s = |\lambda_f|^2$), the loop corrections to the Higgs mass vanish because of the relative minus sign between fermionic and bosonic contributions. The remaining corrections to Δm_H^2, due to the SUSY breaking, are small as long as the masses of the superpartners are about $1\ TeV$ [3]. The solution of the fine-tuning problem was an important motivation for the development of various supersymmetric models. This section introduces the minimal extension of the SM involving only one additional degree of freedom in the superspace ($N = 1$ SUSY), the so called minimal supersymmetric standard model (MSSM).

2.2.1 Particle content

The fermions of the SM are members of chiral supermultiplets[1] having a bosonic (spin-0) superpartner. These superpartners are called *sfermions*. The names of the single superparnters are results of the prepending of an "s" for scalar to the names of the corresponding SM fermions (e.g. selectron, stop, sbottom). The spin-1 SM bosons are members of the gauge supermultiplets[2] having spin-1/2 fermions as superpartners which are generally referred to as *gauginos*. The supersymmetric partners are represented by the same symbols as corresponding SM particles, but with a tilde, for example $\tilde{e}$ for the selectron.

The MSSM needs two complex Higgs doublets to generate masses of the particles. One of this doublets couples only to the up-type particles (H_u) while the other doublet gives masses to the down-type particles (H_d). Thus there are four complex Higgs states corresponding to eight degrees of freedom. Three of these degrees of freedom are needed to provide masses of the $W^{\pm}$- and Z-bosons, leaving five degrees of freedom for mixing into the Higgs-bosons. There are three neutral superpositions of H_u^0 and H_d^0 : two scalars h^0 , H^0 and a pseudoscalar A^0, as well as two charged superpositions of $H_{u/d}^{\pm}$: the $H^{\pm}$.

Not all previously introduced superparticles of the MSSM are mass-eigenstates. Symmetry breaking can lead to the mixing between particles with same quantum numbers. The gluino, being in the eight-dimensional adjoint representation, is the only SUSY member of the gauge multiplet which cannot mix. The electro-weak symmetry breaking leads to the mixing of the Higgsinos with the supersymmetric partners of the electro-weak gauge bosons. The four neutral mass eigenstates are called neutralinos and are denoted by $\chi_{1...4}^0$. They are superpositions of the neutral Higgsinos with the zino ($\tilde{Z}$) and photino ($\tilde{\gamma}$). The mixing depends on the Weinberg angle θ_W, the ratio of the vacuum expectation values of the two Higgs doublets $\tan\beta$, the mass of the Z-boson, and the mass parameters of the SUSY breaking terms M_1 and M_2. The charged Higgsinos and the winos mix respectively into two charged mass eigenstates $\chi_{1,2}^{\pm}$, depending on the mass of the W-boson and the Higgsino mass-parameter μ. The numbering scheme of charginos and neutralinos begins with the lightest particle and the number grows with the mass.

2.2.2 Superpotential

The superpotential describes the interactions between the particles in the MSSM [3]:

$$W_{MSSM} = \bar{u}y_u Q H_u - \bar{d}y_d Q H_d - \bar{e}y_e L H_d + \mu H_u H_d, \tag{2.5}$$

where $\bar{u}$, $\bar{d}$, Q, H_u, H_d, $\bar{e}$, and L are the chiral superfields of the associated chiral supermultiplets ($\bar{u}$, $\bar{d}$, Q stand for the supermultiplets of squarks and quarks, L and $\bar{e}$ stand for the supermultiplets of sleptons and leptons and $H_{u,d}$ stand finally for the Higgs/Higgsino multiplet). The y_i terms are Yuakawa-matrices describing

---

[1]Multiplets consisting of two-component Weyl fermions and complex scalar fields. Only chiral supermultiplets can contain fermions whose left-handed parts transform differently under the gauge group than their right-handed parts.

[2]Multiplets containing spin-1 bosons and spin-1/2 fermionic superpartners whose right- and left-handed components have the same gauge-transformation properties. The last property has to be satisfied, since gauge bosons transform in the adjoint representation, which is its own conjugate.

the mixing angles between the particles and their couplings, while μ is the Higgs mass parameter. There is no theoretical reason prohibiting the addition of other gauge invariant terms to the superpotential. The most general gauge-invariant and renormalisable superpotential would however include terms violating lepton (L) and baryon number (B) [40] leading inter alia to the proton decay. Postulating the conservation of these numbers is a drawback in comparison with the SM, where the conservation is the consequence of the impossibility of construction renormalisable Lagrangian terms that would violate L and B. Instead a new symmetry called *R-parity* is added to the model. This symmetry eliminates the possibility of B and L violating terms in the renormalisable superpotential and has additional nice properties.

2.2.3   R-parity

The R-parity is defined as:

$$P_R = (-1)^{3(B-L)+2S}, \tag{2.6}$$

with S being the spin quantum number of the particle. From the definition follows, that all SM particles have a R-parity $P_R = 1$, while all SUSY particles have $P_R = -1$. The conservation of R-parity, which is a postulate of the MSSM, leads not only to the conservation of B and L, but also to the pair-wise creation or annihilation of SUSY particles. Additionally every SUSY decay chain must end with a lightest stable supersymmetric particle, the LSP. Depending on the SUSY breaking scenario, the LSP can provide a good *dark matter candidate* [37].

2.3   Supersymmetry breaking

Since SUSY particles were not discovered parallel to the discovery of SM particles, their masses must be larger than the masses of known particles, and hence SUSY must be spontaneously broken [40]. This can be achieved by the introduction of additional breaking terms in the SUSY Lagrangian. If these terms preserve renormalisability and do not introduce new quadratic divergences, one speaks of soft supersymmetry breaking. The general SUSY potential including soft breaking terms introduces 105 new free parameters to the theory making the general model intractable. Therefore, several more constrained models of SUSY breaking were constructed. In general the breaking occurs in a "hidden sector" of particles, that have no direct couplings to the "visible sector" : the chiral supermultiplets of the MSSM. The breaking is then mediated via some interaction which is shared between the two sectors leading to the soft breaking terms.

This study deals with the SUSY breaking scenario based on the assumption, that gravity is the interaction providing the connection between the two sectors. This scenario is called mSUGRA (minimal supergravity). The mSUGRA model of SUSY reduces the 105 parameters of the MSSM to 5 free parameters, defined at the scale of the great unification (GUT-scale). The free parameters are: $m_{1/2}$ - the unified mass term of the gaugino breaking parameters, m_0 - the unified mass term of the sfermion breaking parameters, A_0 - unified trilinear couplings of the SUSY breaking, $\tan\beta$ - the ration of the VEV's of the two Higgs-doublets, and $\text{sign}(\mu)$ the sign of the Higgs mass parameter. Given a particular set of these parameters, one can compute

the values of the particle masses at the lower scale by using renormalisation group equations.

The CMS collaboration defined a set of test points in the mSUGRA parameter space, to cover significantly different experimental signatures [4]. The points are divided in two groups: the so called high-mass points (HM) whose parameter lead to higher masses, and low-mass points (LM) whose parameters lead respectively to the lower SUSY particle masses. The CMS test points are shown in the Fig. 2.3 in the $m_0 - m_{1/2}$- plane of the mSUGRA parameter space, and additionally the values of the parameters for some points relevant for the present work are given in Table 2.3.
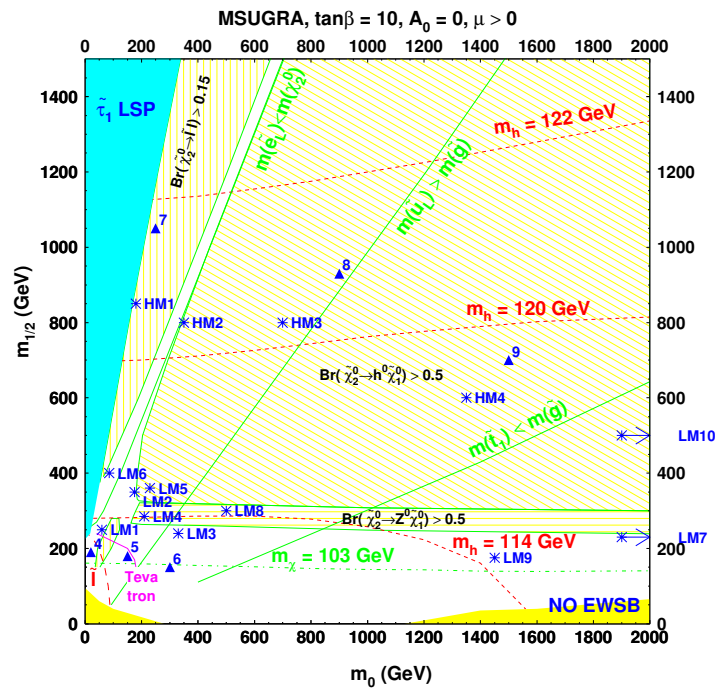

Figure 2.1: The CMS test points in the $m_0 - m_{1/2}$-plane of the mSUGRA parameter space (the other parameters are $\tan \beta = 10$, $A_0 = 0$, and $\mu > 0$) . The testpoints are labeled with $*$. The turquoise domain corresponds to a charged LSP, which is exclueded experimentally, while the yellow domain does not yield electro-weak symmetry breaking. Further experimentally excluded domains are also shown [4].

Point	m_0	$m_{1/2}$	$\tan \beta$	$\text{sign}(\mu)$	A_0
LM1	60	250	10	$+$	0
LM4	210	285	10	$+$	0
LM8	500	300	10	$+$	-300
HM3	700	800	10	$+$	0

Table 2.1: mSUGRA parameter values for selected test points. Masses are given in units of GeV.

2.4   Experimental signals

If weak scale SUSY is realised in nature, it should be accessible with the Large Hadron Collider [41]. A hadron collider like LHC offers many SUSY production channels, however the particles will be produced in pairs, if R-parity is conserved. The production processes of the strong interaction (e.g. $gg \rightarrow \tilde{g}\tilde{g}$, $qq \rightarrow \tilde{g}\tilde{q}_i$) will dominate over the possible electro-weak channels like $u\bar{d} \rightarrow \chi_i^+ \chi_i^0$, due to the larger cross sections [40] unless the squarks and gluionos are much heavier than the other gauginos. The lightest SUSY particle is stable, if the R-parity is conserved, and only weakly interacting. It follows, that the LSP traverses the detector without leaving energy deposition in the calorimeter, and produces missing transverse energy (MET), like the SM neutrino. Therefore, missing transverse energy is a characteristic SUSY signature. The present work tries to find a method to distinguish between mismeasured QCD events with fake MET, and true signals of decaying heavy particles, like SUSY, via new variables for the description of QCD processes.

The large masses of the SUSY particles yield a short life-time , which causes them to decay in the detector often via long chains of intermediate particles. The decay ends with the LSP, which is the neutralino χ_1^0 in the model considered in this work. If the decay chain entails only such SM particles, which either hadronise themselves leading to jets in the detector, or decay further in quarks like the heavy gauge bosons $W^\pm$ and Z^0, the process is called all-hadronic. Such processes are characterised by larger MET and many jets. Figure 2.4 shows a possible all-hadronic decay chain.

Figure 2.2: Example for an all-hadronic decay chain. The pairwise produced supersymmetric particles decay via a chain into quarks, gauginos, hadronically decaying SM gauge bosons, and neutralinos.

3

The CMS Experiment

Being highly successful, the Standard Model still cannot be the truly fundamental theory of matter and forces as it was shown in chapter 1.5. To probe physics beyond the Standard Model (SM) and to decide if one of the various proposed extensions to the SM is really realised in nature, experiments at the TeV scale have to be made [29], q.v. previous chapter. Such experiments will become possible after the start of the operation of the Large Hadron Collider (LHC) at the European Organisation for Nuclear Research, CERN[1], near Geneva. The Compact Muon Solenoid (CMS) Experiment is one of two multipurpose elementary particles detectors built at the LHC in order to examine physics at the TeV scale. The main focus is put on the unveiling of the origin of electroweak symmetry breaking, for which the Higgs mechanism is presumed to be responsible, and on the search for supersymmetric particles, since Supersymmetry is the most promising candidate for an extension of the SMPP cf. section 2. In the following some of the LHC properties are reviewed and CMS design is introduced.

3.1 LHC

The Large Hadron Collider [44] is a two ring superconducting hadron accelerator built into the existing tunnel of the Large Electron Positron Collider (LEP) the predecessing major particle accelerator at CERN. The 26.7 km circumference tunnel was constructed for LEP between 1984 and 1989 and is situated 49 - 150 m below the ground level. At four interaction points proton or fully stripped lead ion (^{208}Pb^{82+}) beams are crossed and particles collide at the design centre of mass energy of 14 TeV for protons or 1.15 PeV for lead ions. Four detectors were build around the interaction points - ALICE (A Large Ion Collider Experiment) [45] at interaction point 2, designed for investigations of quark-gluon plasma in ion collisions, ATLAS (A Toroidal Lhc ApparatuS) [46] at interaction point 1, a general-purpose experiment like CMS, CMS [47] at interaction point 3 and LHC-B (LHC-Beauty) [48] at

---

[1]CERN is a french acronym for *Conseil Européen pour la Recherche Nucléare* (European Council for Nuclear Research), which was a provisional council founded in 1952 in order to establish European subatomic physics research organisation. The organisation become European Organisation for Nuclear Research in 1954, but the acronym CERN was retained [42], [43].

interaction point 4 build to examine CP-violation in processes with b quarks. The LHC has eight arcs and eight straight sections and each interaction point is located in one of the latter. The insertions in the remaining four straight sections do not have beam crossing and are used either for beam collimation or for acceleration and damping. Each exertion is numbered clock-wise beginning with ATLAS interaction point, CMS being at the point 5 consequentially. Figure 3.1 shows the schematic LHC layout. Protons were selected as interacting particles in spite of being non el-
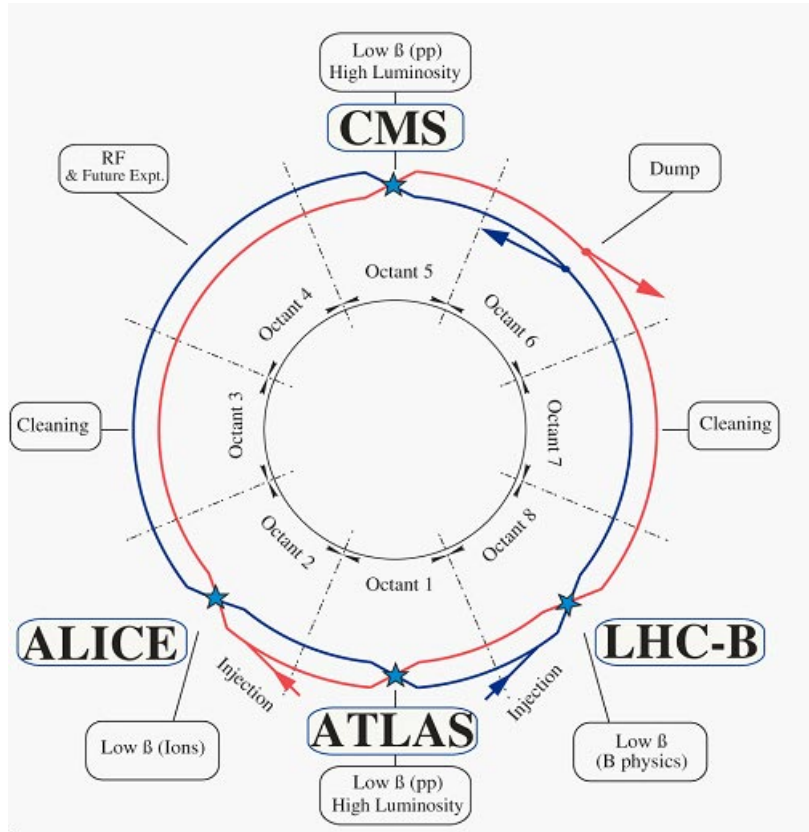
Figure 3.1: Schematic layout of the LHC. Collimation systems for both beams are situated at points 3 and 7, RF acceleration systems one for each beam are in the exertion at point 4. The two beams can be vertically extracted from the machine at point 6 (beam dump) [44].

ementary, since the synchrotron radiation, the major source of energy losses in ring accelerators, falls of with the fourth power of the mass m of the particle being accelerated ($\propto m^{-4}$). Furthermore, protons can be produced in large numbers, contrary to antiprotons, which enable a high number of particles per bunch. Together with the small time interval of 25 ns between the bunches this leads to a high number of protons inside the collider. This large number of protons and the small β-function values of the focussing magnets at the ATLAS and CMS interaction points lead to high LHC design luminosity of 10^{34} $cm^{-2}s^{-1}$ for both experiments. The luminosity L of a hadron collider [25], assuming no crossing angle at the interaction point, is defined as

$$L = \frac{f}{\pi} \frac{N_{h_1} N_{h_2}}{n_b} \frac{\gamma}{\sqrt{\beta_x^* \beta_y^* E_x^* E_y^*}}, \quad (3.1)$$

Quantity	pp operation	Heavy-ion operation
Design energy per nucleon ($\sqrt{S}/2$)	$7\ TeV$	$2.76\ TeV$
Dipole field at $7\ TeV$ (B)	$8.33\ T$	$8.33\ T$
Design Luminosity (L)	$10^{34}\ cm^{-2}s^{-1}$	$10^{27}\ cm^{-2}s^{-1}$
Bunch separation	$25\ ns$	$100\ ns$
Number of bunches (n_b)	2808	592
Number of particles per bunch (N)	$1.15 \cdot 10^{11}$	$7 \cdot 10^{7}$
RMS beam radius at IP (σ^*)	$16.7\ \mu m$	$15.9\ \mu m$
Transverse normalised emmitance (E^*)	$3.75\ \mu m$	$1.5\ \mu m$
Twiss function β^* at IP	$0.55\ m$	$0.5\ m$
Luminosity lifetime (τ_L)	$15\ hr$	$6\ hr$

Table 3.1: Some of the relevant LHC parameters. Given are nominal values for proton-proton and heavy-ion operation [44]

where N_{h_i} are total numbers of the hadrons in each beam. Other parameters are f the revolution frequency, n_b the number of bunches, $\gamma = E/m$ the relativistic factor, E_i^* transverse emmitance of the beams, and β_i^* wavelength of the betatron oscillations of the beams. For a Gaussian beam distribution E_i^* and β_i^* can be replaced by normalised values E^* and β^* equal for each direction. The LHC luminosity will be reduced by a geometrical factor due to the small crossing angle between the beams at the interaction point. Values of some important parameters of the LHC machine are given in table 3.1

3.2 CMS

The Compact Muon Solenoid Experiment [47] [49] is a general purpose detector, whose mostly cylindrical component shells cover the whole solid angle around the interaction point. Being 21.6 meters long, having a diameter of 14.6 meters and a weight of 14.5 tonnes CMS outweighs ATLAS, whose dimensions amount to $44\ m$ length, $25\ m$ diameter, and 7000 tonnes weight. The CMS collaboration adopted following coordinates conventions: The x-axis points radially inward toward the centre of the LHC and the y-axis points vertically upward. Thus, the z-axis points along the beam direction towards the Jura mountains from LHC point 5. The azimuthal angle ϕ is measured from the x-axis in the $x-y$ plane. The polar angle θ is measured from the z-axis. Pseudorapidity is defined as:

$$\eta = -\ln\left(\tan\frac{\theta}{2}\right) \tag{3.2}$$

and equals rapidity if the particle has no mass or the mass can be neglected (relativistic limit). Rapidity is preferred to the angle θ because it is an additive quantity under Lorentz boosts along the z-direction, which implies that rapidity differences are Lorentz invariant [50].

3.2.1 Purpose

CMS was designed to achieve all physical goals mentioned in the introduction to this chapter while operating in the hadron collider environment. Following requirements

on the detector originating in the premises for Higgs discovery have to be taken into account. The current lower limit for Higgs mass was set by LEP to 114 GeV/c^2. Hadronic Higgs decay dominates in the vicinity of this value, but large QCD background and poor mass resolution of jets make a discovery in this channel difficult. More promising signals invole final states with isolated leptons and photons. If the Higgs is in the 114-130 GeV/c^2 mass range CMS will particularly look for the $H \rightarrow \gamma\gamma$ signal. The Higgs can decay into two Z bosons if its mass is above 130 GeV/c^2, one boson being virtual if $m_h < 2m_Z$, in this case it can be found via the 4-lepton final state from Z decays. In both cases it is essential to definitely identify all particles and to measure their charges. For Higgs masses above 600 GeV/c^2 the cross section drops and it is inevitable to use jets and missing transverse Energy (MET) of W and Z decay remnants in the $H \rightarrow W^+W^-$ and $H \rightarrow ZZ$ channels.

The search for supersymmetric events requires also a good lepton identification and a fair jet energy resolution. Heavy supersymmetric particles decay in cascades to their standard model partners until, assuming R-parity conservation, the decay chain reaches the lightest supersymmetric particle (LSP) which is stable. The LSP interacts only weakly or via gravitation and thus can be detected only as MET in the detector. Consequently SUSY final states are characterised by an abundance of MET and many jets and leptons in mSUGRA SUSY breaking scenario or by MET and enhanced number of isolated photons in GMSB case. Good resolution of MET and jets as well as an understanding of the jet energy scale is crucial for SUSY searches in the all-hadronic channel, which are relevant for the present work.

In summary, the CMS design meets the following demands:

- Good muon identification and precise measurement of their momenta across the whole detector, good dimuon mass resolution and measurement of the muon charge in tracker and in the muon system.

- Good particle momenta resolution and reconstruction efficiency in the inner tracker as well as efficient selection of τ's and b-jets, requiring pixel detectors close to the interaction region.

- Good resolution of the electromagnetic calorimeter for measurement of photon and electron momenta as well as efficient photon and lepton isolation and π^0 rejection.

- A hermetically closed hadron calorimeter, which enables accurate measurement of MET and dijet masses in a large angular domain.

Figure 3.2.1 shows the overall layout of the CMS detector. The innermost layer of the detector in the vicinity of the interaction point consists of silicon pixel and microstrip detectors, which reconstruct tracks of charged particles. The tracker is surrounded by an electromagnetic and a hadron calorimeter, which are used for particle identification and energy measurements. The outer layers compose the muon detection system, since muons are minimal ionising particles. A high magnetic field configuration was chosen in order to resolve boosted particle pairs with different charges. This configuration is realised via a 13 m long 4 T superconducting solenoid with a diameter of 5.9 m inserted between the main part of the hadron calorimeter and the muon system. In the following components of the detector are described in more detail beginning with the inner parts.
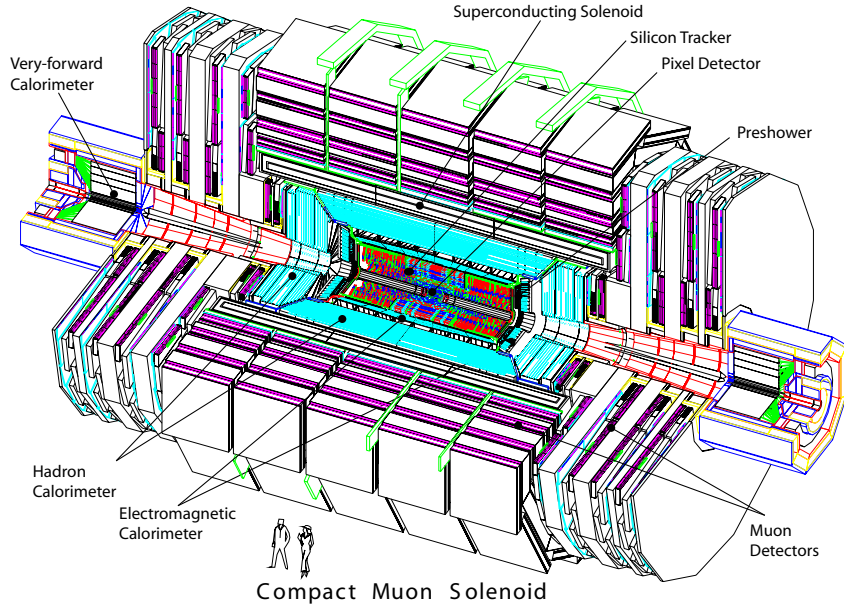
Figure 3.2: Schematic view of the CMS detector [47]

3.2.2 Tracker system

The task of the tracker is a precise and efficient measurement of the charged particle trajectories. The total tracking volume is given by a cylinder of 5.8 m length and 2.6 m diameter. In order to resolve and identify secondary vertices of b-quarks and τ-leptons decays, which are characteristic for many interesting channels, in the region of high particle flux, three cylindrical layers of pixel detector modules surround the interaction point. The pixel size of $100 \times 150 \ \mu m^2$ was chosen to achieve the desired impact parameter resolution. Each of the layers have a length of 53 cm and they are situated at the radii of 4.4, 7.3 and 10.2 cm. Two endcaps close the pixel detector at each side.

At the radius of about 20 cm the particle flux drops and it is possible to use silicon strips for track reconstruction. The intermediate region of the tracker up to 55 cm contains Tracker Inner Barrel and Discs (TIB/TID) with the minimal strip size of $10 \, cm \times 80 \mu m$. The TIB/TID is surrounded by the Tracker Outer Barrel (TOB), which extends to 116 cm, and whose strips have maximal size of $25 \, cm \times 180 \mu m$. Beyond the z range of $\pm$ 118 cm, Tracker EndCaps (TEC) cover the remaining tracker volume, extending the acceptance of the tracker up to a pseudorapidity of $|\eta| < 2.5$. Each TEC is composed of 9 disks, carrying up to 7 rings of microstrip detectors.

A total of 66 million pixel and 9.6 million strip detectors cover an area of 200 m^2, making the CMS tracker the largest silicon detector ever built.[47].

3.2.3 Electromagnetic calorimeter (ECAL)

The electromagnetic calorimeter surrounds the tracker and is used for energy measurement and identification of particles, especially electrons and photons. It covers a pseudorapidity range up to $|\eta| < 3.0$ and was designed to resolve the decay of

two photons from the proposed Higgs boson, cf. section 3.2.1. For this purpose it was made of 61200 lead tungstate ($PbWO_4$) crystals in the central barrel part and 7324 $PbWO_4$ crystals in each of the endcaps. The scintillation light is detected by avalanche photodiodes in the barrel region and vacuum phototriodes in the endcap region. Lead tungstate crystals were chosen because of the short radiation length of 0.89 cm and radiation-hardness. Furthermore, 80% of the light is emmited in 25 ns, which is of the same order of magnitude as the LHC bunch crossing time.

The barrel region of the ECAL covers a pseudorapidity up to $|\eta| < 1.479$ and consists of crystals which have a length of 230 mm equivalent to 25.8 radiation lengths (X_0). The remaining pseudorapidity range is covered by the endcaps, each divided into 2 D-shaped halves (Dees), where each Dee holds 3662 crystals with the length of 22 cm (24.7 X_0).

The energy resolution of the ECAL is given by

$$\left(\frac{\sigma}{E}\right)^2 = \left(\frac{S}{\sqrt{E}}\right)^2 + \left(\frac{N}{E}\right)^2 + C^2, \tag{3.3}$$

where S is a stochastic, C a constant, and N an electronic noise term. The values of the terms could be determined from measurements; they amount to $S = 2.8\% \sqrt{GeV}$, $N = 0.12\,GeV$, and $C = 0.3\%$ [47].

3.2.4   Hadron calorimeter (HCAL)

The hadron calorimeter is responsible for the measurement of hadron jets and, indirectly, neutrinos or other exotic weakly interacting particles resulting in apparent missing transverse energy. The hadron calorimeter barrel (HB) and endcaps (HE) sit behind the electromagnetic calorimeter as seen from the interaction point. HB is the last component inside the magnetic coil. However the total amount of the absorbing material which can be put inside is restricted. Brass was chosen as absorber material, since it has short interaction length and is not magnetic. The innermost and outermost absorber layer is made of stainless steel for structural strength. Plastic scintillators are inserted between the absorber layers. The light they produce is converted by wavelength-shifting fibres embedded in the scintillator tiles and channeled to photodetectors via clear fibres. The HB consists of 32 rings and covers a pseudorapidity range of $|\eta| < 1.4$. Except for the first and the last scintillator layer, which are 9 mm thick, all other layers have a thickness of 3.7 mm.

The outer hadron calorimeter (HO) is placed outside the solenoid to ensure the measurement of the jets, which penetrate the magnet in the $|\eta| < 1.3$ region. The absorber in HO correspond to 1 interaction length and the scintillator plates are 10 mm thick.

The calorimeter endcaps (HE) $1.3 < |\eta| < 3.0$ as well as the forward region (HF) complete the hadron calorimeter and provide coverage up to a pseudorapidity of 5.0. The forward calorimeter makes use of iron plates as absorber material. Photomultipliers detect the Cherenkov light emitted by the particles in the quartz fibres, which are inserted between the absorbers. The forward calorimeters provide full geometric coverage for the measurement of the transverse energy in the event.

The E_T resolution of the HCAL is almost equal in all detector parts which is shown in figure 3.3. The MET resolution for QCD dijet events amounts to
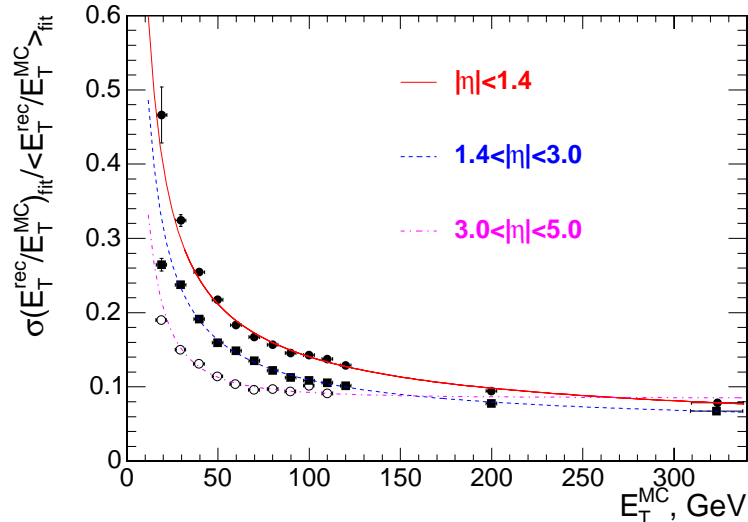
Figure 3.3: The jet transverse-energy resolution as a function of the jet transverse energy in different detector parts. The jets are reconstructed with an iterative cone algorithm (cone radius = 0.5) [47].

$$\sigma(\text{MET}) = 1.0\sqrt{\sum E_T}. \tag{3.4}$$

Taking into account the electromagnetic calorimeter the total jet resolution amounts to

$$\frac{\sigma}{E} = \frac{120\%}{\sqrt{E}} \oplus 6.9\%. \tag{3.5}$$

3.2.5 Superconducting solenoid

The 12.5 m long, 6 m inner diameter, 4 T superconducting solenoid is the distinctive feature of the CMS detector. At full current of 19.5 kA 2.6 GJ of energy is stored inside the magnet. The ratio between stored energy and the cold mass of 11.6 KJ/kg causes large mechanical deformation during energising, beyond the values of previous solenoidal detector magnets. The CMS magnet uses innovative self-supporting high-purity aluminium-stabilised NbTi conductor to provide the necessary hoop strength. The magnetic flux is returned through a 10 000 t iron yoke comprising 5 wheels and 2 endcaps composed of three disks each. The structure of the magnet determines dimensions and weight of the whole detector and provides structural support for all other components [47].

3.2.6 Muon system

The muon system is the outermost component of the detector. As the experiment's middle name suggest, muon identification and momentum measurement is of central importance to CMS, since process signatures involving muons can be recognised over the very high background rate expected at the LHC. Muons are minimal ionising particles and besides neutrinos the only known particles, which can traverse the inner part of the detector without major energy losses and hence can be used for precise invariant mass measurements.

To ensure sufficient energy resolution in the barrel region ($|\eta| < 1.2$), where the muon rate is low and the neutron introduced background is small, the muon system there consists of four modules of drift tube (DT) chambers, integrated in the iron return yoke. The chambers are filled with a gas mixture of argon and carbon dioxide. Due to the uniform magnetic field in the chambers single wire resolution better than 250 μm can be achieved.

High radiation exposure as well as a high and non uniform magnetic field suggest the use of radiation resistant cathode strip chambers (CSC) in the endcap region of CMS ($|\eta| < 2.4$). Resistive plate chambers (RPC) are used as a complementary dedicated trigger system in the whole detector to assign the muons to a particular collision, because the RPC response time is superior to the ones of DT's and CSC's [47].

3.2.7   Data aquisition and trigger

High luminosity of the LHC, which is needed for studies of rare processes, together with the total proton cross section of 100 mb cause a very high event rate of 10^9 events/s. This rate corresponds to a data stream of several TB/s, assuming 250 kB as single event size. It is impossible to store and process such large amounts of data. Therefore a reduction of the rate to a viable size of 100 events/s has to be achieved. This task is performed by the trigger and data acquisition system of CMS (TriDAS), which enriches the recorded sample with physical interesting events. TriDAS consists of four parts: detector electronics, custom made hardware Level 1 (L1) Trigger, readout network, and finally High-Level Trigger (HLT) a software system implemented on a processor farm of commercial PC's.

L1 trigger uses basic very fast reconstructed trigger objects made of calorimeter and muon system data with reduced resolution, to select interesting events with an output rate of 30 kHz. Such events could be characterised by a large amount of MET, large jet multiplicity or leptons. The whole detector data for each event is stored for 3.2 μs during the decision process. This data is forwarded to the HLT if the event is selected. HLT uses full event data for filtering with advanced objects and higher thresholds and writes 100 events/s on average to the mass storage devices.

4

Computational Techniques

The Feynman rules derived in chapter 1.4.2 allow perturbative calculations of processes involving quarks and gluons. However, the calculations can become very complicated, since the rules are build upon Dirac (4 component) spinors and a lot of trace algebra of γ matrices, and additionally QCD colour algebra has to be performed. Furthermore, the final expressions for S-matrix elements can become very large and some fundamental aspects of interactions can be hidden in the notation.

To calculate processes with many particles, as needed for tree level calculations of multijet QCD events (c.f. next chapter), new techniques have to be introduced. A first step is the deployment of orthogonal helicity states for all particles. Instead of carrying out the spin sums, the amplitude is evaluated for every possible combination of helicity states. Such amplitudes are called *helicity amplitudes*. The square of the matrix element[1] transforms to the sum of the squares of helicity amplitudes, since helicity states are orthogonal. The gauge freedom for the spin 1 bosons translates into freedom of choosing their helicity vectors, which can be used to eliminate many Feynman diagrams. In the next step 2 component spinors (first introduced by Weyl [51]) are used for calculations. They remove the γ-algebra and translate Dirac spinors and Minkowski vectors to the same kind of objects.

This chapter introduces spinor representations of the Lorentz group and the spinor calculus for massless fermionic spin-1/2 and bosonic spin-1 particles. The restriction to the massless particles is just a convenience, since this work deals primary with gluons and high energy limit is satisfied for quarks (it does not apply to heavy particles, like i.e. SUSY). A short introduction to the treatment of colour algebra is also provided in the end of this chapter. In the spinor sections the presentation follows [8], [6], and [27] while the notation from [27] is used.

---

[1]In the following the terms matrix element and S-matrix element are used interchangeable, if no confusion is possible.

4.1   Structure of the Lorentz group

The space-time background of QFT is the flat Minkowski space $\mathcal{M}$. The Lorentz-invariant inner product of two vectors x and y in $\mathcal{M}$, with components x^μ and y^μ, is given by

$$xy = x^\mu y^\mu g_{\mu\nu}, \tag{4.1}$$

$(g_{\mu\nu}) = \mathrm{diag}(1,-1,-1,-1)$ being the metric tensor.

A Lorentz transformation $\Lambda : \mathcal{M} \rightarrow \mathcal{M}$ is a linear transformation satisfying $(\Lambda x)(\Lambda y) = xy$. The set of all Lorentz transformations forms the Lorentz group L. From Eq. (4.1) follows that every $\Lambda \in L$ satisfies following equation (treating g and Λ as matrices):

$$\Lambda^T g \Lambda = g. \tag{4.2}$$

From this equation follows that $\det\Lambda^2 = 1$ and thus $\det\Lambda = \pm 1$. The 00-component of the equation 4.2 reads:

$$\left(\Lambda_0^0\right)^2 - \sum_{i=1}^{3} \left(\Lambda_0^i\right)^2 = 1. \tag{4.3}$$

what leads to $|\Lambda_0^0| \geq 1$. Thus the group L consists of four topological components:

$$
\begin{aligned}
L_+^\uparrow & : \det\Lambda = +1 \quad \Lambda_0^0 \geq 1 \qquad \text{contains identity} \\
L_-^\uparrow & : \det\Lambda = -1 \quad \Lambda_0^0 \geq 1 \qquad \text{contains space inversion} \\
L_+^\downarrow & : \det\Lambda = +1 \quad \Lambda_0^0 \leq -1 \qquad \text{contains space-time inversion} \\
L_-^\downarrow & : \det\Lambda = -1 \quad \Lambda_0^0 \leq -1 \qquad \text{contains time inversion}
\end{aligned}
$$

Only $L_+^\uparrow$ component is a group itself - it contains the identity element. This subgroup is called *restricted* Lorentz group. This group is not simply connected, since it entails not simply connected rotation group, whose fundamental group is a cyclic group of order 2. The simply connected covering group of the Lorentz group is the group of 2×2 complex matrices with determinant 1 - the group $SL(2,C)$. The covering homomorphism

$$\Lambda : \begin{cases} SL(2,C) & \rightarrow L_+^\uparrow \\ A & \mapsto \Lambda(A) \end{cases}$$

is declared in the following way. First a bijective map from the Minkowski space into the space of 2×2 matrices is defined via:

$$x \mapsto \underset{\sim}{x} = x^0 \mathbf{1} + \mathbf{x} \cdot \vec{\sigma} = \begin{pmatrix} x^0 - x^3 & -x^1 + ix^2 \\ -x^1 - ix^2 & x^0 + x^3 \end{pmatrix}. \tag{4.4}$$

Furthermore following equation holds:

$$\det \underset{\sim}{x} = \mathrm{x}^2, \tag{4.5}$$

and finally a Lorentz transformation $\Lambda(A)$ can be defined as:

$$\underset{\sim}{\Lambda(A)x} = A \underset{\sim}{x} A^*. \tag{4.6}$$

In the next step irreducible representations of the Lorentz group, which are the objects of interest, are explored.

4.2 Spinor representations of SL(2,C)

A field $\psi(x)$ is a function with some components which transform in a definite way under the Lorentz transformations:

$$\psi'(x') = D(A)\psi(x), \qquad x' = \Lambda(A)x, \qquad A \in SL(2, C). \tag{4.7}$$

The group $SL(2, C)$ supersedes the Lorentz group and $D(A)$ is a matrix representation of $SL(2, C)$. The fields can be classified according to irreducible representations of $SL(2, C)$. The group $SL(2, C)$ has exactly two fundamental representations, all other matrix representations are direct sums of these two.

The defining representation is described by:

$$D^{\frac{1}{2}0}(A) = A \tag{4.8}$$

The group acts naturally upon the two dimensional complex vector space $\mathbb{C}^2$ whose elements are called *spinors*. Such spinor Ψ has two complex components:

$$\Psi = \begin{pmatrix} \Psi_1 \\ \Psi_2 \end{pmatrix}. \tag{4.9}$$

The spinor transformation law reads:

$$\Psi'_A = A_A^{\ B}\Psi_B, \qquad A \in SL(2, C). \tag{4.10}$$

Only undotted indices are used for spinors in the defining representation.

The conjugate representation is described by:

$$D^{0\frac{1}{2}}(A) = \bar{A}, \tag{4.11}$$

where $\bar{A}$ is the complex conjugate of A. This representation acts on complex conjugated spinors $\bar{\Psi} = (\Psi_{\dot{A}})$ which transform analogue to the Ψ's:

$$\Psi'_{\dot{A}} = A_{\dot{A}}^{\ \dot{B}}\Psi_{\dot{B}}, \qquad A \in SL(2, C). \tag{4.12}$$

Both representations are inequivalent and dotted indices are reserved for the spinors of the conjugate representation.

A general spinor s of type (j, k) is a tensor with complex components $s_{A_1 \cdots A_{2j}, \dot{A}_1 \cdots \dot{A}_{2k}}$ whose transformation properties are implied by this notation. The tensor should be symmetric under permutations of the first 2j undotted and the last 2k dotted indices. It can be shown that the representation D^{jk} of the $SL(2, C)$ which acts on the space of all spinors of type (j, k) is irreducible. The dimension of this representation space is $(2j + 1)(2k + 1)$ and this dimension is also assigned per definition to the representation D^{jk}.

If the representation D^{jk} is limited on the subgroup $SU(2)$, the defining and conjugate representations become equivalent and the representation D^{jk} becomes the reducible representation $D^j \otimes D^k$ of the $SU(2)$. It can be decomposed into irreducible parts, as it is done in the theory of angular momentum. The decomposition reads in terms of dimensions:

$$(2j + 1)(2k + 1) = \sum_{s=|j-k|}^{j+k} s. \tag{4.13}$$

Now a connection between fields and corresponding spin can be established: If a field $\psi(x)$ transforms under Lorentz-transformations according to the irreducible representation D^{jk} of $SL(2,C)$ it is called an irreducible field. It can possess following spin quantum numbers:

$$s = |j - k|, |j - k| + 1, \ldots, j + k. \tag{4.14}$$

However, this connection only shows which particle species can be potentially described by the field under consideration, it is imaginable that some possible spin values do not occur. The vector field $A_\mu(x)$, for example, is a $(\frac{1}{2}, \frac{1}{2})$ spinor and can describe spin-1 and spin-0 particles. However, it is possible to isolate the spin-1 part and to suppress the spin-0 contribution[2], as done in electrodynamics.

To perform spinorial calculations, some elements of spinor algebra are introduced.

4.3   Spinor algebra

The spinor index is raised and lowered with the spinor metric ϵ^{AB}:

$$\epsilon^{AB} = \begin{pmatrix} 0 & 1 \\ -1 & 0 \end{pmatrix} = \epsilon_{AB} = \epsilon^{\dot{A}\dot{B}} = \epsilon_{\dot{A}\dot{B}} \tag{4.15}$$

Eq. 4.15 implies that $\epsilon^{AB} = -\epsilon^{BA}$, and it is therefore necessary to raise the indices in a well defined order. The order used in this work is :

$$\Psi^B = \Psi_A \epsilon^{AB} \qquad \Psi_{\dot{A}} = \epsilon_{\dot{A}\dot{B}} \Psi^{\dot{B}}. \tag{4.16}$$

The spinorial inner product between two Weyl spinors is defined by:

$$\langle \Psi_1 \Psi_2 \rangle \equiv \Psi_{1A} \Psi_2{}^A, \qquad \langle \Psi_1 \Psi_2 \rangle^* = \Psi_{1\dot{A}} \Psi_2{}^{\dot{A}}. \tag{4.17}$$

From the definition of the inner product follows that:

$$\langle \Psi_1 \Psi_2 \rangle = - \langle \Psi_2 \Psi_1 \rangle, \tag{4.18}$$

and in particular that

$$\langle \Psi \Psi \rangle = 0. \tag{4.19}$$

The map from Minkowski vectors into Weyl spinors was already introduced, hence the momentum $K^{\dot{A}B}$ in spinor language is defined by:

$$K^{\dot{A}B} \equiv \sigma^{\mu\dot{A}B} K_\mu = \sigma_\mu^{\dot{A}B} K^\mu = \begin{pmatrix} K_0 - K_3 & -K_1 + iK_2 \\ -K_1 - iK_2 & K_0 + K_3 \end{pmatrix}, \tag{4.20}$$

where $\sigma^{\mu\dot{A}B} = (\sigma^0, \vec{\sigma})$ is a spin tensor, an object with both Lorentz and spinor indices, and K^μ is an arbitrary Minkowski four vector with energy component $K^0 = K_0$, and the momentum part $\vec{K}$. The spin tensor $\sigma^{\mu\dot{A}B}$ satisfies a number of relations, in particular:

$$\left(\sigma_{\mu\dot{A}B} \right)^* = \sigma_{\mu\dot{B}A}, \tag{4.21}$$

$$\sigma_{\mu\dot{A}B} \sigma_\nu^{\dot{A}B} = 2g_{\mu\nu}, \tag{4.22}$$

$$\sigma_{\mu\dot{A}B} \sigma_{\dot{C}D}^\mu = 2\epsilon_{\dot{A}\dot{C}} \epsilon_{BD}. \tag{4.23}$$

---

[2]Lorenz gauge condition of electrodynamics excludes spin-0 photons

The four vector can be reconstructed from the spinorial object $K^{\dot{A}B}$:

$$K^\mu = \frac{1}{2}\sigma^\mu_{\dot{A}B}K^{\dot{A}B} = \frac{1}{2}\sigma^{\mu\dot{A}B}A_{\dot{B}}. \tag{4.24}$$

The Minkowski inner product can also be translated into spinorial notation:

$$(K \cdot P) = K^\mu P_\mu = \frac{1}{2}\sigma^\mu_{\dot{A}B}K^{\dot{A}B}\frac{1}{2}\sigma_{\mu\dot{C}D}P^{\dot{C}D} = \frac{1}{2}K^{\dot{A}B}P_{\dot{A}B} \equiv \{K,P\}. \tag{4.25}$$

The last equality serves as a definition of the inner product of two momenta in spinor notation.

In this work we are dealing with massless particles and hence with light-cone vectors, $K^2 = 0 = \{K,K\}$. From

$$K_{\dot{A}B}K^{\dot{A}B} = 2(K_{\dot{1}1}K_{\dot{2}2} - K_{\dot{1}2}K_{\dot{2}1}) = 0, \tag{4.26}$$

follows that $K_{\dot{A}B}$ has $\det K_{\dot{A}B} = 0$. By virtue of Eq. (4.21) $K_{\dot{A}B}$ is a hermitian matrix, and the last equation implies that one of the eigenvectors is equal zero. Hence, the matrix can be written as a projection onto the eigenvector corresponding to the non-zero eigenvalue:

$$K_{\dot{A}B} = 2K_0 l_{\dot{A}}l_B. \tag{4.27}$$

Redefinition of the non-zero eigenvector to $k_A = \sqrt{2K_0}l_A$ leads to:

$$K_{\dot{A}B} = k_{\dot{A}}k_B. \tag{4.28}$$

A spinor k_A corresponding to a light-cone momentum K_μ is called momentum spinor. It is convenient that capitals denote space-time momenta in spinor language, and lower case characters denote the corresponding momentum spinors. The normalised eigenvectors k_A can be written explicitly in terms of momentum components, but this is not important for the present work and can be found in [27].

The Minkowski inner product of two light-cone vectors can also be expressed in terms of momentum spinors:

$$(K \cdot P) = \frac{1}{2}\{K,P\} = \frac{1}{2}K_{\dot{A}B}P^{\dot{A}B} = \frac{1}{2}k_B p^B k_{\dot{A}}p^{\dot{A}} = \frac{1}{2}\langle kp\rangle \langle kp\rangle^* = \frac{1}{2}|\langle kp\rangle|^2 \tag{4.29}$$

It turns out, that the matrix elements become more compact when expressed in terms of spinorial inner products, which are more fundamental quantities than the Minkowski products. This is also true for spinors in comparison to four vectors, as it is emphasised in [52]. As the essential spinor algebra is presented, the spinor representations for fermionic spin-1/2 and bosonic spin-1 particles are introduced.

4.4 Spin-1/2 particles

The fields corresponding to spin-1/2 particles transform in the representations $D^{\frac{1}{2}0}$ and $D^{0\frac{1}{2}}$ in accordance with the definition given above. After translation of the four gradient $\partial_\mu = (\partial_0, \nabla)$, which transforms like a four vector under Lorentz transformations, to the Weyl spinor notation:

$$\left(\partial^{\dot{A}B}\right) = \begin{pmatrix} \partial_0 - \partial_3 & -\partial_1 + i\partial_2 \\ -\partial_1 - i\partial_2 & \partial_0 + \partial_3 \end{pmatrix} = \partial_0 + \vec{\sigma}\nabla, \tag{4.30}$$

the Dirac theory is defined by the following system of coupled differential equations:

$$
\begin{aligned}
i\partial^{\dot{A}B}\Psi_B &= m\Phi^{\dot{A}}, \\
i\partial_{\dot{A}B}\Phi^{\dot{A}} &= m\Psi_B.
\end{aligned}
\tag{4.31}
$$

The term m, which is interpreted as a particle mass, couples the spinors Ψ_A and $\Phi_{\dot{A}}$ which transform in the different representations of the $SL(2,C)$ (see above). The Dirac theory uses two fields for a description of the spin $1/2$ particles. These two spinors correspond with the two helicity states of massless fermions, as it will be shown in the description of the Weyl equations.

The Dirac equations can be reformulated as one equation by combining two spinors into one four-dimensional bispinor and by introducing γ matrices:

$$
(\gamma^\mu)^a{}_b = \begin{pmatrix} 0 & \sigma^\mu_{\dot{B}A} \\ \sigma^{\mu\dot{A}B} & 0 \end{pmatrix}.
\tag{4.32}
$$

With this definition the Dirac equation reads:

$$
(i\gamma^\mu\partial_\mu - m)\,\Psi(x) = 0, \qquad \Psi(x) = \begin{pmatrix} \Psi_A \\ \Phi^{\dot{B}} \end{pmatrix}
\tag{4.33}
$$

The equivalence with the usual definition of left-, and right-handed spinors is given via the definition of $\gamma^5 = i\gamma^0\gamma^1\gamma^2\gamma^3$. It follows:

$$
\Psi_R = \Psi_+ = \frac{1}{2}(1+\gamma^5)\Psi = \begin{pmatrix} \Psi_A \\ 0 \end{pmatrix}
\tag{4.34}
$$

$$
\Psi_L = \Psi_- = \frac{1}{2}(1-\gamma^5)\Psi = \begin{pmatrix} 0 \\ \Phi^{\dot{B}} \end{pmatrix}
\tag{4.35}
$$

If one sets $m = 0$ in Eq. (4.31) one is led to two uncoupled equations of motion - these are the Weyl equations:

$$
\begin{aligned}
\partial^{\dot{A}B}\Psi_B &= 0 &\equiv&& \partial_0\Psi(x) &= -\vec{\sigma}\nabla\Psi(x) \\
\partial_{\dot{A}B}\Phi^{\dot{A}} &= 0 &\equiv&& \partial_0\Phi(x) &= \vec{\sigma}\nabla\Phi(x)
\end{aligned}
\tag{4.36}
$$

The left-right asymmetry of this equations can be understood after examination of the plane wave solutions:

$$
\Psi(x) = \Psi_0 e^{-ipx}, \qquad p = (p^\mu) = (|\vec{p}|, \vec{p}),
\tag{4.37}
$$

where the spinor Ψ_0 describes spin orientation. From the Weyl equation and $\vec{n} = \vec{p}/|\vec{p}|$ follows:

$$
\vec{\sigma}\vec{n}\Phi_0 = -\Phi_0.
\tag{4.38}
$$

Thus the spin direction of Φ_0 is constrained to be antiparallel to the momentum. This spinor describes a left handed particle, as stated earlier.

The Weyl equations can be transformed to the momentum space. The first equation becomes:

$$
K^{\dot{A}B}\tilde{\Psi}_B = k^{\dot{A}}k^B\tilde{\Psi}_B = 0,
\tag{4.39}
$$

with $K^{\dot{A}B}$ the four momentum of the fermion, $\{K, K\} = 0$ and k_A its momentum spinor. The treatment of the second equation is analogue. Both equations can be solved leading to description of the two helicity states in momentum space. All parameters of the solutions can be derived from the orthogonality condition and the completeness relation. Final results are:

$$u_+\left(\vec{K}\right) = \begin{pmatrix} k_A \\ 0 \end{pmatrix} \qquad \text{end} \qquad u_-\left(\vec{K}\right) = \begin{pmatrix} 0 \\ k^{\dot{A}} \end{pmatrix} \qquad (4.40)$$

The solution u_+ corresponds with the $+$ helicity state and u_- with the $-$ helicity state respectively.

4.5   Spin-1 particles

The fields of spin-1 particles transform in the $D^{\frac{1}{2}\frac{1}{2}}$ representation. It is not important whether the particles carry colour (q.v. next section), thus photons and gluons can be treated on equal footing. The equation of motion for a free massless spin-1 particle in the Lorenz gauge

$$\partial \cdot A = 0 \qquad (4.41)$$

reads

$$\Box A^\mu = 0. \qquad (4.42)$$

The general solution can be decomposed in plane waves:

$$A^\mu = \int d^4k \left(\epsilon^\mu(k)e^{ikx} + \epsilon^{*\mu}(k)e^{-ikx} \right). \qquad (4.43)$$

The Lorenz condition reduces four degrees of freedom of A^μ to three, which implies that ϵ^μ still has the gauge freedom

$$\epsilon'^\mu = \epsilon^\mu + \xi K^\mu, \qquad (4.44)$$

since massless spin-1 fields should have two degrees of freedom, represented by right- and left handed complex helicity vectors ϵ^μ_λ with $\lambda = \pm 1$. The last statement follows from the analysis of the representations of the Poincaré group [12]. Following orientation and normalisation conditions imposed upon ϵ^μ_λ determine its form:

$$\begin{align}
\{K, K\} &= 0 \qquad &(4.45)\\
\{\epsilon_\lambda, K\} &= 0 \qquad &(4.46)\\
\{\epsilon_\lambda, \epsilon_\lambda\} &= 0 \qquad &(4.47)\\
\epsilon_\lambda^{\dot{B}A} &= \left(\epsilon_{-\lambda}^{\dot{A}B}\right)^* \qquad &(4.48)\\
\{\epsilon_\lambda, \epsilon_{-\lambda}\} &= -2 \qquad &(4.49)
\end{align}$$

with $K^{\dot{A}B}$ the momentum of the particle. For transverse vectors an extra condition can be stated:

$$\vec{\epsilon}_\lambda \cdot \vec{K} = 0. \qquad (4.50)$$

This last relation reduces the number of degree of freedoms to two and can be satisfied if ϵ is redefined via a gauge transformation. The helicity vectors satisfying all constraints can be written in the following form:

$$\epsilon_+^{\dot{A}B} = \sqrt{2}\frac{k^{\dot{A}}b^B}{\langle kb\rangle} \tag{4.51}$$

$$\epsilon_-^{\dot{A}B} = \sqrt{2}\frac{b^{\dot{A}}k^B}{\langle kb\rangle^*} \tag{4.52}$$

with b^A an arbitrary spinor not proportional to k^A. The overall phase factor is set here to zero.

The gauge freedom of the helicity vectors is still manifest in the spinor language, even if the spinors satisfy all defining conditions, and is equivalent to a different choice for b^A. This freedom is crucial for computations, since b^A can be set to the momenta of other spinors present in a scattering process, which leads to cancellation of many diagrams.

Feynman diagrams of QCD processes contain not only their space-time dynamics but also a complex colour structure, which enters the computations in form of products and traces of representation matrices. To reduce the complexity of calculations, colour and dynamics of the QCD processes are treated separately.

4.6   Colour decomposition in QCD

The tree level amplitude for a scattering process can be written as a sum of gauge invariant functions containing the space-time dynamics, each with a certain colour structure:

$$\mathcal{T} = ig^{n-2} \sum_{perms} F(T^A, i, N)K_F(P). \tag{4.53}$$

The matrix element depends on a phase space point P, a set of n particle momenta and helicities. The strong coupling constant g is separated from the dynamics. The function $F(T^A, i, N)$ is built up from representation matrices and colour indices. The open indices of the representation matrices can only be the quark and antiquark colour indices. The set of F's is independent and the decomposition of $\mathcal{T}$ in terms of F's with Eq. (4.53) leads to a set of gauge invariant expressions $K_F(P)$ in a unique way. These $K_F(P)$ are called subamplitudes. They are functions of momenta and helicities only, and can be obtained with the help of colour-ordered Feynman rules. The sum runs over all permutations of identical particles which change F.

The colour functions F can be read out from the Feynman diagrams with the help of the *colour flow* concept, which is just a way of applying QCD Feynman rules. In this concept the colour flows from external line to external line in a defined direction (anticlockwise in this work). Depending on the kind of external lines, representation matrices with some indices are added to a chain, which is just a product of such matrices (Kronecker delta can also be a chain). A trace occurs when the chain is closed and the only non contacted indices are identical. To be able to use colour flow, Feynman diagram should be drawn in planar fashion (no crossed lines) with all particles outgoing.
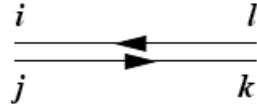
Figure 4.1: The double line notation for the propagator of a hermitian matrix field [53] .

In the following the concept for gluon scattering is shown, which is essential for the present work. First the spin 1 field Lagrangian is written in a particular gauge: the *Gervais-Neveu gauge* . The QCD gauge group is $SU(N = 3)$ but the discussion is carried out for an arbitrary N. For convenience the generators are normalised slightly different in comparison with chapter 1.4.2:

$$Tr\left(T^A T^B\right) = \delta^{AB}, \tag{4.54}$$

which leads to following commutation relations:

$$\left[T^A, T^B\right] = i\sqrt{2} f^{ABC}\left(T^C\right). \tag{4.55}$$

To obtain the gauge Lagrangian in the Gervais-Neveu gauge, the matrix-valued field strength is rewritten as antisymmetric part of the matrix-valued complex tensor $H_{\mu\nu}$:

$$H_{\mu\nu} \equiv \partial_\mu A_\nu - \frac{ig}{\sqrt{2}} A_\mu A_\nu \tag{4.56}$$

The Gervais-Neveu gauge fixing term $-1/2 Tr(H^\mu_\mu H^\nu_\nu)$ leads to the following gauge Lagrangian in terms of $H_{\mu\nu}$:

$$\mathcal{L}_{gauge} = \mathcal{L}_{class} + \mathcal{L}_{gauge-fixing} = -\frac{1}{2}\text{Tr}(\text{H}^{\mu\nu}\text{H}_{\mu\nu} - \text{H}^{\mu\nu}\text{H}_{\nu\mu}) - \frac{1}{2}\text{Tr}(\text{H}^\mu_\mu \text{H}^\nu_\nu), \tag{4.57}$$

which can be rewritten back in terms of the A^μ fields (several integration by part steps were performed) :

$$\mathcal{L} = Tr(-\frac{1}{2}\partial^\mu A^\nu \partial_\mu A_\nu - i\sqrt{2}g(\partial^\mu A^\nu)A_\nu A_\mu + \frac{1}{4}g^2 A^\mu A^\nu A_\mu A_\nu). \tag{4.58}$$

This Lagrangian has a rather simple structure in terms of the matrix-valued fields, which should be used for calculations instead of the coefficient fields. The gluon propagator follows from the first term of the Lagrangian and reads (completeness relations for the representation matrices were used):

$$\tilde{\Delta}^{j\,l}_{i\,k}(k^2) = \frac{\delta_i^{\,l}\delta_k^{\,j}\, g_{\mu\nu}}{k^2 - i\epsilon}. \tag{4.59}$$

The propagator can be represented diagrammatically as a double line, with arrows pointing from up to down indices, as shown in Fig. 4.1. Since all interactions involve matrix products, with an up index from one field contracted with a down index from an adjacent field, the vertices follow the pattern shown in Fig 4.2. The n-point vertex of this type has only an n-fold cyclic symmetry.
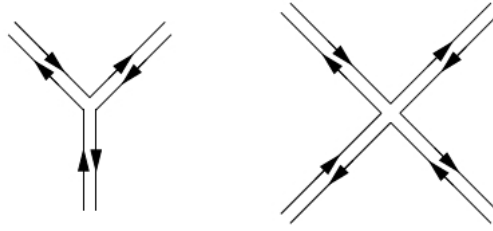
Figure 4.2: 3- and 4-point vertices in the double-line notation [53].

As example, three of eighteen possible Feynman diagrams for the scattering of two gluons are shown in Fig. 4.3. The remaining 15 diagrams are obtained by making non-cyclic permutations of the labels 1, 2, 3, 4, which is equivalent to making unrestricted permutations of the labels 2, 3, 4. Each external line carries a factor of T^{A_i}, with its matrix indices contracted by following the arrows backward through the diagrams. From this example one can infer that the value of any diagram with n external gluon lines is proportional to $\mathrm{Tr}(\mathrm{T}^{A_1}\dots\mathrm{T}^{A_n})$.
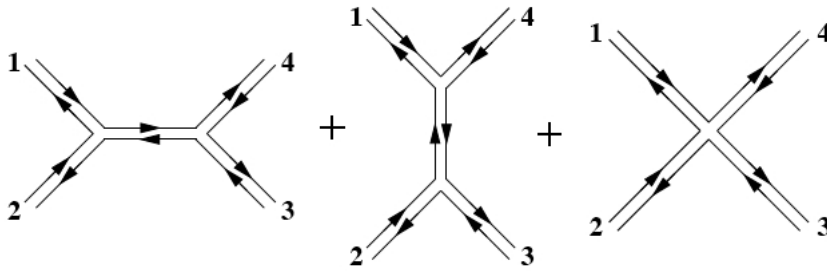
Figure 4.3: Three example tree diagrams with four external lines. All other diagrams can be obtained by permutations of the labels 2, 3 and 4 [53].

The double-line notation in the Gervais-Neveu gauge should have motivated the general concept of colour flow, where a representation matrix $(T^A)_{i_L i_R}$ is added to the chain for each external gluon with a colour A. The matrix indices i_L and i_R will be contracted with indices i_R and i_L coming from the previous and the next colour objects, thus leading always to traces in case of pure gluon scattering as stated above. The ordering of the A_i indices in the trace is determined by the counterclockwise ordering of the labels on external lines. In case of incoming quarks Kronecker deltas with indices $i i_R$ for a quark with colour i and $i_L j$ for an antiquark with colour j are added to the chain. The rules for quarks can also be motivated by the double-line notation [53]. It is evident that only quark indices can occur in chains as open indices. The Feynman rules for a theory stripped from the colour structure are called *colour-ordered rules*.

Computing the square of an amplitude involves evaluation of expressions of the type:

$$Tr(T^{A_1}T^{A_2}T^{A_3}T^{A_4})\left[Tr(T^{A_1}T^{A_2}T^{A_4}T^{A_3})\right]^*, \qquad (4.60)$$
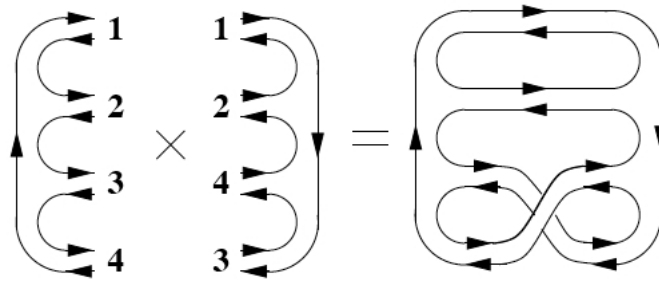
Figure 4.4: Evaluation of products of traces of representation matrices. Each of two closed single-line loops yields a factor of N [53].

with all repeated indices summed. Diagrammatically such computation is shown in Fig. 4.4. Each single-line loop yields a factor of $\delta_i^{\ i} = N$. It follows that the absolute square of any particular trace provides a factor on N^4, and the product of any trace times the complex conjugate of any other trace yields a factor of N^2.

The techniques discussed in this section will be used for calculations of tree-level multi gluon scattering. Furthermore a helicity amplitude based approximation for QCD matrix elements will be introduced in the next chapter.

5

Hadroproduction of Jets

The diagram technique for QCD calculations, developed so far, is of little use for the present work, since it describes quark and gluon scattering amplitudes which are not "physical". Quarks and gluons are confined inside colourless bound states, the *hadrons*, and cannot appear as incoming and outgoing particles in a scattering event. The physical particles which are scattered at the LHC are protons, and therefore cross sections for processes involving protons (or in general hadrons) as initial states are needed. Since the present work deals only with hadronic final states, it is sufficient to find a description for hadroproduction of jets. The solution to this problem is the QCD improved parton model, in which hadrons scattered at high energies are treated as collections of free quarks and gluons (generally called *partons*), which participate independently in the scattering process. In order to extract quantitative results, knowledge of the distribution of the hadron energy and momentum among its constituent partons is needed. This is described by the *parton distribution functions*, which cannot be calculated from first principles and have to be determined by experiments. This chapter introduces the QCD improved parton model, as well as the definition of jets used in this work, and demonstrates the application of the methods developed in the previous chapter for the two-jet cross section. It introduces furthermore the Special Helicity Approximation (SPHEL) usable for predictions of QCD multijet production. This approximation will be used in the following chapters as a basis for a jet based variable for description of QCD multijet processes.

5.1 The QCD improved parton model

The cross section for a hard scattering process initiated by two hadrons with the four-momenta P_1 and P_2 can be written as:

$$\sigma(P_1, P_2) = \sum_{i,j} \int dx_1 \, dx_2 \, f_i(x_1, \mu^2) f_j(x_2, \mu^2) \, \hat{\sigma}_{ij}(p_1, p_2, \alpha_S(\mu^2), Q^2/\mu^2), \quad (5.1)$$

where $p_1 = x_1 P_1$ and $p_2 = x_2 P_2$ are the momenta of the partons participating in the hard scattering process, and Q is the characteristic scale of this process. The
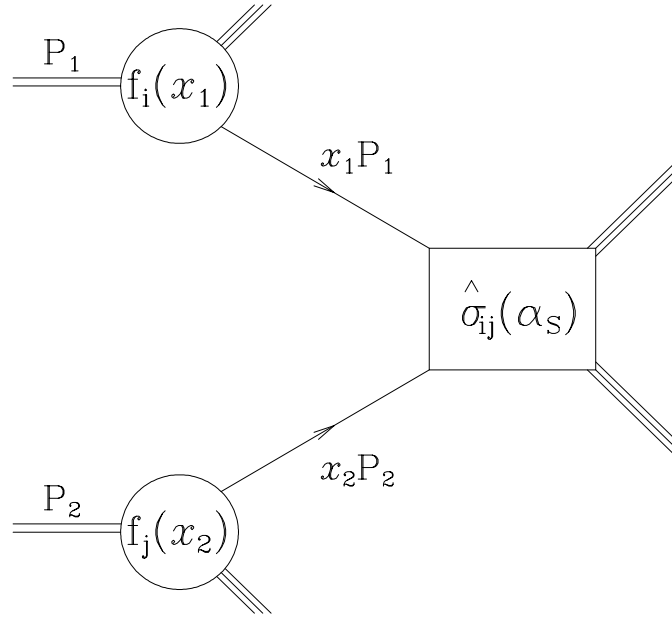
Figure 5.1: Schematic description of a hard scattering process [25].

functions $f_i(x, \mu^2)$ are quark or gluon distributions, which give the probability to find a quark or a gluon with a fraction x of the hadron momentum at a factorisation scale μ. This scale is an arbitrary parameter, which separates the long- and short-distance physics. A parton emitted with a transverse momentum less than μ is absorbed into the parton distribution and does not take part in the hard process, contrary to a parton with large transverse momentum, which is a part of the short-distance cross section $\hat{\sigma}_{ij}$. Because of asymptotic freedom, the coupling at high energies is small, and the short-distance cross section can be calculated as a perturbation series with methods developed in chapters 1.4.2 and 4. The scale μ should be chosen to be of the order of the hard scale Q and is set in this work equal to the renormalisation scale, following Ref. [25]. Figure 5.2 shows the parton distribution functions from the CTEQ group (CTEQ 6.1) for gluons, up, down, and anti-up quarks evaluated at $\mu^2 = Q^2 = 100~GeV^2$. The ability to separate the total cross section into the short-range part, which is insensitive to the physics at the low momentum scales and involves only high momentum transfer, and the long-distance part, which is absorbed into the description of the incoming hadrons, is rooted in the *factorisation theorem*, which can be proved to all orders in perturbation theory [25].

Figure 5.1 shows a schematic description of the hard scattering process.

5.2   Kinematics and jet algorithms

The incoming partons of a hard scattering process have generally different fractions of incoming hadrons momenta which are assumed to be purely longitudinal. As a
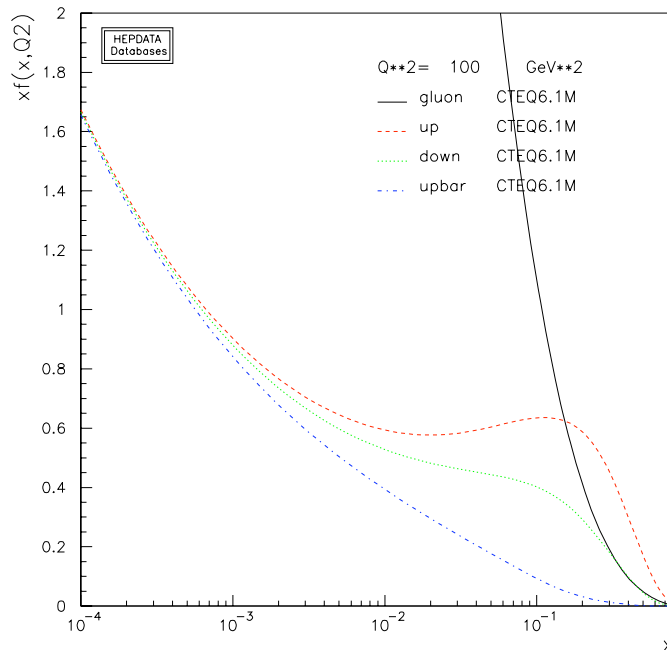
Figure 5.2: The CTEQ 6.1 parton distribution functions evaluated at a $\mu = Q$ of 10 GeV.

result the centre of mass frame of the hard process will be in general longitudinally boosted with respect to the one of incoming hadrons. Therefore, it is convenient to use quantities with simple transformational behaviour under longitudinal boosts. Such quantities are the rapidity y, the transverse momentum p_T and the azimuthal angle ϕ. The rapidity y is defined by:

$$y = \frac{1}{2} \left(\frac{E + p_z}{E - p_z} \right), \tag{5.2}$$

and is additive under boosts along the z-axis. The last property implies that rapidity differences are invariant under such boosts. The four momentum of a particle with mass m can be written as:

$$
\begin{aligned}
p^\mu &= (E, p_x, p_y, p_z) \\
&= (m_T \cosh y, p_T \sin \phi, p_T \cos \phi, m_T \sinh y),
\end{aligned}
\tag{5.3}
$$

where the transverse mass is defined as $m_T = \sqrt{p_T^2 + m^2}$. In the limit $m \to 0$ the rapidity coincides with the pseudorapidity η defined in chapter 3.

After the hard interaction, partons undergo the hadronisation process and emerge as bunches of high energy hadrons collimated in the direction of the original parton in the detector. These bunches are called jets. Due to the current limitation of the understanding of non-perturbative QCD it is impossible to predict the exact patterns of produced hadrons. Instead, calculations in terms of quarks and gluons are related to the observations in terms of jets. In order to establish a link between both entities, well defined jet-finding algorithms are applied to the predicted partonic configurations as well as to the observed hadrons. Though partonic and hadronic jets are not equivalent there is a strong evidence [54] that both distributions can be compared with controlled accuracy.

The cluster-type k_t [55–57] jet finder, implemented as FastJet algorithm [58], was selected for the present work[1]. The cluster-type jet finders are based on successive pair-wise recombinations of particles and have the important property of infrared and collinear safety. At the parton level infrared safety means that calculated cross sections are finite despite the infrared divergences in the single diagrams. Unitarity ensures that the sum of the probabilities for one of the divergent configuration to happen or not to happen is 1. The infrared safety on physical hadron level means, that measured jet variables and/or definitions of a jet do not change when a soft gluon is radiated or when a parton divides into collinear partons.

The k_t jet finder [57, 58] computes first the k_t distance d_{ij} of all pairs of protojets i, j and additionally the beam distance $d_{iB} = k_{ti}$ for each single protojet i. In the next step the minimum distance d_{min} is selected out of all possible d_{ij} and d_{iB}. If d_{min} is a d_{ij}, protojets i and j are merged via summation of their four momenta (alternative recombination schemes are possible); and if it is a d_{iB} the protojet i is selected as final jet and removed from the list of protojets. These steps are repeated until no protojets are left on the list. The distances are defined in the following way:

$$d_{ij} = min(k_{ti}^2, k_{tj}^2)R_{ij}^2/R^2, \tag{5.4}$$

with

$$R_{ij}^2 = (\eta_i - \eta_j)^2 + (\phi_i - \phi_j)^2, \tag{5.5}$$

where k_{ti}, η_i, and ϕ_i are the transverse momentum, rapidity and azimuth of protojet i, and R is a user chosen scaling factor.

The k_t algorithm is suitable for hadron colliders, since only quantities which are invariant under longitudinal boosts are used. The algorithm is furthermore collinear safe, since collinear partons originating from one particle are immediately recombined, leading to the same result as if the parton had not divided. The high k_t jets are similarly not affected by the $k_t^{softjet} \to 0$ limit whether they contained a low k_t sub-jet or not. The algorithm possesses furthermore following properties: it maps every hadron from the final state to exclusively one jet without overlap, and it can resolve nearby high energetic objects like jets originating from decays of highly boosted particles [59] or high energetic jets from multiparton production. The general good properties of the algorithm together with the last property were the decisive factors to choose this jet finder for the present work.

The FastJet version of the k_t algorithm reduces the algorithm complexity from N^3, to $N \ln N$, N being the number of particles.

5.3   Two-jet cross sections

Two jet events are the result of the scattering of two partons, one from each hadron respectively, into two high energetic partons, which form hadronic jets. Momentum conservation forces the two final state partons to have equal and opposite momenta in the centre of mass frame of the hard process. If one neglects the small intrinsic transverse momentum of the incoming partons and assumes that exactly two partons

---

[1]This work uses the FastJet implementation of the k_t algorithm integrated in the software framework of the CMS experiment (CMSSW_1_6_12)

in the final state were created, the jets in the laboratory frame will be back-to-back in azimuth and balanced in transverse momentum.

The parton cross section for a

$$\text{parton}_1(p_1) + \text{parton}_2(p_2) = \text{parton}_3(p_3) + \text{parton}_4(p_4) \tag{5.6}$$

scattering process, described by a matrix element $\mathcal{T}$, reads [25]:

$$\frac{E_3 E_4 d^6 \hat{\sigma}}{d^3 p_3 d^3 p_4} = \frac{1}{2\hat{s}} \frac{1}{16\pi^2} \overline{\sum} |\mathcal{T}|^2 \delta^4(p_1 + p_2 - p_3 - p_4), \tag{5.7}$$

where $\overline{\sum}$ denotes the average over the initial and sum over the final-state spins and colours, and $\hat{s} = (p_1 + p_2)^2$. The cross section contains contributions from processes with different initial and final state partons (quarks and/or gluons), and hence can be written as a sum of terms each representing the contribution from one such process. The result for the two jet inclusive cross section is [25]:

$$\begin{aligned}
\frac{d^3\sigma}{dy_3 dy_4 dp_T^2} =& \frac{1}{16\pi s^2} \sum_{i,j,k,l=q,\bar{q},g} \frac{f_i(x_1, \mu^2)}{x_1} \frac{f_j(x_2, \mu^2)}{x_2} \\
&\times \overline{\sum} |\mathcal{T}(ij \to kl)|^2 \frac{1}{1 + \delta_{kl}}.
\end{aligned} \tag{5.8}$$

The indices (i, j) stand for incoming and (k, l) for outgoing partons, s is the square of the centre of mass energy of the hadronic process, $f_i(x, \mu)$ represent the distributions for the parton type i ($i = u, \bar{u}, d, \bar{d}, g, \ldots, etc.$), evaluated at the momentum scale μ, and y_3 and y_4 are the rapidities of the outgoing partons. The Kronecker delta introduces the statistical factor necessary for identical final state partons. The momentum fractions x_1 and x_2 can be determined from the rapidities y_3 and y_4 via momentum conservation:

$$x_1 = \frac{1}{2} x_T (e^{y_3} + e^{y_4}), \; x_2 = \frac{1}{2} x_T (e^{-y_3} + e^{-y_4}), \tag{5.9}$$

where $x_T = 2p_T / \sqrt{s}$.

The scattering angle of massless partons in their centre of mass frame can be determined from the observed rapidities of jets. This angle θ^* is given by:

$$\cos \theta^* = \frac{p_z^*}{E^*} = \frac{\sinh y^*}{\cosh y^*} = \tanh \left(\frac{y_3 - y_4}{2} \right), \tag{5.10}$$

where * denotes quantities in the centre of mass frame. The second equation follows from the definition of the four momentum in terms of rapidity, and the last equation holds, because the rapidities of both jets in the centre of mass frame are equal in magnitude but have opposite signs. It is useful to define the invariant mass of the jet-jet system as additional variable:

$$M_{JJ}^2 = \hat{s} = 4p_T^2 \cosh^2 y^*. \tag{5.11}$$

To compare the theoretical predictions with experimental results one can investigate the angular distribution of jets. The matrix element of the $2 \to 2$ scattering
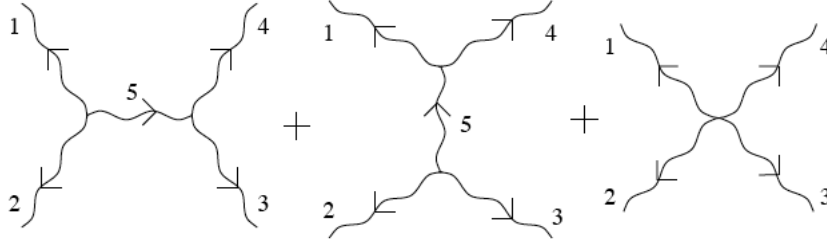
Figure 5.3: Three of eighteen possible Feynman diagrams for scattering of two gluons. Five more diagrams of each of these three types, with external labels 2,3, and 4 permuted also contribute [53].

process is sensitive to the scattering angle in the centre of mass system. Using the transformation

$$dp_T^2 dy_3 dy_4 \equiv \frac{1}{2} s dx_1 dx_2 d\cos\theta^*, \tag{5.12}$$

the differential cross section for a 2-jet system with the invariant mass M_{JJ} to scatter at the angle θ^* in the centre of mass frame can be written as:

$$
\frac{d^2\sigma}{dM_{JJ}^2 d\cos\theta^*} = \\
\sum_{i,j=q,\bar{q},g} \int_0^1 dx_1\, dx_2\, f_i(x_1,\mu^2) f_j(x_2,\mu^2)\delta(x_1 x_2 s - M_{JJ}^2)\frac{d\hat{\sigma}^{ij}}{d\cos\theta^*},
\tag{5.13}
$$

with

$$\frac{d\hat{\sigma}^{ij}}{d\cos\theta^*} = \sum_{k,l} \frac{1}{32\pi M_{JJ}^2} \overline{\sum} |\mathcal{T}(ij \to kl)|^2 \frac{1}{1+\delta_{kl}}. \tag{5.14}$$

Expressions for the leading order matrix elements for all possible processes can be found in [25]. The process $gg \to gg$ has however the largest relative contribution [25] and can be used to demonstrate computational techniques developed in the previous chapter.

5.4   Application of the helicity amplitudes technique

To compute the scattering amplitude for $gg \to gg$ on has to evaluate eighteen Feynman diagrams, three of which are shown in Fig. 5.3. QCD amplitudes can be decomposed into the colour and the dynamical part with Eq. (4.53), and the functions $K_F(P)$ are denoted as partial amplitudes A in case of gluonic scattering [27, 53]. All gluons are treated as outgoing and the tree-level 4-gluon scattering amplitude is then written as:

$$\mathcal{T} = g^2 \sum_{perms} Tr(T^{A_1} \dots T^{A_4}) A(1,2,3,4). \tag{5.15}$$

The diagrams of the Fig.5.3 correspond to the partial amplitude $A(1,2,3,4)$. The partial amplitudes are cyclically symmetric [27, 53],

$$A(2,3,4,1) = A(1,2,3,4), \tag{5.16}$$

which is also true for the general case of n-gluon scattering.

The three- and four-gluon vertices in the Gervais-Neveu gauge are simpler as the one derived in section 1.4.2. The three-gluon vertex factor in the colour-ordered notation is [53]:

$$iV_{\mu_1\mu_2\mu_3}(K_1, K_2, K_3) = -i\sqrt{2}g(K_{1\mu_3}g_{\mu_1\mu_2} + K_{2\mu_1}g_{\mu_2\mu_3} + K_{3\mu_2}g_{\mu_3\mu_1}), \qquad (5.17)$$

while the four-gluon vertex reads:

$$iW_{\mu_1\mu_2\mu_3\mu_4} = ig^2 g_{\mu_1\mu_3}g_{\mu_2\mu_4}, \qquad (5.18)$$

with K_i being a four momentum vector of one external line. Calculations can be simplified further by contracting the vector indices (1,2,3,4) with the incoming polarisations vectors ϵ_i (helicity labels are suppressed):

$$iV_{123} = -i\sqrt{2}g\left[(\epsilon_1\epsilon_2)(K_1\epsilon_3) + (\epsilon_2\epsilon_3)(K_2\epsilon_1) + (\epsilon_3\epsilon_1)(K_3\epsilon_2)\right] \qquad (5.19)$$

$$iW_{1234} = +ig^2(\epsilon_1\epsilon_3)(\epsilon_2\epsilon_4) \qquad (5.20)$$

where the external lines are numbered sequentially, counterclockwise around the vertex. If an attached line is internal, the corresponding polarisation vector is a placeholder for an internal propagator. From the definition of the three and four point vertices and the Feynman diagrams in Fig. 5.3 follows, that every term in the tree-level scattering amplitude includes at least one product of polarisation vectors.

The colour-ordered three-point vertex is antisymmetric on the reflection of the indices $(123 \leftrightarrow 321)$, while the four-point vertex is symmetric on the reflection of the four indices, that implies the general reflection identity for n-gluon scattering:

$$A(n, \ldots, 2, 1) = (-1)^n A(1, 2, \ldots, n) \qquad (5.21)$$

In the next step definitions of the helicity vectors in the Weyl notation are employed:

$$\epsilon_+^{\dot{A}B} = \sqrt{2}\frac{k^{\dot{A}}b^B}{\langle kb\rangle}, \qquad (5.22)$$

$$\epsilon_-^{\dot{A}B} = \sqrt{2}\frac{b^{\dot{A}}k^B}{\langle kb\rangle^*}, \qquad (5.23)$$

where b^A is an arbitrary spinor due to gauge freedom. Having this freedom in choosing b^A one can derive the following general statements. Setting this spinor of all positive helicity polarisation vectors equal to the momentum spinor k^A of one of the negative helicity polarisation vectors leads to the vanishing of many products. Since spinor products are antisymmetric, the product of two identical spinors is equal zero. A product of two arbitrary positive helicity gluons involves such vanishing spinor product, as well as a product of any positive helicity gluon with the particular negative helicity gluon, whose momentum spinor equals b^A. Since every amplitude includes at least one product of polarisation vectors, a non zero amplitude can only occur if there is more than one gluon with helicity different from the helicity of the others. In case of four-gluon scattering[2] there is only one possibility left: two gluons have negative and two gluons positive helicities.

---

[2] From here on all momenta are treated as outgoing leading to the transformation of the amplitudes from $gg \to gg$ to $\emptyset \to gggg$.

One of the non vanishing amplitudes is $A(1^-, 2^-, 3^+, 4^+)$: The gauge spinors are chosen in the following way :

$$b_1^A = b_2^A = k_3^A, \tag{5.24}$$
$$b_3^A = b_4^A = k_2^A. \tag{5.25}$$

This choice leads to the vanishing of all polarisation products, except $(\epsilon_1 \epsilon_4)$. The third Feynman diagram in Fig. 5.3 does not contribute to the process, since it involves a factor of $(\epsilon_1 \epsilon_3)$. The second diagram vanishes, because of the 235 vertex (products: $(\epsilon_2 \epsilon_3)$, $(K_3 \epsilon_2)$, and $((K_5 = -K_2 - K_3)\epsilon_3))$. Only the first diagram is left and must be evaluated. Straightforward calculation and deployment of momentum conservation lead to the result:

$$A(1^-, 2^-, 3^+, 4^+) = \frac{\langle 12 \rangle^4}{\langle 12 \rangle \langle 23 \rangle \langle 34 \rangle \langle 41 \rangle} \tag{5.26}$$

Using cyclic symmetry any other partial amplitude with adjacent negative helicities can be inferred.

$$A(1^+, 2^-, 3^-, 4^+) = \frac{\langle 23 \rangle^4}{\langle 12 \rangle \langle 23 \rangle \langle 34 \rangle \langle 41 \rangle} \tag{5.27}$$

There is only one amplitude left to be calculated : $A(1^-, 2^+, 3^-, 4^+)$ - all others can be determined using cyclic permutations. This amplitude can be either calculated in exactly the same way as the first one, using other gauge spinors assignments or via the technique of the decoupling of a fictitious photon. This technique roots in the observation that the change of the gauge group from $SU(N)$ to $U(N)$ corresponds to the addition of a generator proportional to the identity. This generator commutes with all other generators and hence, there is no interaction term in the Lagrangian density involving this term. Therefore, any scattering amplitude involving the associated particle (fictitious photon) must be zero.

Assuming that one of the particles in the 4-gluon scattering is not a gluon but a fictitious photon one can write for the total scattering amplitude ($T^{A_4} \propto I$)

$$\begin{aligned}
0 =& \mathrm{Tr}(\mathrm{T}^{A_1} \mathrm{T}^{A_2} \mathrm{T}^{A_3}) \left[A(1, 2, 3, 4) + A(1, 2, 4, 3) + (1, 4, 2, 3) \right] \\
&+ \mathrm{Tr}(\mathrm{T}^{A_1} \mathrm{T}^{A_3} \mathrm{T}^{A_2}) \left[A(1, 3, 2, 4) + A(1, 3, 4, 2) + (1, 4, 3, 2) \right]
\end{aligned} \tag{5.28}$$

The contents of each square bracket must vanish. After the assignment of desired helicities, the first square bracket leads to the following result:

$$A(1^-, 2^+, 3^-, 4^+) = -A(1^-, 2^+, 4^+, 3^-) - A(1^-, 4^+, 2^+, 3^-) \tag{5.29}$$

From this equation the last amplitude with nonadjacent negative helicities can be calculated, since other amplitudes have the helicity pattern, which was already evaluated. The desired amplitude reads:

$$A(1^-, 2^+, 3^-, 4^+) = \frac{\langle 13 \rangle^4}{\langle 12 \rangle \langle 23 \rangle \langle 34 \rangle \langle 41 \rangle} \tag{5.30}$$

Now the amplitude for the whole process can be calculated. There are only three independent partial amplitudes, and in the present work they are chosen to be

$$A_3 \equiv A(1, 2, 3, 4) \tag{5.31}$$
$$A_4 \equiv A(1, 3, 4, 2) \tag{5.32}$$
$$A_2 \equiv A(1, 4, 2, 3) \tag{5.33}$$

Each of this amplitudes contributes to two different colour objects, since these amplitudes are invariant under reflections but the traces are not. In the next step the sum of the amplitudes can be squared and the colour sum can be carried out. Using the result from the double line notation of the previous chapter - absolute square of each trace leads to a factor of N^4 and the product of any trace times complex conjugate of any other trace yields N^2 - one finds out:

$$
\begin{aligned}
\sum_{A_1,A_2,A_3,A_4} |\mathcal{T}|^2 &= \left(2N^4 + 2N^2\right) \sum_j |A_j|^2 + 4N^2 \sum_{j\neq k} A_j^* A_k \\
&= \left(2N^4 - 2N^2\right) \sum_j |A_j|^2 + 4N^2 \left(\sum_j A_j^*\right)\left(\sum_k A_k\right),
\end{aligned}
\tag{5.34}
$$

where j and k are summed over 2,3,4. The equation derived from the decoupling of fictitious photon leads to $\sum_j A_j = 0$, and the second term in the Eq. (5.34) vanishes (the term A_3 cancels the other terms). The final result after performing the colour sum and the sum over helicity amplitudes is:

$$
\sum_{col,hel} |\mathcal{T}|^2 = g^4 N^2 (N^2 - 1) \times
$$

$$
\left(\sum_{i=1}^{3} \sum_{j=i+1}^{4} (i\cdot j)^4\right) \times \left(\sum_{perm(234)} \frac{1}{(1\cdot 2)(2\cdot 3)(3\cdot 4)(4\cdot 1)}\right),
\tag{5.35}
$$

where $(i\cdot j)$ is a four vector product of the vectors K_i and K_j. Introduction of the Mandelstam variables $s = (1+2)^2$, $t = (1+3)^2$, and $u = (1+4)^2$ (all momenta are outgoing), leads to (inserting $N=3$):

$$
\sum_{col,hel} |\mathcal{T}|^2 = 288g^4 \left(\frac{1}{s^2 t^2} + \frac{1}{s^2 u^2} + \frac{1}{t^2 u^2}\right)\left(s^4 + t^4 + u^4\right).
\tag{5.36}
$$

In this result the summation over initial and final state helicities and colours was performed. Since physical amplitudes involve averaging and not summing over the initial states, the general result Eq. (5.35) has to be divided by $4(N^2-1)^2$. There are four possible helicity configurations for the incoming gluons and $(N^1-1)^2$ possible colour configurations, since (N^2-1) is the number of gluon colours in a $SU(N)$ theory. If one performs the averaging in the QCD case, and rearranges the terms, one obtains the following result in agreement with [60]:

$$
\overline{\sum} |\mathcal{T}|^2 = g^4 \frac{9}{2}\left(3 - \frac{tu}{s^2} - \frac{su}{t^2} - \frac{st}{u^2}\right)
\tag{5.37}
$$

5.4.1 General results

After the development of the result for a process with four gluons it is important to know which statements hold also for a general case of n-gluon scattering. First of all, the symmetry properties of the partial amplitudes are true for all n-gluon processes:

$$
\begin{aligned}
A(2,\ldots,n,1) &= A(1,2,\ldots,n) \tag{5.38}\\
A(n,\ldots,2,1) &= (-1)^n A(1,2,\ldots,n) \tag{5.39}
\end{aligned}
$$

The structure of three and four gluon vertices ensures that every term in any tree-level amplitude is proportional either only to products of polarisation vectors or to both: products of polarisation vectors and products of polarisation vectors with external momenta. The factors involving momentum vectors originate in three gluon vertices. Every tree diagram with n external lines, called legs, has maximally n-2 vertices[3]. Therefore, there are maximally n-2 momenta entering the diagram, and it follows that every diagram must have at least one product of two polarisation vectors. If products of all possible pairs of polarisation vectors were equal zero, the amplitude for this process would vanish. This is the case for partial amplitudes where all gluons have the same helicity, since the gauge momentum can be chosen to be equal for all gluons, which would lead to a spinor product of two equal light-like momenta. This is also true for amplitudes where all but one gluons have the same helicity. The gauge momentum in this case has to be chosen equal to the momentum of the single negative (positive) helicity gluon. In case of a general n gluon amplitude where gluons i and j have negative helicity, while the helicity of all other gluons is positive, the amplitude takes a short analytical form [27]. Summing up, one can state the following general results:

$$A(1^{\pm}, 2^{+}, \ldots, n^{+}) = 0, \qquad (5.40)$$

$$A(1^{\pm}, 2^{-}, \ldots, n^{-}) = 0, \qquad (5.41)$$

$$A(1^{+}, \ldots, i^{-}, (i+1)^{+}, \ldots, j^{-}, \ldots, n^{+}) = \frac{\left(\sqrt{2}\right)^{n}}{2} \frac{\langle ij \rangle^{4}}{\langle 12 \rangle \langle 23 \rangle \cdots \langle n-1 n \rangle \langle n1 \rangle}. \qquad (5.42)$$

The indices products in the last equation are again products of the four vectors with the particular indices.

5.5 Multijet production and special helicity amplitudes

The QCD improved parton model allows also calculations of processes with many quarks and gluons in the final state. These processes manifest at the detector level as multijet events. In leading order QCD the cross sections for finding n jets in a defined region of phase space is calculated at the parton level from tree-level diagrams. These calculations can be done with techniques developed so far, but the number of diagrams which contribute to the processes rise, and the exact treatment of colour structure becomes more complicated. The general expression for the cross section of an n jet final state reads:

$$\sigma^{n} = \sum_{i,j,k_1,\ldots,k_n=q,\bar{q},g} \int_0^1 dx_1 dx_2 \, f_i(x_1, \mu^2) f_j(x_2, \mu^2) \hat{\sigma}^{ij \to k_1,\ldots,k_n} \qquad (5.43)$$

The leading order matrix elements for all the $2 \to 3, 4, 5, \ldots, 18$ processes are known [61]. The cross sections fall roughly geometrically with increasing n, because of the dependence on α_s^n.

---

[3]To maximise the number of vertices while holding the number of legs minimal one chooses three gluon vertices as building blocks of the diagram. Each vertex has three legs, and if there are m vertices one can arrange them in a way, that $m-2$ vertices have only one external leg, the other two legs are connecting them with other vertices. Two vertices are the last ones in the chain and have 2 external legs each. Adding the number of legs one gets m-2+4 = m+2.

Parallel to performing exact calculations, efforts have been made to approximate the matrix elements for any given n. Several approximation schemes were developed and this work uses the first part of the SPecial HELicity (SPHEL) approximation proposed in [27]. The term special helicity refers to the processes where all but two partons have the same helicity when all the momenta are outgoing, since short analytical expressions for $K_F(P)$ exist for this helicity configurations. The precise expression of the approximation depends on the number of quarks present in the n-particle scattering process. The full SPHEL approximation includes terms for zero, one and two massless quark pairs. Since only the first term of the approximation (pure gluonic case) will be of importance for this work, it is only this part, that will be presented here. It was proposed originally by Kunszt and Stirling [62] and was incorporated later in the more general SPHEL approximation.

SPHEL contains two assumptions. The first one is that the special helicity configurations are typical for all possible configurations. The second assumption is that the non leading order colour contribution can be neglected. Reduction of the colour contribution to the leading order ensures factorisation of the matrix elements into the colour and the dynamical part, which become independent. Furthermore, there is no interference between the $K_F(P)$. The dynamical part for the gluonic special helicity configurations has been presented in the previous section cf. Eq. (5.40).

The SPHEL approximated square of the matrix element reads:

$$
\sum_{col,hel} \left| \mathcal{T}_k^l(q_1\bar{q}_1; \cdots ; q_l\bar{q}_l; g_1 \cdots g_k) \right|^2 =
$$
$$
a_k^l S_k^l C_k^l(N) K_k^l(q_1\bar{q}_1; \cdots ; q_l\bar{q}_l; g_1 \cdots g_k),
$$
(5.44)

where l is the number of quark pairs, k the number of gluons, K_k^l is the function, which entails the dynamic of the process, a_k^l is a free tuning factor, $C_k^l(N)$ is the leading order colour factor, and S_k^l is a combinatorial factor to account for the uncalculated helicity amplitudes.

The $l = 0$ part of SPHEL uses the property that the subamplitudes are zero when less than two gluons have a helicity opposite to the helicity of the other gluons. For $k \leq 5$ SPHEL coincides with the exact result. The different contributions to the square of the matrix element (factors of g^n are left out and have to be taken later into account):

$$
K_k^0 = 2 \sum_{1 \leq i \leq j \leq k} (i \cdot j)^4 \sum_{perm(2...k)} \frac{1}{(1 \cdot 2)(2 \cdot 3) \cdots (k \cdot 1)}
$$
(5.45)

$$
S_k^0 = \frac{\text{Number of non-zero amplitudes}}{\text{Number of SPHEL amplitudes}} = \frac{2^k - 2(k + 1)}{k(k - 1)}
$$
(5.46)

$$
C_k^0 = 4(N/2)^{k-2}(N^2 - 1)
$$
(5.47)

The errors introduced by the approximation depend on the process under consideration. The negligence of non leading order colour contribution does not affect much the gluonic sub-processes, for example for $k = 6$ it is about 1%. However it can amount up to 10% for processes involving one quark pair. Although these errors

change the absolute numbers, they do not modify the shapes of the distributions [27]. The last statement is also true for the first assumption[4], whose impact on the total cross section is even worse . The gluonic SPHEL part overestimates the exact gluonic cross section at the Tevatron Run I collider energy ($\sqrt{s} = 1.8\ TeV$), for instance by a factor of 1.4 for $k = 7$. A tuning factor a_k^0 was introduced to correct this overestimation. This factor depends however on the collider energy and on the phase space cuts, which leads to the conclusion that SPHEL is not able to give precise results for the total cross section without tuning. The main feature of SPHEL is the correct estimation of the shapes of various distributions [27]. This feature inspired the construction of event shape variables based on the gluonic part of the SPHEL. These variables will be introduced in the following chapter.

---

[4]The special helicity configurations are typical for all possible configurations.

6

Antenna Variables

The search for physics beyond the standard model is one of the main goals of the CMS detector, as already stated in chapter 3. Although the LHC will be able to access the desired domain, where, according to the theoretical predictions, new phenomena should appear, the path to discoveries will not be straightforward, due to the dominance of standard model processes, in particular QCD. For example, the cross section to produce a jet with a transverse energy larger than 100 GeV is greater than 1 μb, as it can be seen in Fig. 6.1, in contrast to the total production cross section for the SUSY LM1 point, which amounts to ca. 55 pb, see chapter 2. Depending on the characteristics of the signal, different techniques have been developed to suppress various standard model backgrounds.

The approach presented in this work intends to describe QCD multijet events, which are one of the main backgrounds in searches for new signals in the all-hadronic channel, by utilising the theoretical knowledge about the structure of QCD matrix elements. In the present work SUSY based on the mSUGRA model with R-parity conservation was chosen as an example for a possible signal (cf. chapter 2). As it was shown in the previous chapter, scattering amplitudes for multiparton production can be approximated by a sum over terms with a particular pole structure in the phase space, see chapter 5.5. Such terms are called QCD-*antenna* [25, 63], and since they lie at the core of the present approach, the variables constructed in this work are called antenna variables. The main goal of the present work is the investigation of these variables. The variables should be sensitive to the differences between event structures of QCD multijet production originating mostly in the gluon radiation, and the decays of heavy particles (e.g. SUSY), which can also lead to many jets in the final state.

This chapter describes first the software and datasets which were used for the studies. Then different antenna variables are introduced, and it is shown how they are implemented numerically. In the next step "proof of principle" results at the parton level for the process $gg \rightarrow gg$ are presented. They are followed by results for the variables at the hadron jets level (without detector simulation). Next the transition to the jets constructed from simulated energy deposition in the calorimeter cells of the CMS detector is undertaken. All results are summarised in plots, before in the
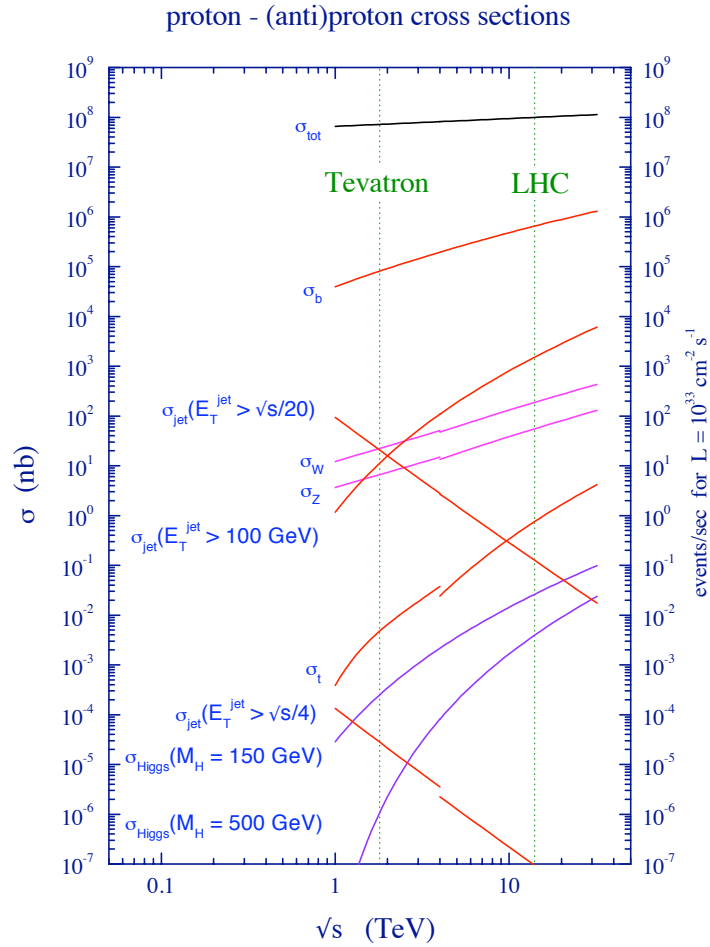
Figure 6.1: Standard model cross sections at the Tevatron and LHC colliders [64].

last step correlations between the antenna and event shape variables (sphericity and thrust) are investigated.

6.1 Datasets

The studies of this work were performed using the 1.6.12. version of the software framework of the CMS experiment (CMSSW 1.6.12). The various variables are implemented as the so called "selector modules" in the framework of the physics analysis toolkit (PAT) for SUSY searches [65].

The QCD datasets are part of the official CMS CSA07[1] production [66]. The whole produced data contains more than 150 million simulated standard model events, and represents the first 100 pb^{-1} of LHC data. For technical reasons the data is separated in three "soups". The "gumbo" soup contains mainly QCD and Photon+Jet events, and is of interest for the present work. All events of this soup are generated with the Pythia event generator [67]. The SUSY group distilled a sub-sample from the

---

[1]Computing Software and Analysis challenge

SUSY Point	Number of events MC	σ [pb]	weight
LM1	120624	54.86	0.45
LM4	93751	25.11	0.261
LM8	83708	12.19	0.146
HM3	12133	0.047	0.0038

Table 6.1: Number of simulated events for each SUSY Point, as well as corresponding cross section in pb and weighting factor for the integrated luminosity of 1 fb^{-1}.

"gumbo" soup, which consists of potential background events for the SUSY searches in the all-hadronic channel and is characterised by the following cuts: each event contains at least one jet with $E_t > 80~GeV$ and one jet with $E_t > 20~GeV$. The events should furthermore pass one of the High-Level-Triggers based on the missing transverse energy and number of jets [66]. This sub sample[2] containing 5603793 events was selected for the present study. Since the selection of the events is based on the triggers, the events represent a realistic scenario for the LHC data taking. The simulation was affected by a bug [68]: The momenta of some jets originating from decays of either long lived b-, and c-hadrons or of τ-leptons are given in the reference frame of the mother particle, and not in the laboratory frame. As a result such events have wrong values for $E_t = E \sin \theta$ of the jets and for missing transverse energy, since almost the entire energy of the b-hadron is lost. These events are not used for the present analysis. This affects 1-2% of all QCD events.

The SUSY datasets for the points LM4, LM8, and HM3 were simulated with Pythia 6.409 in a private Monte Carlo production [69]. The events were simulated and reconstructed with the full CMS detector simulation using CMSSW software versions 1.6.5 - 1.6.7 [69].

The dataset for the SUSY LM1 point is a part of the official CSA07 production. It was produced and reconstructed with the CMSSW version 1.4.X, where $X > 3$ [70]. In the present study all events are weighted to represent an integrated luminosity of 1 fb^{-1}. Table 6.1 summarises the information on SUSY datasets used in the present work.

6.2   Definition of the variables

The theoretical machinery developed in the last chapters leads to an approximation for cross sections of multijet processes. Although the approximation overestimates the total cross section, the shapes of different distributions are in agreement with exact results [27]. Instead of using this approximation for predictions of cross sections, this work employs it as a basis for the construction of observables from the momenta of jets measured in the detector. All jets are reconstructed with the k_t algorithm introduced in section 5.2, the user chosen scaling factor R is set to 0.4.

Before the definition of the variables, further approximations have to be made:

- All differences between pure gluonic and gluon-quarks events are ignored, so that jets measured in the detector are treated as gluon jets. This crude approximation can be justified, since gluons are the dominating initial states at

---

[2]HLT JetMET Skim:
/CSA07JetMET/CMSSW_1_6_7CSA07GumboB1PDJetMET_Skims1susyJetMET/USER

the LHC for low partonic centre of mass energies (the majority of the dijet production for the transverse momentum range less than $1\ TeV$ will be with gg initial state [71]) and gluon quark initial states are dominating a wide kinematic range, c.f Fig. 6.2 showing the fractional contribution of the various partonic processes to the total jet cross section. This quantitative result is anticipated from the form of the partonic pdfs, c.f Fig. 5.2. Furthermore, processes with gluons are more important, because of the larger colour charge of the gluons[3][25]. As example, Kuijf ([27]) compared expected LHC leading order cross sections ($\sqrt{s} = 16\ TeV$ in his thesis) with various initial and final states for four and five jet events (He considered partons with $p_t > 60\ GeV$, $\eta < 2.0$, and with the angle between two partons larger than $40°$). He found out, that pure gluon scattering is responsible for 53 % of the total four jet cross section and 49 % of the total five jet cross section respectively. The next most important processes were those including one quark pair, they amounted to 38% of the total crossection for the four jet, and 37% for the five jet case. Similiar reason for the importance of the processes involving gluons in the final state is the difference between Sudakov form factors for the splitting $g \rightarrow gg$ in comparison with $q \rightarrow qg$. The Sudakov form factors give the probability for a parton to evolve from a hard to a soft scale without emitting a parton and are used in parton showering approaches of Monte Carlo event generators. The probability to radiate a gluon is larger for the gluon initial state, because of its larger colour factor [71].

- Antenna structures involve not only momenta of the outgoing but also the momenta of incoming partons. In the present approach momenta of incoming partons are approximated using energy conservation by summing over the jets in the final state assuming, that the momenta of these partons have vanishing transverse components. The terms are generalisations of the results from the section 5.3:

$$k_1 \;=\; \frac{\sqrt{s}}{2}(x_1, 0, 0, x_1), \quad \text{with} \quad x_1 = \frac{1}{\sqrt{s}}\sum_i m_i^T (e^{y_i}) \qquad (6.1)$$

$$k_2 \;=\; \frac{\sqrt{s}}{2}(x_2, 0, 0, -x_2) \quad \text{with} \quad x_2 = \frac{1}{\sqrt{s}}\sum_i m_i^T (e^{-y_i}) \qquad (6.2)$$

$m_i^T = \sqrt{m_i^2 + p_i^{T2}}$ being the transverse mass of a jet i and y_i is the rapidity of jet i. The sum runs over all jets.

Antenna variables are constructed from all well defined jets (c.f. 6.4) present in the event and the approximated momenta of incoming partons. The straightforward

---

[3]Only gluons introduce representation matrices into the amplitudes, which leads to larger factors via evaluation of traces. Colour charge is often quantified as the value of the quadratic Casimir operator of the particular representation of the $SU(3)$ group. The quadratic Casimir operator of the fundamental representation is 4/3, while it has the value 3 for the adjoint representation.
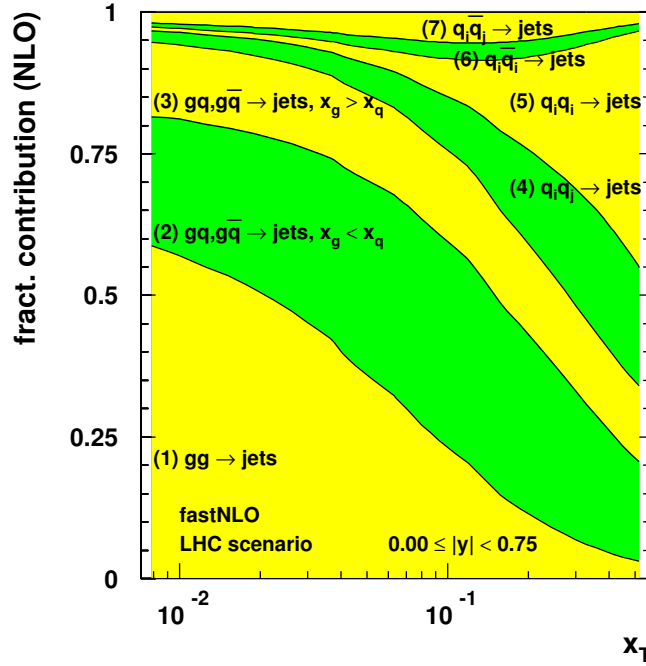
Figure 6.2: Decomposition of the total jet cross section into the partonic processes at the LHC. The fractional contributions are shown versus the scaling variable $x_t = 2p_t/\sqrt{s}$ [4].

definition of the antenna *NJet** variable A_{n*} follows closely the gluonic SPHEL formula and utilises all jets in the event:

$$A_{n*} = \frac{2^k - 2(k+1)}{k(k-1)} \cdot (3/2)^{k-2} \cdot (64) \times$$
$$\sum_{1 \le i \le j \le k} (i^m \cdot j^m)^4 \sum_{P(2...n)} \frac{1}{(1^m \cdot 2^m)(2^m \cdot 3^m)\dots(k^m \cdot 1^m)} \times GeV^{2*(n-2)}, \quad (6.3)$$

with n number of jets in the event, and $k = n + 2$ number of momenta in the event (jets and approximated incoming partons). The momenta are written in the $p_i \equiv i$ notation. The index m indicates that these are measured or approximated momenta. Regarding a multijet event, and assuming this event was produced by a QCD process, the value of this variable can be interpreted as a crude guess for the value of the partonic matrix element (a factor of g^n has to be taken into account) of this particular event in the gluonic SPHEL approximation. However, this interpretation is only valid for QCD, not for SUSY.

A better interpretation, which can be also extended to the subsequent variables, is the treatment of this variable as an *average inverse invariant mass* of jet pairs of the event [72]. The definition of the variable suggests this interpretation, since events with many adjacent jets lead to larger values of the variable[4] — many of the four products in the denominator tend to be small— than events with large invariant

---

[4]In the subsequent sections the variables will be multiplied with (-1) and to be consistent with the plots the values of the negative antenna variables will be discussed. Consequently the sentence will be changed to: events with many adjacent jets lead to **smaller** values of the variable.

masses originating from decays of heavy particles. In summary, the variable is sensitive to the invariant masses present in the event. Hence most QCD events, which are characterised by gluon emissions, should lead to a larger value of the variable than SUSY events, in which many large invariant masses are present.

The variable defined so far has a drawback, since it partitions the data in bins of number of jets. Each such "NJet" bin will have in general varying statistics. Additionally, there can be a lot of migration of the events between the bins, since the boundaries depend on the thresholds of the jets and jet definitions, which complicates the comparability of the studies. The situation is getting even more complicated using jets reconstructed from calorimeter cells compared to jets on generator level. In order to use a variable of this kind as an additional discriminator in existent studies, which require a minimum number of jets and no maximum number, new variables using a defined number of leading jets can be constructed.

The simplest example is the antenna $3Jet$ variable A_3, which uses only the first three leading jets of each event:

$$A_3 = 216 \times \sum_{1 \leq i \leq j \leq 5} (i^m \cdot j^m)^4 \sum_{P(2...5)} \frac{1}{(1^m \cdot 2^m)(2^m \cdot 3^m) \ldots (5^m \cdot 1^m)} \times GeV^2. \quad (6.4)$$

Requiring three jets one rejects QCD dominated dijet events and makes this variable compatible with the proposed SUSY search in multijet events ($N_{jet} \geq 3$) with large missing transverse energy [4]. A possible drawback of this variable is the utilisation of only three jets, which might not be enough to describe properly the different event structures of QCD and SUSY.

In order to incorporate more of the event information in the variable, a antenna $3plus$ variable A_{3plus} is defined. This variable uses the vector sum of all jets in the event, besides the two leading jets, as the third jet:

$$A_{3plus} = 216 \times \sum_{1 \leq i \leq j \leq 5} (i^m \cdot j^m)^4 \sum_{P(2...5)} \frac{1}{(1^m \cdot 2^m)(2^m \cdot 3^m) \ldots (5^m \cdot 1^m)} \times GeV^2, \quad (6.5)$$

with $5^m \equiv p_5^m = \sum_{i=3}^{n} p_i^m$, n being the number of jets in the event.

Finally, a antenna $6jet$ variable A_6 is defined by requiring events with at least six jets, which are then used to calculate the value of the variable. This variable is a compromise, because it incorporates more of the event structure than the variables using three jets but does not partition the data in many bins like the A_{n*}. Provided that this variable has the desired discrimination power, it could be used in further studies, which would in that case require at least six jets. The variable is given by:

$$A_6 = \frac{12393}{4} \times \sum_{1 \leq i \leq j \leq 8} (i^m \cdot j^m)^4 \sum_{P(2...8)} \frac{1}{(1^m \cdot 2^m)(2^m \cdot 3^m) \ldots (8^m \cdot 1^m)} \times GeV^8. \quad (6.6)$$

The choice of the six leading jets will be motivated in subsequent sections, where the distributions of the variables for QCD and SUSY (LM4) data samples are shown.

6.2.1 Numerical implementation

The permutation sum occuring in the definitions of all variables is evaluated using the technique proposed by Kuijf in [27]. To exemplify the problem, a general expression P is defined:

$$P = \sum_{P(1...n)} f(L, 1, \ldots, n, R), \quad (6.7)$$

with

$$f(L, 1, \ldots, n, R) = \frac{1}{(L \cdot 1)(1 \cdot 2) \cdots (n \cdot R)}, \tag{6.8}$$

where L and R are arbitrary momenta. Naive evaluation would lead to generation and storage of all permutations of indices $1 \ldots n$, k and multiplication of $n + 1$ momenta for each function f. Many of these functions are however closely interconnected, since many of the included momenta products are identical. This can be seen if one compares two functions f differing only by two indices which were *swapped* - two neighbour indices were interchanged. The ratio of such two functions f is:

$$\frac{f(L, 1, \ldots, a, b, c, d, \ldots, n, R)}{f(L, 1, \ldots, a, c, b, d, \ldots, n, R)} = \frac{(a \cdot c)(b \cdot d)}{(a \cdot b)(c \cdot d)}. \tag{6.9}$$

It follows, that if all permutations are ordered in a way that two successive permutations differ only by a swap, it is sufficient to calculate the function f only one time. All other possible values of the function can be then obtained using the Eq. 6.9. The permutations are generated based on this requirement (all successive permutations differ only by a swap) with the following algorithm:

- The first sequence of indices is $(1, 2, \ldots, n)$. Every index has its own swap direction, which is initialised with the left neighbour. The subsequent step is applied recursively, and the recursion begins with the index $i = n$ and stops when an attempt is made to swap with $i = 1$.

- The index i is swapped one time unless

  a) there are no indices in the swap direction or

  b) the index to change places with is higher

  If the swap was not successful, the swap direction of index i is reversed and recursion is applied to index $i - 1$. If the swap was successful, the step is continued with index n.

This algorithm allows efficient evaluation of the products and permutations sums [27], and is used in the present study.

6.3   Proof of principle

The goal of this section is the cross check of the implementation of the variable and an analysis of its meaning. For this reason the A_{n*} variable is computed from the two leading final state partons of the QCD dataset. Only $gg \to gg$ events are selected. Furthermore, the invariant mass of the two leading partons was chosen to lie in the region between 300 and 600 GeV. Since the A_{n*} variable is constructed out of the two final state gluons, it is called the A_{2*} variable. The momenta of the incoming partons were computed with the approximation presented in the last section. The value of the A_{2*} variable is, in the case of negligible initial- and final-state radiation, the exact result for $\frac{\mathcal{I}}{g^4}$ if it is averaged over the colours and helicities of the initial states. This averaging is necessary, since the variable incorporates only summations over the properties of the initial and final states. The formula computes exact tree-level cross section only for processes without gluon-showers, but the gluon

showers are present in the simulated events used in the present work. For this reason, only normalised distributions are shown and only the shapes of the distributions are compared. The differential cross section for a jet pair of mass M_{JJ} produced at an angle θ to the beam direction in the parton-parton centre of mass frame reads (c.f. Eq. 5.13):

$$\frac{d^2\sigma}{dM_{JJ}^2 dz}\frac{1}{g^4} =$$
$$\int_0^1 dx_1\,dx_2\,f_g(x_1,\mu^2)f_g(x_2,\mu^2)\delta(x_1 x_2 s - M_{JJ}^2)\frac{1}{64\pi M_{jj}^2}\frac{1}{256}\underbrace{\frac{(288\cdot(3+z^2)^3)}{(z^2-1)^2}}_{A_{2*}(z)},$$

$$(6.10)$$

where $z \equiv \cos\theta$, since $d\cos\theta = dz$, and the gluon scattering formula from Eq. 5.36 was inserted. The Mandelstam variables of the original formula are expressed here in dependence of $\cos\theta$. As the first step, the integration over x_1 eliminates the delta function and leads to the Heaviside theta function Θ:

$$\frac{d^2\sigma}{dM_{JJ}^2 dz}\frac{1}{g^4} =$$
$$\int_0^1 dx_2\,f_g(\frac{M_{JJ}^2}{s^2 x_2},\mu^2)f_g(x_2,\mu^2)\Theta(s^2 x_2 - M_{JJ}^2)\frac{1}{64\pi M_{jj}^2}\frac{1}{256}\frac{(288\cdot(3+z^2)^3)}{(z^2-1)^2}.$$

$$(6.11)$$

The integration over the theta function is equivalent to the shift in the lower integral limit $0 \to M_{jj}^2/s^2$. Hence, the cross section can be written as:

$$\frac{d^2\sigma}{dM_{JJ}^2 dz}\frac{1}{g^4} =$$
$$\int_{M_{jj}^2/s^2}^1 dx_2\,f_g(\frac{M_{JJ}^2}{s^2 x_2},\mu^2)f_g(x_2,\mu^2)\frac{1}{64\pi M_{jj}^2}\frac{1}{256}\frac{(288\cdot(3+z^2)^3)}{(z^2-1)^2}.$$

$$(6.12)$$

The occurring integral can be evaluated numerically. For the computations in this chapter the CTEQ 5.1 pdfs [73] were used. The scale μ^2 was set to 100 GeV^2.

Integration over M_{jj}^2 from 9000 to 360000 GeV^2 leads to the differential cross section in dependence from $\cos\theta$:

$$\frac{d\sigma}{dz}\frac{1}{g^4} = c\frac{(288\cdot(3+z^2)^3)}{(z^2-1)^2} = c \cdot A_{2*}(\cos\theta \equiv z) * \frac{1}{GeV^2},$$

$$(6.13)$$

c being the numerical prefactor originating from the integration (0.0651). The integration was performed using a numerical integration routine [74]. The last computation shows that the shape of the differential cross section in dependence of $\cos\theta$ is independent from the parton distribution functions. In order to test the theoretical prediction, the cosine of the scattering angle in the centre of mass frame $\cos\theta$ can be computed from the rapidities of the two leading partons, as shown in section 5.3. Figure 6.3 shows the normalised distribution of $\cos\theta$ computed from data, as well as the fit of the theoretical function. The number of events rises with the modulus of the $\cos\theta$, as predicted by the theory. The distribution shows a cut off at large cosine values where the theoretical function becomes divergent and the Monte Carlo
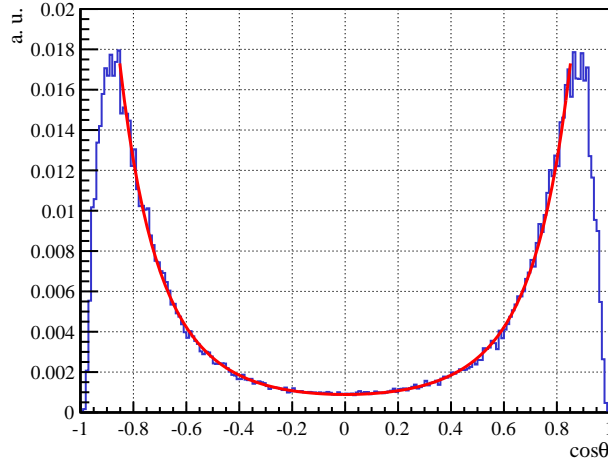
Figure 6.3: Normalised (area=1) distribution of $cos\theta$ computed from the rapidities of the two leading partons in each event (blue curve). The red curve is the fit of the theoretic formula to the data.

events are not produced. Furthermore, effects of final state radiation have to be taken into account, since the additional gluons in the final state lead to a disbalance of the transverse momenta and rapidities of the two leading gluons. Therefore, the formula for $\cos\theta$ is only an approximation. The effect described above is also responsible for the minor asymmetry of the distribution. The red curve shows the fit of the function $(288 \cdot (3 + z^2)^3)/(z^2 - 1)^2$ to the data. The curve matches the data, as long as the fitting range excludes the cut-off regions.
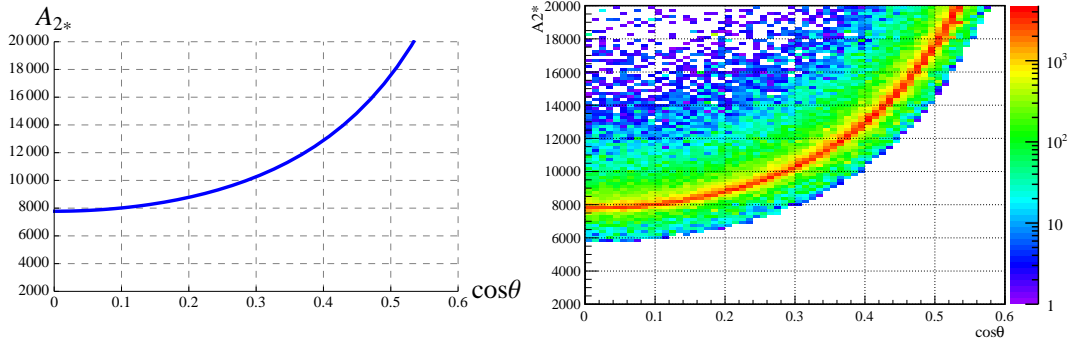
Figure 6.4: **Left:** Theoretical prediction for the dependence of the A_{2*} variable on $\cos\theta$. **Right:** Distribution of the A_{2*} variable plotted vs. the distribution of $\cos\theta$ computed from data. Colour code indicates the number of events in each bin. Both plots are shown for $\cos\theta$ range of 0 - 0.6.

The crucial check of the implementation and understanding of the variable is the comparison between the theoretical curve for the dependence of the variable on $\cos\theta$ and the correlation between the values of $\cos\theta$ and A_{2*} computed in each event. The theoretical formula is polynomial in $z \equiv \cos\theta$:

$$A_{2*} = \frac{(288 \cdot (3 + z^2)^3)}{(z^2 - 1)^2}. \tag{6.14}$$
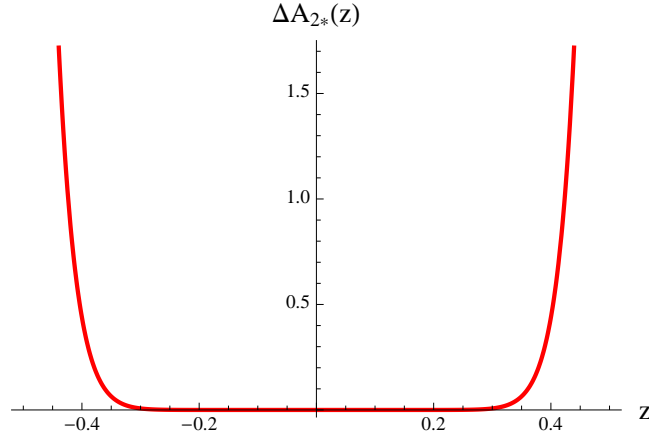
Figure 6.5: Difference between the exact function $A_{2*}(z)$ and the power series approximation.

Figure 6.4 shows both plots for the range of $\cos\theta$ between 0 and 0.6. These values were chosen for better comparison, since the curves have a too large slope for larger $\cos\theta$. The correlation plot shows exactly the predicted dependence between both variables. The theoretical curve intersects the y-axis at the value of 7776, which corresponds to the value of the partonic matrix element for gluon scattering at the angle of 90° (The value has to be averaged over initial states and hence divided by 256, which leads to 30.8 - the exact value from [25]). Most events - represented by red bins - follow the theoretical curve and have the predicted value of A_{2*} if their $\cos\theta$ value equals 0. The events in which the variables do not have the exactly predicted correlation are stronger affected by the final and initial state radiation and hence cannot be treated as pure four gluon events.

As the last step, the distribution of the A_{2*} variable in the data should be understood. In order to get a theoretical prediction for this distribution, the differential cross section, which is a function of $\cos\theta$ has to be transformed to a differential cross section in dependence of A_{2*}:

$$dz = \left|\frac{dz}{dA_{2*}}\right| dA_{2*} \Rightarrow \frac{d\sigma}{dA_{2*}}\frac{1}{g^4} = cA_{2*} \cdot \left|\frac{dz}{dA_{2*}}\right|. \tag{6.15}$$

To get a qualitative feeling for the form of $d\sigma/dA_{2*}$, A_{2*} can be expanded as a power series (in this example up to 13'th order):

$$
\begin{aligned}
A_{2*}(z) =& \frac{(288 \cdot (3 + z^2)^3)}{(z^2 - 1)^2} = 7776 + 23328z^2 + 41472z^4 \\
& + 59904z^6 + 78336z^8 + 96768z^{10} + 115200z^{12} + o[z^{14}]
\end{aligned}
\tag{6.16}
$$

Figure 6.5 shows the difference between the exact formula and the approximative power series as a function of z. The series is in good agreement with the true function up to $z = 0.4$. In the next step the power series can be inverted. The inverse function is an approximation for the function $z(A_{2*})$, precise within few percent up to such values of A_{2*} ($A_{2*} \approx 13000$) where z reaches the value of 0.4. Figure 6.6 shows the inverse function. Finally the expression for a function f, which
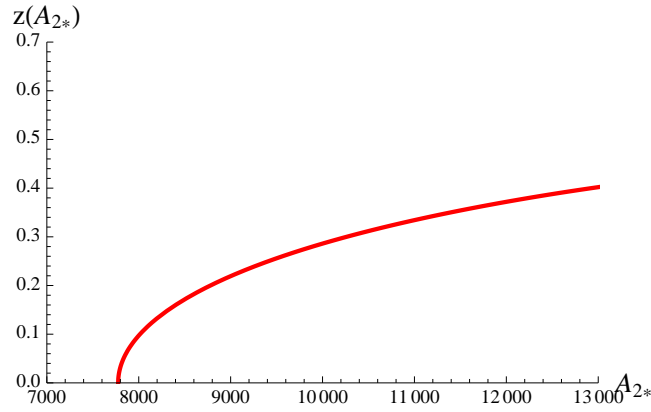
Figure 6.6: The function $z(A_{2*})$ approximated as a power series, shown in the trustable domain of definition.

should be proportional to $d\sigma/dA_{2*}$ can be plotted. The shape of this function should resemble the shape of the A_{2*} distribution in data. The function f reads:

$$f = A_{2*} \cdot \left| \frac{dz}{dA_{2*}} \right|, \tag{6.17}$$

where $z(A_{2*})$ is the function defined above as a power series. Figure 6.7 shows on the left hand side the function f and on the right hand side the normalised distribution of the variable A_{2*} computed from data.
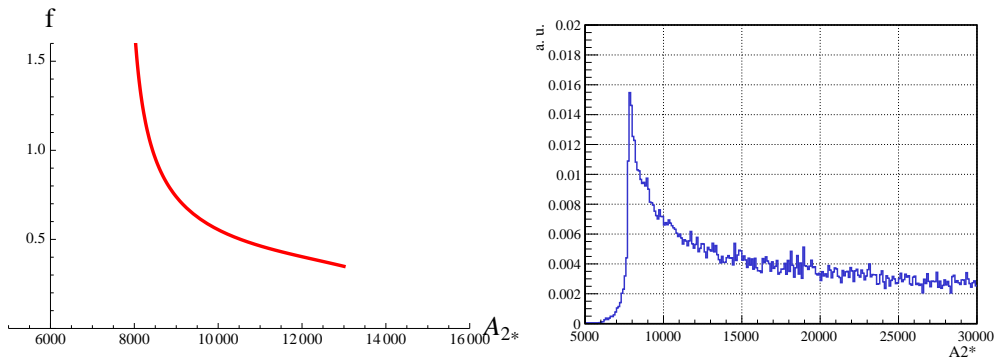
Figure 6.7: **Left:** The function f, defined in the text. **Right:** Distribution of the A_{2*} variable, calculated from data. The shape of the function f should resemble the shape of the true A_{2*} distribution.

Both curves show similar behaviour. The theoretical curve diverges for $A_{2*} \to 7776$, what can be also found in the measured distribution. The divergence of f results from the extreme steep fall of the inverse function $z(A_{2*})$ for $A_{2*} \to 7776$, see Fig. 6.6, causing the derivative to blow up. The number of events in the measured distribution rises until the cut-off, since 7776 is the theoretical minimum value for the matrix element. Some events have values of A_{2*} smaller than 7776, which resembles the situation in Fig. 6.4, and can be explained in the same way by initial and final state radiation. The function f is plotted in the trustable domain of definition and resembles well the shape of the measured distribution, which continues to fall slowly
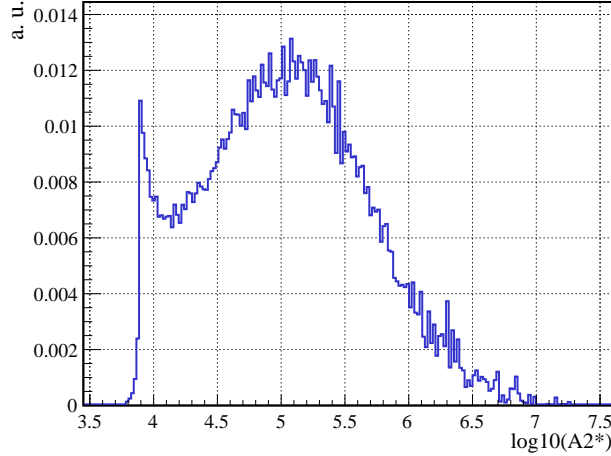
Figure 6.8: Distribution of the logarithm of A_{2*} to base 10.

over a wide range of A_{2*}, until it fades out for extreme large values, which correspond to $\cos\theta \to \pm 1$. This behaviour can be understood from the steep form of $A_{2*}(z)$ for large z, which leads to the fact, that large variations of the A_{2*} values correspond to minor changes in $z \equiv \cos\theta$.

A convenient representation of the variables for many purposes is a plot of their logarithm to base 10. All subsequent distributions of the antenna variables will use this representation. Therefore, it is convenient to redefine the variables:

$$A_n := \log_{10}(A'_n), \tag{6.18}$$

where A'_n are previous definitions of the antenna variables. Figure 6.8 shows such plot for the A_{2*} variable. In order to understand the shape of such plots, it is important to consider that the number of possible values of A_{2*} grows from bin to bin, since the plot is showing a logarithmic quantity. Hence, a uniform distributed quantity would lead in such a plot to an ever growing curve. The distribution of the A_{2*} variable has some distinctive features: the peak at $\log_{10}(A_{2*}) = 3.9$ corresponds to the true peak of the A_{2*} distribution at 7776. The steep fall of the A_{2*} distribution is also carried over to the logarithmic plot. After the steep fall, the A_{2*} variable undergoes a slow decrease, which transforms into a rise of the $\log_{10}(A_{2*})$. The fall of the $\log_{10}(A_{2*})$ distribution for values larger than 5 can be understood from Fig. 6.9 which shows the correlation between $\cos\theta$ and the logarithm of A_{2*} to base 10, plotted over the whole domain of $\cos\theta$ contrary to Fig. 6.4. The number of events being affected by the initial and final state radiation falls rapidly after $\log_{10}(A_{2*}) = 5$. Additionally the cut off at large cosine values starts between $\log_{10}(A_{2*}) = 5.5$ and $\log_{10}(A_{2*}) = 6$, as it can be inferred from the colour code. These effects force the $\log_{10}(A_{2*})$ distribution in Fig. 6.8 to decrease.

In summary, the antenna A_{2*} variable shows the expected behaviour. The values of the variable computed from the momenta of two leading partons in each event are in agreement with theoretical predictions, and the shapes of all distributions can be explained by theoretical calculations. The correlation between the A_{2*} variable and $\cos\theta$ shows the desired pattern. The algorithm for the computation of the antenna
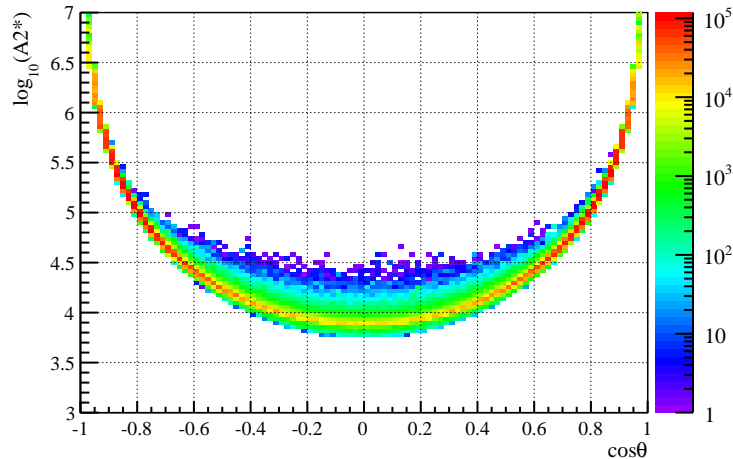
Figure 6.9: Correlation between the $\log_{10}(A_{2*})$ variable and $\cos\theta$. Colour code indicates the number of events in each bin.

variables implemented in the present work delivers correct values for the A_{2*} variable and can be trusted.

6.4   Results on hadron-jets level

In this section antenna variables computed from jets reconstructed with the k_t algorithm out of hadrons from Monte Carlo data, q.v. section 6.1, the so called GenJets, are studied. The distributions of the variables constructed from QCD multijet events will be compared with the distributions of the antenna variables constructed from SUSY events out of two SUSY scenarios differing in underlying theoretical parameters[5]. Since the number of QCD events exceeds the number of SUSY events all subsequent plots will show distributions of the antenna variables normalised to unit area. Considering different event structures of QCD and SUSY, the distributions are expected to be displaced with distribution of the antenna variables computed from QCD events tending to larger values, due to more closely radiated gluons (small opening angle θ between the partons) and hence larger inverse invariant mass. However, the discrimination power should vary with the different SUSY scenarios under consideration. The discrimination power is expected to decrease if the chosen theoretical parameters lead to decreasing mass of decaying SUSY particles, since this would make SUSY events more QCD-like because of smaller averaged invariant masses and higher boosted primary particles leading to more collimated jets. Additionally, boosted jets originating from soft gluons radiated by the final state quarks can overcome the thresholds and enter the calculation. Such jets would enlarge the value of the variable. The results of this and the following section are summarised in plots in section 6.7.

The SUSY scenarios used for the comparison are the CMS test points LM1 and LM4, whose underlying theoretical parameters are given in chapter 2. Important for the present work are the key values for gluinos and squark masses, which are

---

[5]Different test points in the mSUGRA m_0-$m_{1/2}$ plane.

Point	$M(\tilde{q})$	$M(\tilde{g})$	σ
LM1	558.61	611.32	54.86
LM4	660.54	695.05	25.11

Table 6.2: Masses of squarks and gluinos in GeV and cross sections in pb (at NLO) for LM1 and LM4 test points.

given along with the cross section (NLO) in Tab. 6.2 [4]. Considering the arguments above, antenna variables are expected to have greater discrimination power between QCD- and SUSY LM4-events in comparison with their discrimination power between QCD- and SUSY LM1-events.

The jets entering the computation have to fulfil certain requirements. In the first step only events passing the direct lepton veto on the detector level were selected. The direct lepton veto rejects all events, in which isolated electrons or muons were found. Since characteristics of the variables are demonstrated on the SUSY samples, certain cuts from the all-hadronic SUSY search were adopted. Only events with at least 3 jets are considered. This cut is part of the signal selection for events with many jets in the final state. The following selection criteria were applied to *all* GenJets:

- $p_t > 20\ GeV$,

- $|\eta| < 3.0$.

These cuts ensure that only jets with well measured energies in the hadron calorimeter barrel and endcaps would be selected on the detector level [4, 5, 69]. Additional restrictions were imposed on the *two leading GenJets*:

- $p_t^{j(1)} > 200\ GeV$,

- $p_t^{j(2)} > 150\ GeV$,

- $\left|\eta^{j(1)}\right| < 1.5$.

The restrictions on the transverse momenta of the leading jets will be replaced by cuts on the transverse energy on the calorimeter level. These cuts were selected to optimise the ratio of signal- to background-events. The cut on the pseudorapidity of the leading jet ensures that its track is in the inner tracker and was adopted to be compatible with previous SUSY searches [4, 5, 69].

Figure 6.10 shows distributions of the GenJet multiplicities in the QCD and SUSY LM4 sample. Only GenJets that pass all selection criteria are shown. The upper limit is set to eight jets, since only events with maximal eight selected jets enter exact antenna computation in order to speed up the event processing. The upper plot of Fig. 6.10 shows that for QCD the number of events falls rapidly with increasing number of jets. The lower plot of Fig. 6.10 reveals the different multiplicity distribution in the SUSY LM4 case, as expected. SUSY events tend to have a larger number of high energetic jets originating from cascade decays of supersymmetric particles, contrary to the gluon radiation pattern of QCD. Most SUSY LM4 events contain

Entries	2752057
Mean	4.141 ± 0.002259
RMS	1.206 ± 0.001597
Integral	$2.248e+07$

Entries	30773
Mean	5.527 ± 0.008832
RMS	1.549 ± 0.006245
Integral	8031

Entries	30773
Mean	5.527 ± 0.008832
RMS	1.549 ± 0.006245
Integral	8031
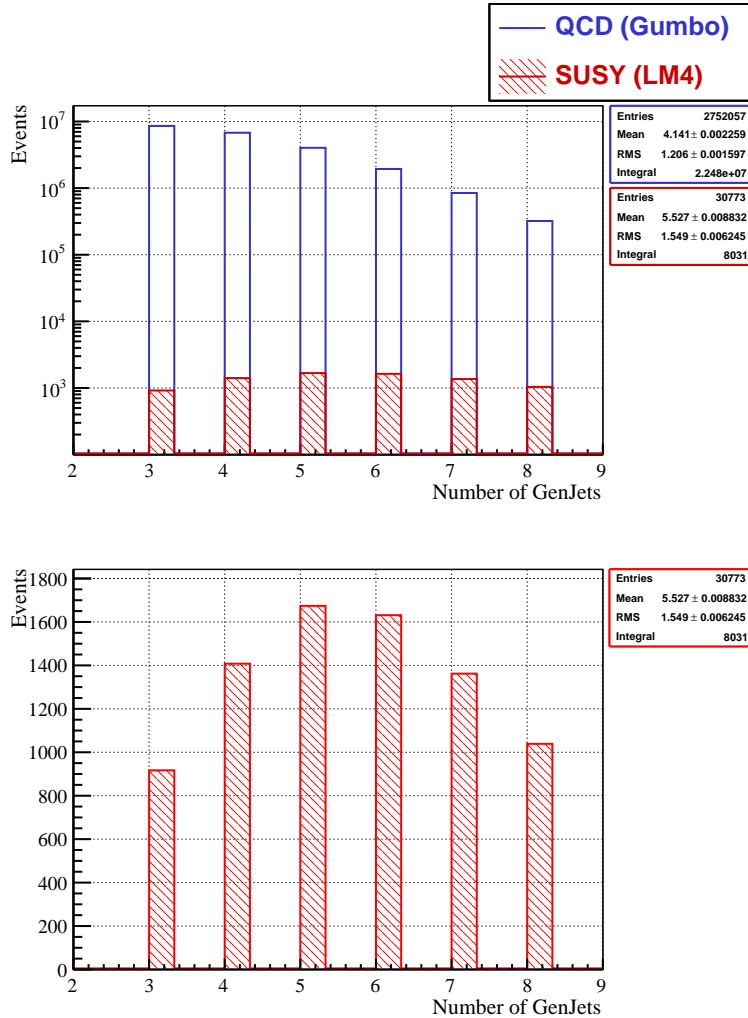
Figure 6.10: **Upper plot**: Distribution of the the jet multiplicity in the QCD and the SUSY LM4 sample. **Lower plot**: Distribution of the jet multiplicity in the SUSY LM4 sample. **Both plots** show only GenJets which passed all selection criteria.

five or six jets. These different multiplicity distributions motivated the definition of the A_6 variable, since demanding at least six jets, one rejects the largest QCD contributions, while still taking the dominant SUSY contribution into account.

Figures 6.11 and 6.12 show normalised (area =1) distributions of the exact antenna variable A_{n*} for $n = 3, 4, 5, 6, 7, 8$. For later convenience all variables are multiplied by (-1), what causes the distributions of the variables computed from SUSY events to have larger values of the antenna variables than the distributions of the antenna variables computed from QCD events. **From here on the values of the *negative* antenna variables are discussed, in order that the discussion is consistent with the plots.**

The distributions are shifted to ever larger values (smaller values before the multiplication with (-1)) with increasing number of jets because of the rising number of four momenta products in the antenna structures of the variables — there are $n+2$ products for n jets. From here on distributions of various antenna variables A_n computed from the QCD data set are denoted as A_n^{QCD}, while the distributions of

the same variables computed from SUSY events is denoted as A_n^{SUSY}. The relative
displacement of the A_n^{QCD} and A_n^{SUSY} distributions (difference between the mean
values) increases with increasing number of jets. This can be explained by different
origins of the additional jets in QCD and SUSY case. The additional QCD jets are
created mainly by gluon radiation (see section 6.2 for explanation) and tend to have
small opening angle to the generating parton, which leads to small values of the four
products and hence small antenna values. There are of course also contributions of
the true multiparton processes involving quarks. In the SUSY case, selecting more
jets one selects longer decay cascades of supersymmetric particles, which leads to
more jets with larger opening angles and larger antenna variable values in compar-
ison with QCD. Boosted secondary decay products lead in fact also to collimated
jets, but in average the event structure differs from the one of QCD. The width of
all antenna distributions rises as well with increasing number of jets. As a reminder:
the "width" of such logarithmic quantity ($\ln A$) is dependent on the event rate in
a give range of the pre-logarithmic quantity (A). The more events are in a given
range of A the steeper is the slope of the $\ln A$ distribution, and vice versa for the
fall. The enlargement of the width in the logarithmic plot means, that the density of
the pre-logarithmic antenna values decreases. With increasing number of jets there
are increasing number of possibilities to arrange the jet-momenta in the space and
hence the range of the possible antenna values becomes larger, but the number of
events decreases (cross section falls), leading to fewer events in a given range and
hence to the slow rise and fall of the logarithmic distribution.

Figure 6.13 shows normalised distributions of the A_3, A_{3plus} and A_6 variables. The A_3
variable performs better (has higher separation power) than the exact A_{3*} variable,
although they have comparable "widths". This fact is not surprising, since the
width depends mainly on the number of jets. The mean of the A_3^{QCD} distribution is
comparable with the mean of the exact A_{3*}^{QCD} distribution, since the contribution of
the 3-jet events is dominant (see Fig. 6.10), and the three leading jets taken from
all other (non three jets) QCD events seem to resemble pure QCD 3-jet events. The
gain of the discrimination power originates from the shift of the A_3^{SUSY} distribution
to lower values compared with the A_{3*}^{SUSY} distribution. This shift can be explained
by completely different SUSY event structure. Pure SUSY 3-jet events are the minor
contribution to the A_3^{SUSY} distribution, while the three leading jets originating from
events with higher jet multiplicities are well separated leading to large invariant
masses.

The A_{3plus} variable shows a similar behaviour. The dominant 3-jet contribution in
the A_{3plus}^{QCD} case can be seen directly as a second maximum of the distribution. The
contribution from events with higher jet multiplicity pushes the variable to higher
values, since the third jet being a four vector sum of all, but the two leading jets, is
well separated from the others and has additionally large energy component. The
heterogeneous composition of the distribution of the A_{3plus} variable computed from
QCD events manifests itself in its large width. The A_{3plus}^{SUSY} distribution benefits
even more from the definition of the third jet. Its huge energy component drives the
momenta products to higher values and reduces the range of all possible values of
the antenna variable (increases the event rate per given range) and hence the width
of the distribution. The 3-jet SUSY events contribute to the tail of the A_{3plus}^{SUSY}
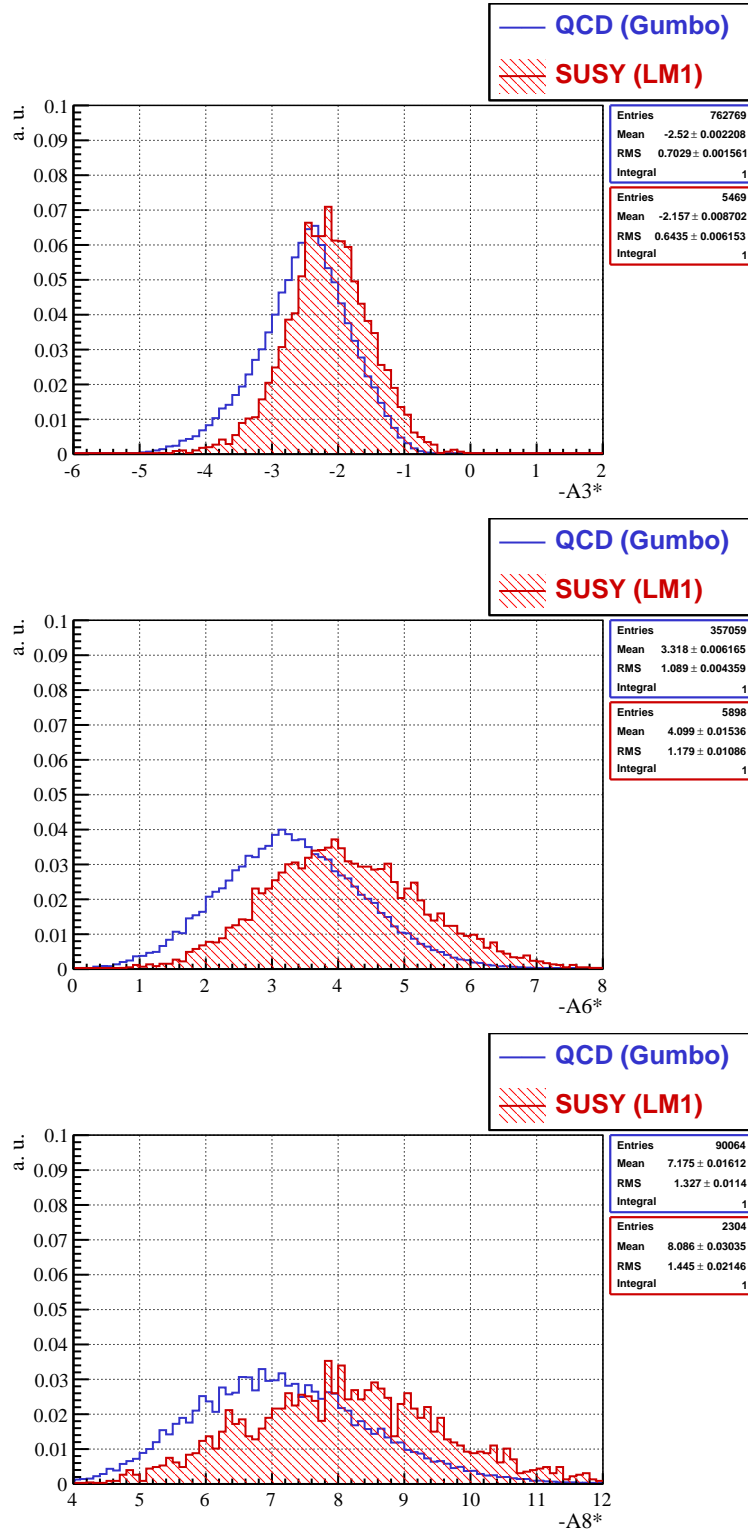distribution at low antenna values.
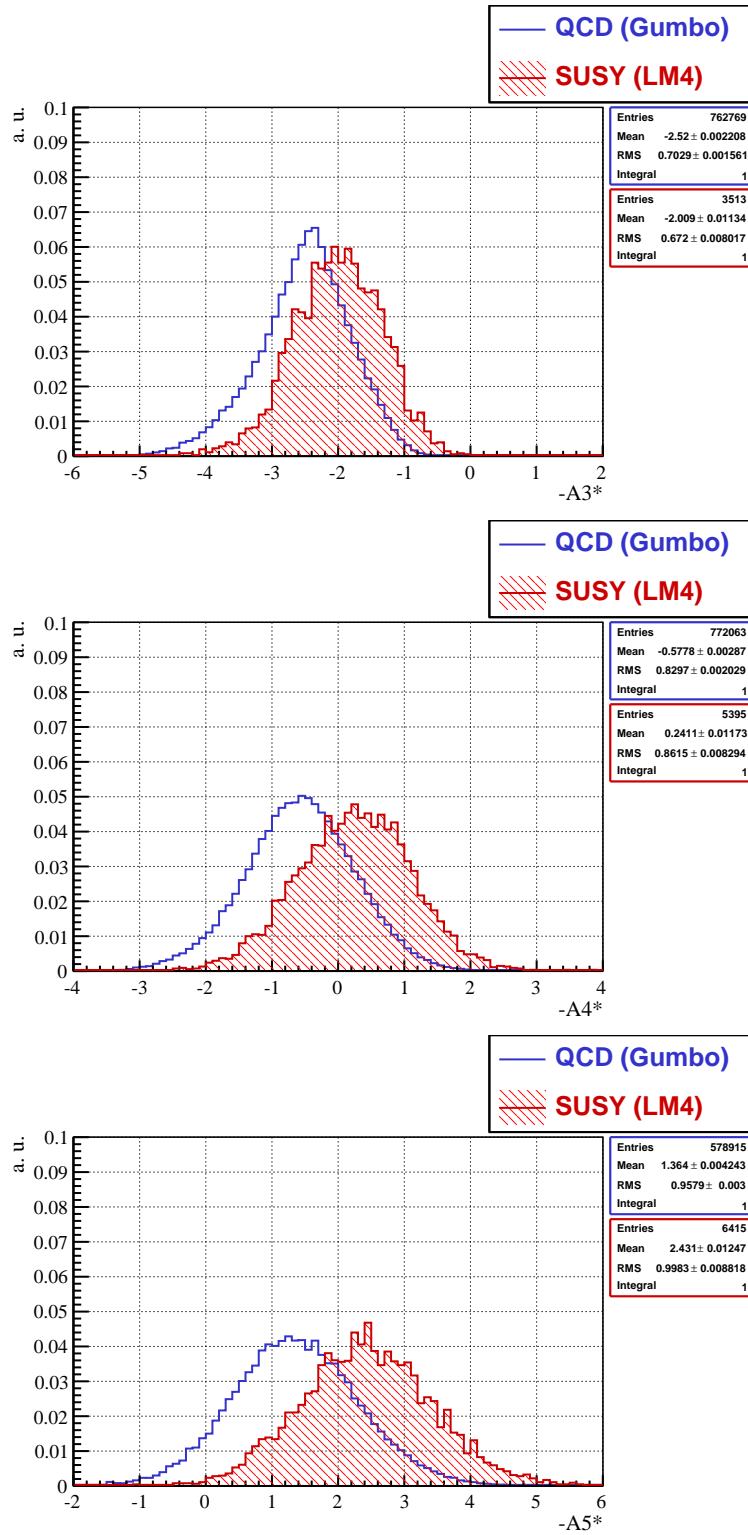
Figure 6.11: Normalised distributions of the negative exact antenna variable for 3,4, and 5 GenJets in the final state for the QCD and SUSY LM4 sample.
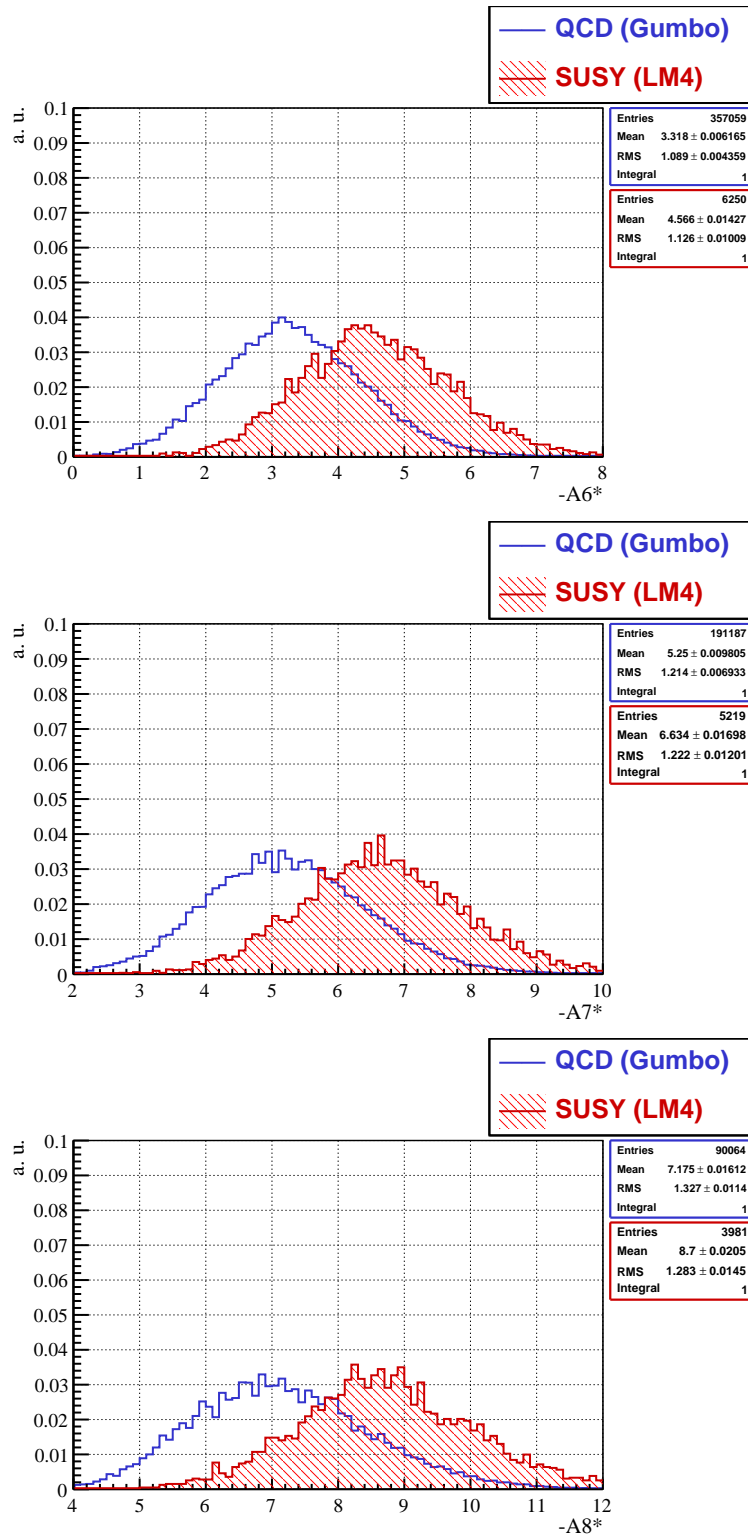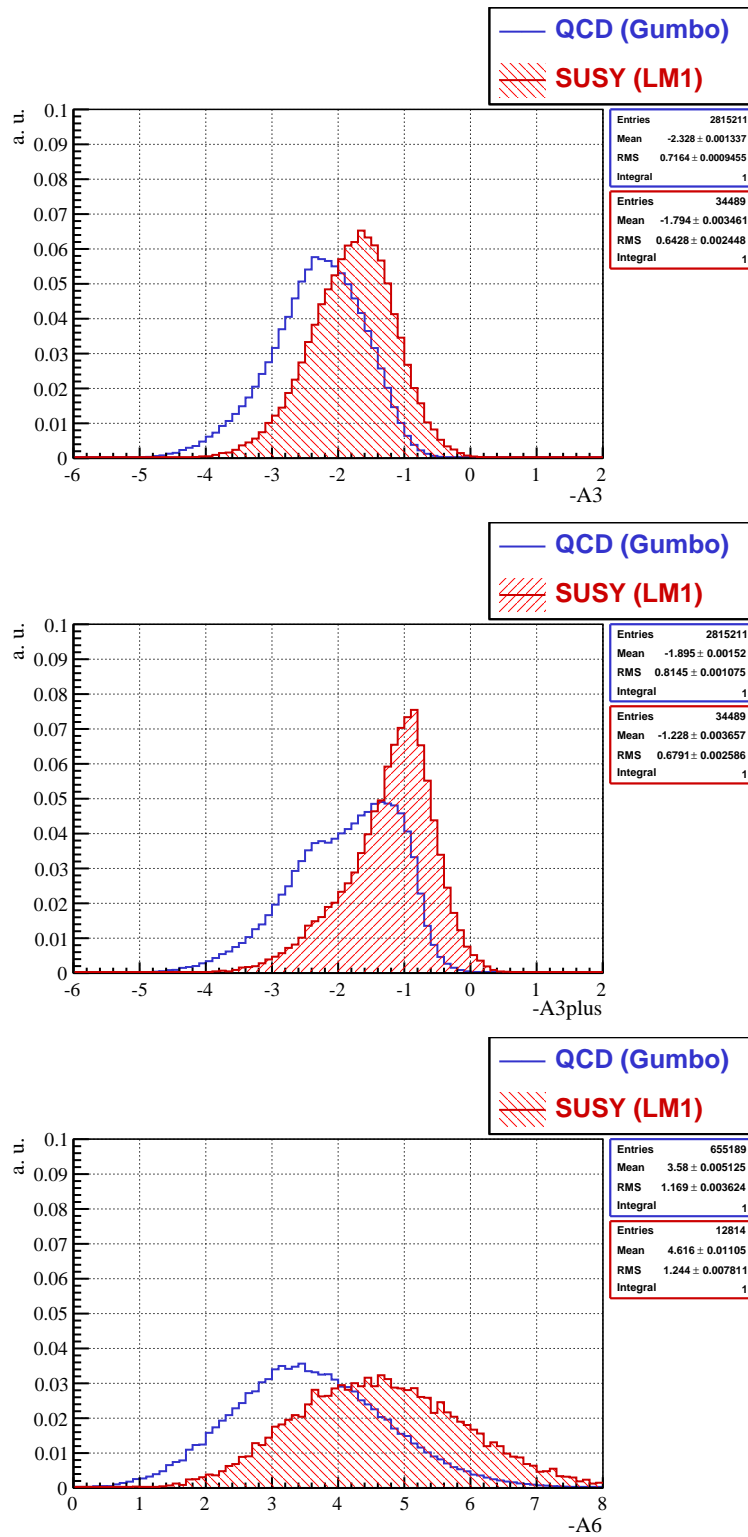
Figure 6.12: Normalised distributions of the negative exact antenna variable for 6,7, and 8 GenJets in the final state for the QCD and SUSY LM4 sample.

The distribution of the A_6 variable shows also the expected pattern. The width of both A_6^{QCD} and A_6^{SUSY} distributions is large due to the high number of jets. True 6-jet events are the dominant contribution to the A_6^{QCD} distribution, because of the steep fall of the QCD multijet cross section. Hence the mean of the A_6^{QCD} distribution resembles the mean value in the A_{6*}^{QCD} case. The A_6^{SUSY} distribution receives valuable contributions also from events with higher number of jets. The six leading jets of such events lead to larger antenna values, similarly to the case of the A_3^{SUSY} distribution.

Having seen the distributions for the SUSY LM4 point as signal scenario, one can compare them with the distributions assuming that the signal is given by the SUSY LM1 point. It is sufficient to compare distributions of key variables. The normalised distributions of exact antenna A_{3*}, A_{6*} and A_{8*} variables are shown in Fig. 6.14, while Fig. 6.15 shows the distributions of the normalised A_3, A_{3plus} and the A_6 variables. All antenna variables have less discrimination power than in the SUSY LM4 case. This behaviour is expected, q.v. beginning of this chapter, and approves the understanding of the variables. It follows that the antenna variables show their potential (before the cuts on different kinematic variables) mainly in cases of signal scenarios with higher primary particle masses than in the SUSY LM1 case. For this reason SUSY LM4 point is chosen as the main reference.

6.5 Effects of jet reconstruction

In the next step the transition from GenJets to the jets reconstructed from the measured values of the calorimeter cells, the so called CaloJets, is undertaken. In both cases jets were build with the k_t Jet finder ($R = 0.4$). To account for the impact of various technical and physical processes, which depend on the energy and the detector region, the energies of measured jets are corrected using a Monte Carlo-based correction method[6]. This method is based on the comparison between the transverse jet energies of Gen- and CaloJets, which were produced by the same jet algorithm and matched to each other via $\Delta R = \sqrt{\Delta\eta^2 + \Delta\phi^2}$ matching, in different η and p_t regions. After the comparison, the transverse energies of the CaloJets are corrected by multiplication with a factor depending on their transverse energies and locations in η [49].

The following cuts were applied to all CaloJets:

- $p_t > 20\ GeV$,

- $|\eta| < 3.0$.

Similar to the GenJet level additional cuts were applied to the two leading Jets:

- $E_t^{j(1)} > 200\ GeV$,

- $E_t^{j(2)} > 150\ GeV$,

- $\left|\eta^{j(1)}\right| < 1.5.$,

---

[6]CMSSW MCJetCorrections 152
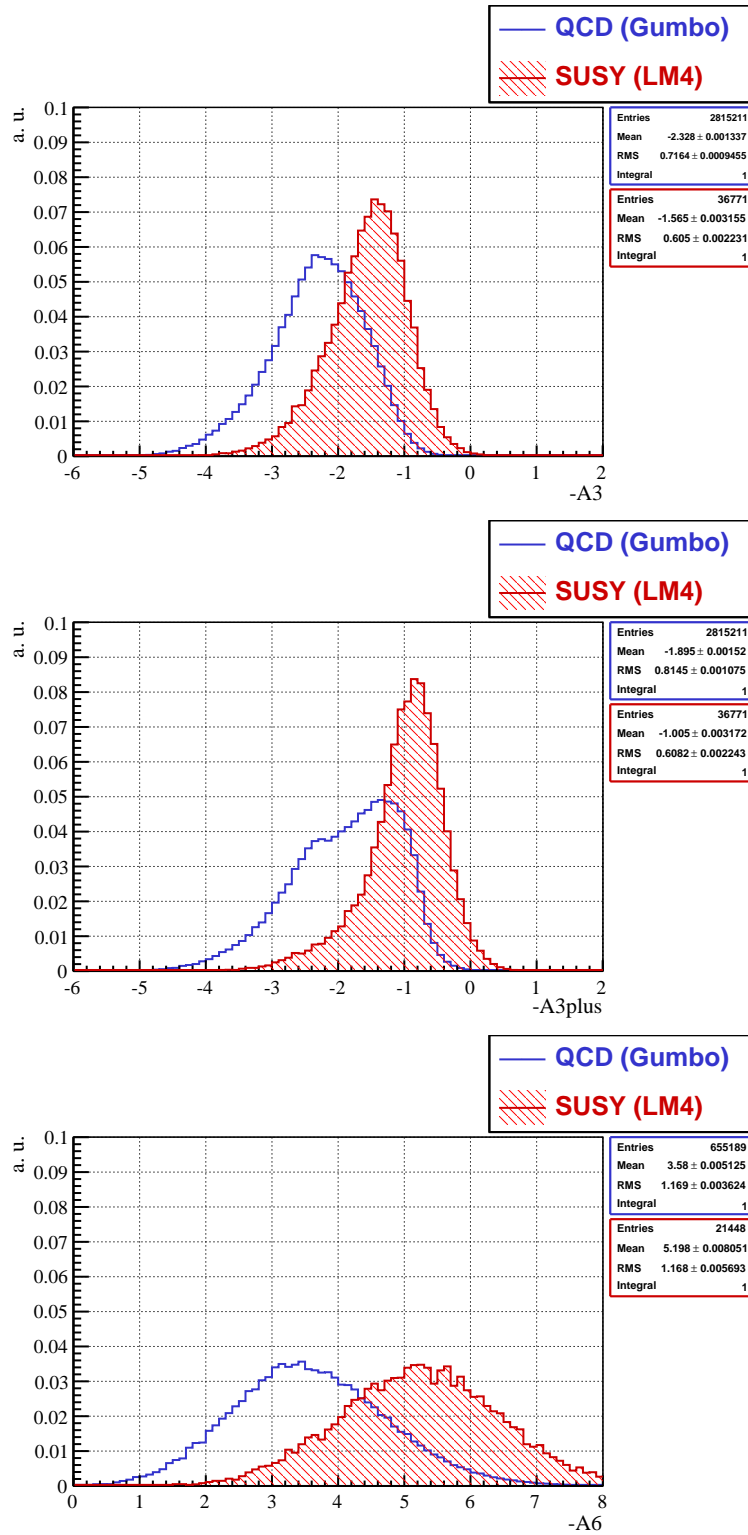
Figure 6.13: Normalised distributions of the negative A_3, A_{3plus} and A_6 variables for the QCD and SUSY LM4 sample. The variables are constructed from GenJets.

Figure 6.14: Normalised distributions of the negative exact antenna variable for 3, 6, and 8 GenJets in the final state for the QCD and SUSY LM1 sample.

Figure 6.15: Normalised distributions of the negative A_3, A_{3plus} and A_6 variables for the QCD and SUSY LM1 sample. The variables are constructed from GenJets.
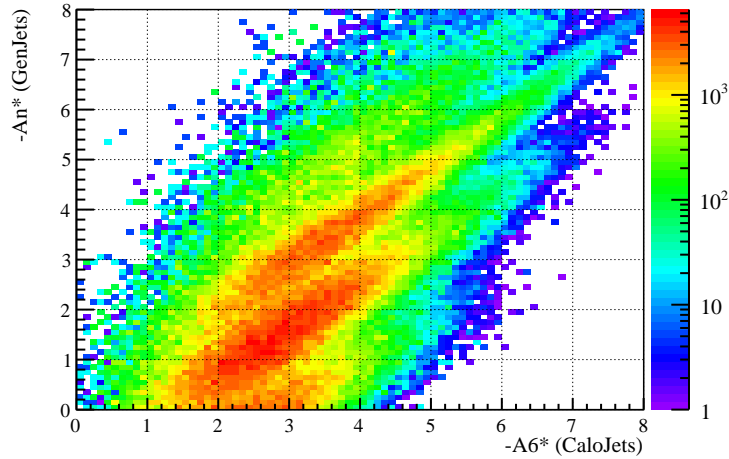
Figure 6.16: Correlation between the values of the $-A_{6*}^{QCD}$ variable computed from CaloJets and the values of the corresponding GenJet $-A_{n*}^{QCD}$ variable in each event. Colour code indicates the number of events.

where E_t is the transverse Energy: $E \sin \theta$. E is the scalar sum of energy deposited in the calorimeter towers. All cuts resemble the cuts on the GenJet level.

In order to understand the possible deviations between the distributions on the GenJet- and CaloJet-level, a plot of the correlation between the values of the A_{6*} variable computed from the corresponding jets for the QCD sample is shown in Fig. 6.16. The plot shows the value of the negative exact A_{6*}^{QCD} variable computed in each event, which passed the thresholds on the calorimeter level, from CaloJets vs. the value of the antenna variable computed from the GenJets of the same event. The major fraction of the events lies not on the main diagonal. However, the distributions of events follows some pattern. The events are concentrated on and around lines, whose slopes are either larger or smaller than the slope of the main diagonal. Most events have higher values of the variable computed from the CaloJets in comparison with the variable computed from the GenJets. Only a small fraction of the events shows a diametric opposite behaviour. The reason for such abnormal correlations lies in the fact, that selection of exact 6, or in general $N_{CaloJets}$, jets on the calorimeter level does not imply that the selected events contain also exact 6 GenJets. Figure 6.17 shows the number of GenJets in the selected events. It turns out, that events with some exact number of CaloJets are a mixture of events with different GenJets numbers. The events with 5 or 4 GenJets contribute mostly to the events with exactly 6 CaloJets. The contributions from events with 3 or 7 GenJets lie in the same order of magnitude. The dominance of the 4- and 5-GenJets events is rooted in the fast decrease of the QCD multijet cross section with the growing number of jets. This fact is also reflected in the Fig. 6.10. The huge number of QCD 4 jet events leads to the fact, that the fraction of the 4 GenJet events which are reconstructed as 6 jet events is even larger than the actual number of 6 GenJet events reconstructed as 6 CaloJet events. However, the probability to create an event with $N_{CaloJets}$ CaloJets out of event with less or more GenJets seems to fall steeply if $\Delta N = N_{CaloJets} - N_{GenJets}$ is too large. Otherwise events with 2 and 3 GenJets would dominate the distribution, due to the large cross sections. As a comparison the number of GenJets in events with exact 3 CaloJets is shown in Fig.
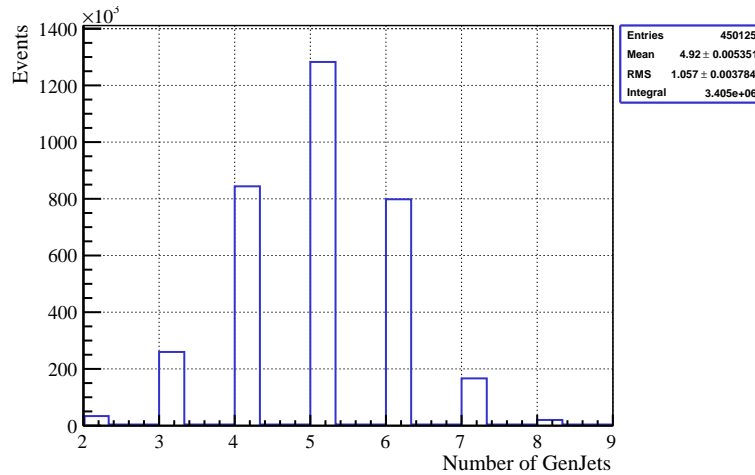
Figure 6.17: Number of GenJets in the events from the QCD sample which passed the selection criteria and entail exactly 6 CaloJets
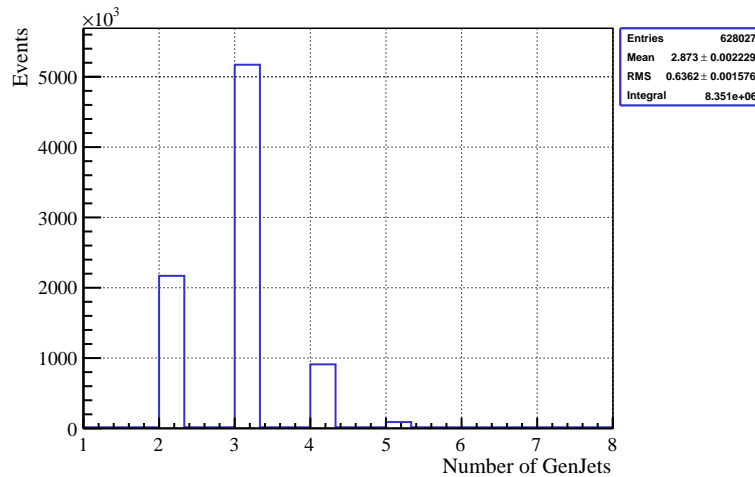
Figure 6.18: Number of GenJets in the events from the QCD sample which passed the selection criteria and entail exactly 3 CaloJets

6.18. Figures 6.17 and 6.18 suggest, that if the events were equally distributed in each n-GenJet bin, the major contribution would come either from the events with $N_{GenJets} = N_{CaloJets}$ or from the events with $N_{GenJets} = N_{CaloJets} \pm 1$. In the case of 6 CaloJets the distribution that would emerge from this rule of thumb is convoluted with the steep fall of the n-jet cross section.

The events with different number of GenJets populate different lines in the correlation plot 6.16. If there are less GenJets in the event than CaloJets, the correlation will lie on the line below the main diagonal, since the variable tends to smaller values for smaller jet numbers. In the opposite case where $N_{GenJets} > N_{CaloJets}$ the events will occupy the line above the main diagonal. Restricting the number of GenJets to the number of CaloJets produces the desired correlation where all events occupy the domain around the main diagonal, see Fig. 6.19, with reasonable resolution and small bias.
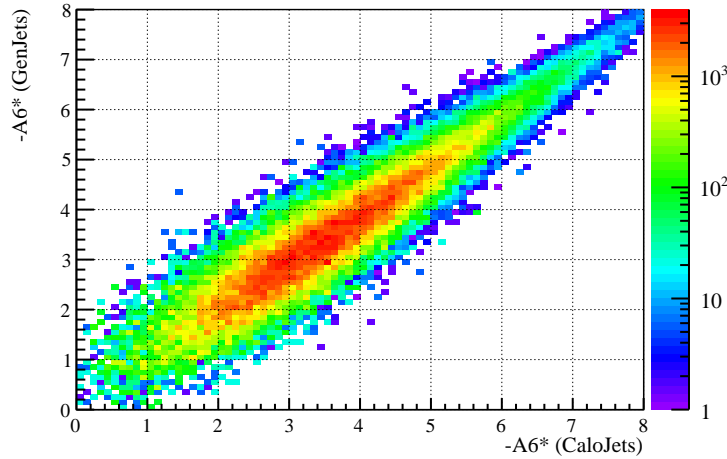
Figure 6.19: Correlation between the values of the $-A_{6*}^{QCD}$ variable computed from Calo- and GenJets, after the number of GenJets was restricted to six. Colour code indicates the number of events.

The impact of the different populations inside the set of events with exact number of CaloJets can be seen in Fig. 6.20, where the distributions of the $-A_{3*}^{QCD}$ and the $-A_{6*}^{QCD}$ are shown on the generator and the calorimeter level. Only events which pass the thresholds corresponding to each level are plotted. The distributions of the $-A_{3*}^{QCD}$ variable look similar on both levels. The numbers of events are comparable, the number of GenJet events is slightly higher than the number of CaloJet events. This can be understood, since some of the events with 3 GenJets are reconstructed having 4 or 2 CaloJets. The contributions of the events with 2 or 4 GenJets, which are reconstructed as events with 3 CaloJets are not enough to compensate this loss. The value of the $-A_{3*}^{QCD}$ distribution is shifted to smaller values on the calorimeter level. The reason for this shift will be explained in the case of the $-A_{6*}^{QCD}$ variable. The width of the CaloJet distribution is slightly larger than the width of the GenJet distribution and will be also explained in the discussion of the $-A_{6*}^{QCD}$ variable.

The impact of the transition to the calorimeter level on the $-A_{6*}^{QCD}$ variable is much larger compared to the shift of the $-A_{3*}^{QCD}$ distribution. The number of events with exactly 6 CaloJets outweighs the number of events with exactly 6 GenJets. Most of these additional events have 4 and 5 GenJets, which were reconstructed as 6 CaloJets. The mean of the distribution is shifted to smaller values compared with the mean on generator level by ca. 0.567.

This shift can be explained, assuming that the additional CaloJets (the jets which have no counterpart on the generator level) in the events having 4 or 5 GenJets originate from one of these GenJets which was reconstructed as two very close CaloJets sharing the energy of the original GenJet. In this work such CaloJets are called partner jets. Partner jets would push the variable to smaller values because of two reasons. First of all, these jets have small angular separation to their partner, which leads to small values in the denominator of the antenna structure. The second reason relies on the fact, that the two CaloJets originating from one GenJet share its energy
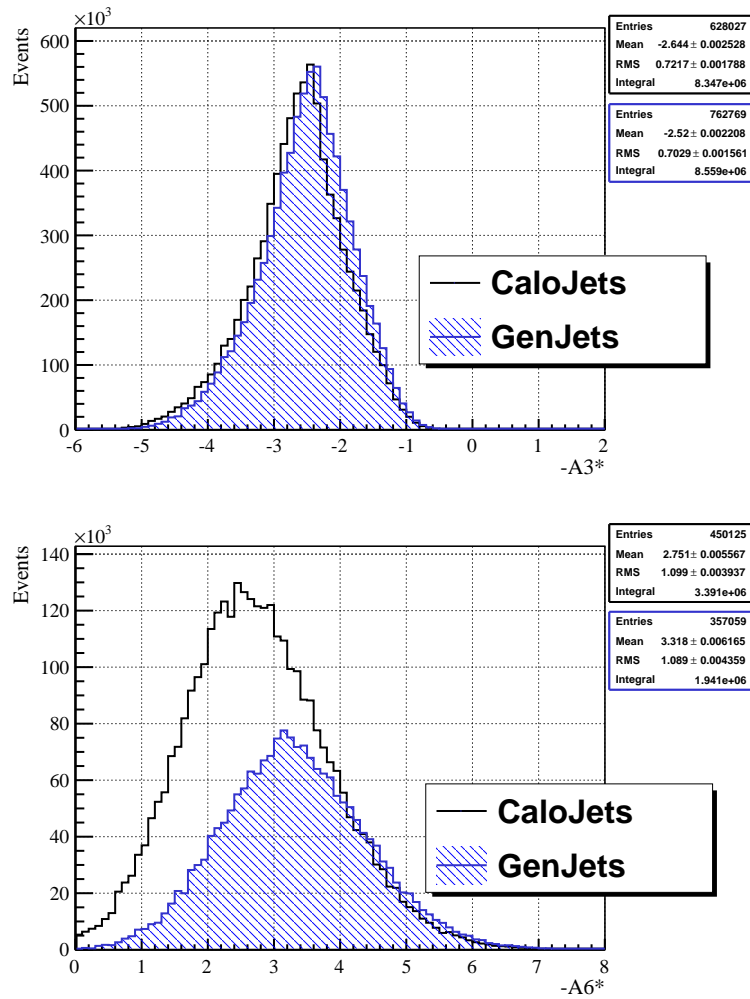
Figure 6.20: Distributions of the $-A3*^{QCD}$ and $-A6*^{QCD}$ variables. Black curves are indicating the distributions of the variables on the calorimeter level, while the blue curves show the distributions on the generator level.

and thus have smaller invariant mass than the events with 6 Gen- and CaloJets[7], independent from angular structure of the jets.

In order to verify the statements from the previous paragraph, the characteristics of the generator-level content of the events with 6 CaloJets is examined. Figure 6.21 shows distributions of the $-A_{6*}^{QCD}$ variable computed from events having 6 CaloJets, but different number of GenJets. The mean value is similar to the value of the $-A_{6*}^{QCD}$ computed from GenJets, cf. Fig. 6.20, but the number of events is approximately 1/3 of the number of all events having 6 GenJets. The missing fraction contributes to distributions with other numbers of CaloJets, similar to the case of the $-A_{3*}$ variable. The distributions of events having 4 and 5 GenJets are shifted to ever smaller values with decreasing number of GenJets.

6.5.1 HT dependence

Figure 6.22 shows the distribution of the HT variable for the same classes of events. The HT variable is the scalar sum of the transverse energies of all CaloJets in the event $HT = \sum_i E_T^{jet_i}$, and is by definition connected with invariant masses present in the event. The HT^{QCD} distributions resemble the pattern of the $-A_{6*}^{QCD}$ distributions. The CaloJets in the events having $N_{CaloJets} = 6$ but $N_{GenJets} = 4$ carry less energy than the CaloJets in the events from the $N_{CaloJets} = 6$, $N_{GenJets} = 5$ class, which contain in turn less energy than events with 6 Calo- and GenJets. This pattern arises, because the n ($n = 6_{CaloJets} - N_{GenJets}$) additional jets do not carry additional energy but rather share energy with their partner jets, as stated above. In fact one is essentially comparing energy contents of 4, 5 and 6 jet events, and not energy contents of true 6 jet events. This energy dispersion leads, in addition to angular effects, to the observed shift of the $-A_{6*}^{QCD}$ variable after the transition to the calorimeter level, since the smaller the energies in the denominator the smaller the values of the (negative) antenna variables.

In order to asses the relevance of the HT dependence in comparison with the angular effects, Fig. 6.23 shows the distributions of the $-A_{6*}^{QCD}$ variable computed from events with a different number of GenJets, after HT of the events was restricted to the $900 - 1400$ GeV bin. This HT bin was chosen, because it lies beyond the region where the main differences in the HT variable occur. All distributions are shifted to larger antenna values in comparison with Fig. 6.21, but the displacement of the distributions with respect to each other retains. The HT cut suppresses furthermore mainly events with 4 GenJets, as expected. The relative displacement of the distributions seems truly to originate from the angular separation of the jets and not purely from the different energy contents. The heterogeneity of the $-A_{6*}$ distribution on calorimeter level yields a larger width in comparison with the generator level distribution, due to the larger spread of the possible antenna values.

In order to estimate the effect of the transition to the calorimeter level on the discrimination power of the variable, the distribution of the $-A_{6*}$ variable on both levels is also shown for the SUSY LM4 dataset in Fig. 6.24. Contrary to the QCD case, both distributions lie in the same range, the distribution on the calorimeter

---

[7]As stated in the introductory section of this chapter, the antenna variables are proportional to the averaged inverse invariant mass of the event.
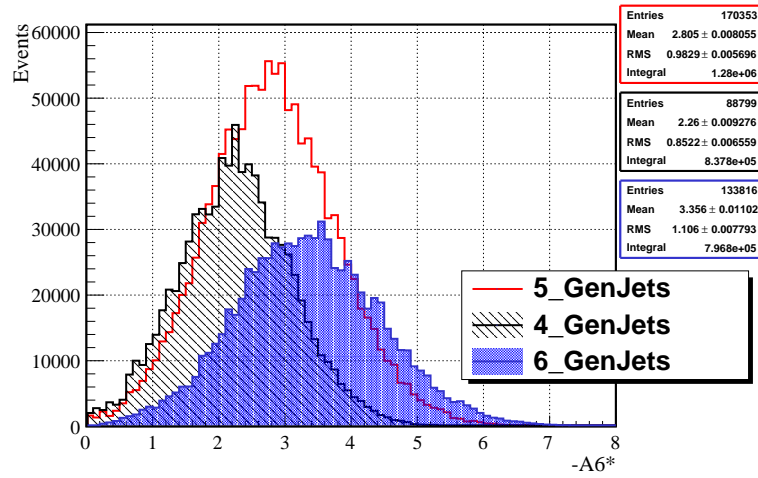
Figure 6.21: Distributions of the $-A_{6*}^{QCD}$ variable computed from events having 6 CaloJets, but different number of GenJets. The red curve shows the distribution for the events having 5 GenJets, the black curve shows the distribution for the events with 4 GenJets, and the blue curve shows the distribution for the events with 6 GenJets.
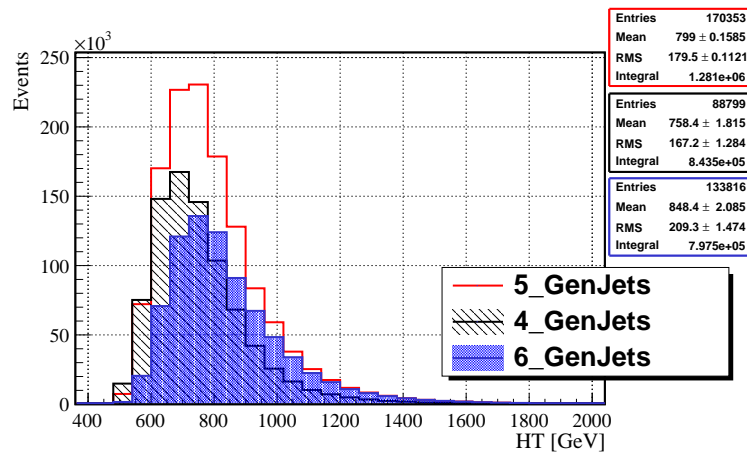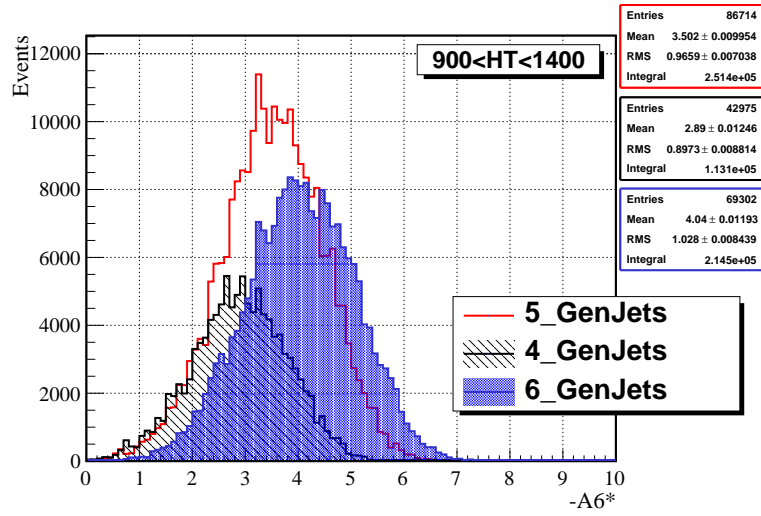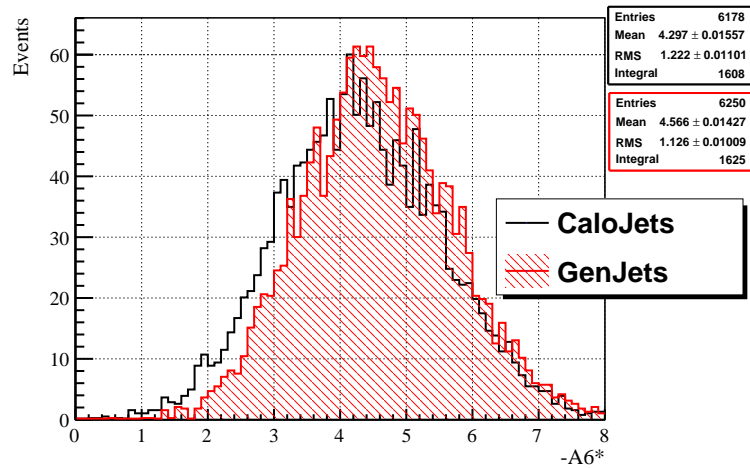

Figure 6.22: Distributions of the HT^{QCD} variable computed from events having 6 CaloJets, but different number of GenJets. The red curve shows the distribution for the events having 5 GenJets, the black curve shows the distribution for the events with 4 GenJets, and the blue curve shows the distribution for the events with 6 GenJets.

Figure 6.23: Distributions of the $-A_{6*}^{QCD}$ variable computed from events having 6 CaloJets, but different number of GenJets, in the $900\ GeV < HT < 1400\ GeV$ bin. The red curve shows the distribution for the events having 5 GenJets, the black curve shows the distribution for the events with 4 GenJets, and the blue curve shows the distribution for the events with 6 GenJets.

Figure 6.24: Distributions of the $-A6*^{SUSY}$ variable. The black curve shows the distribution on the calorimeter level, while the red curve is indicating the distributions of the variable on the generator level.
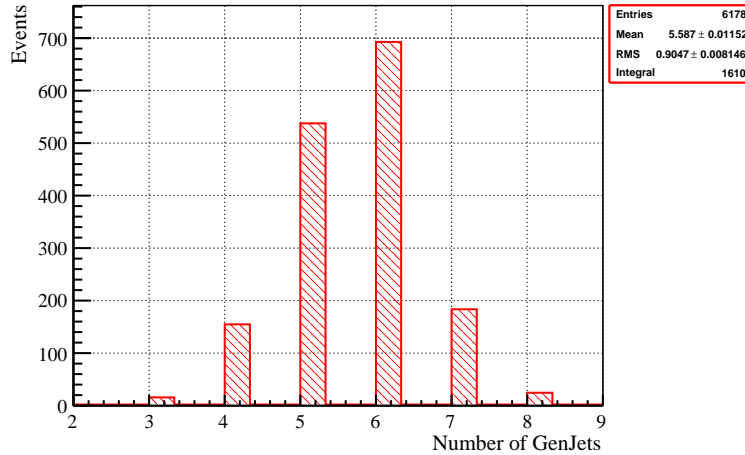
Figure 6.25: Number of GenJets in the events from the SUSY LM4 sample which passed the selection criteria and entail exactly 6 CaloJets.

level being slightly shifted to smaller values. Figure 6.25 shows the number of GenJets in the events, which entail exactly 6 CaloJets. The dominant contribution comes from the events with 6 GenJets explaining the small displacement of the $-A_{6*}^{SUSY}$ distribution. The different structure of the 6 jet SUSY LM4 events on calorimeter level in comparison with the 6 CaloJet QCD events is rooted in the different cross sections for the multijet production. In general all antenna variables computed from SUSY events A_n^{SUSY} are also displaced to smaller values due to the splitting of the GenJets, similar to A_n^{QCD}, but this shift is smaller than the shift of the corresponding A_n^{QCD} distributions. This difference yields a relative displacement of the QCD and SUSY antenna distributions with respect to each other, after the transition to the calorimeter level.

6.6   Results on detector-jets level

This section presents distributions of the various antenna variables computed from CaloJets. Fig 6.26 shows the normalised distributions of the negative exact antenna variables A_{3*}, A_{6*}, and A_{8*}, while Fig. 6.27 shows the normalised distributions of the negative A_3, A_{3plus} and A_6 variables. All antenna variable have preserved their discrimination power. The A_6 variable is affected from the same effect as the A_{6*} variable, since the events having exactly 6 CaloJets contribute mostly in the SUSY and in the QCD case (both cross section fall when the number of jets exceeds 6) to the inclusive A_6 variable. The behaviour of all variables resembles the behaviour on the generator jet level.

In summary, the transition to the calorimeter level can be undertaken. The distributions of the variables computed from the QCD and SUSY LM4 datasets are even more displaced in relation to each other, compared with the generator level, due to the different multijet cross sections as described above. The extent of the displacement depends on the number of jets the variable makes use of. The displacement is growing with increasing number of jets. However, the use of the exact antenna A_{n*} variables is problematic, since in general they compare events which have different
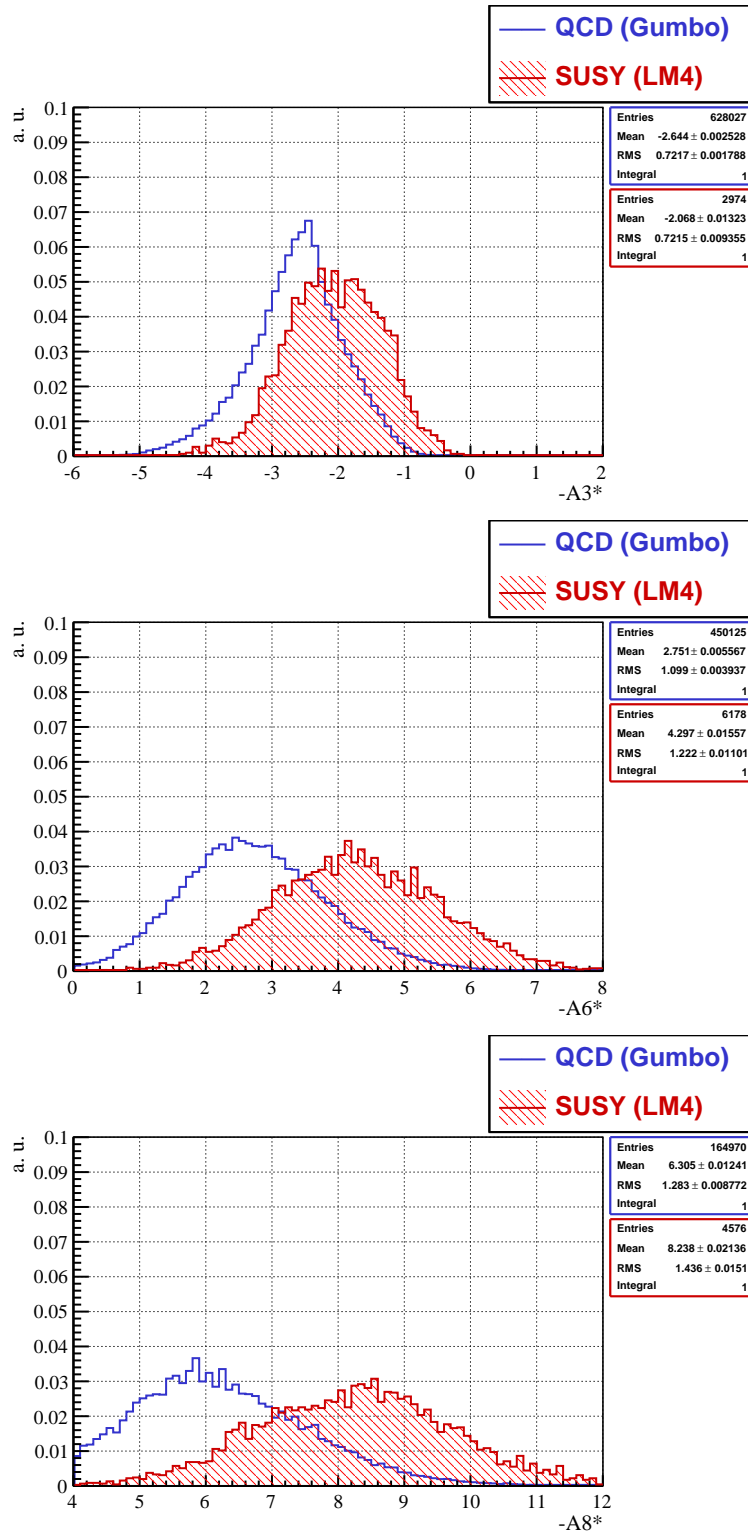
Figure 6.26: Normalised distributions of the negative exact antenna variable for 3,6, and 8 CaloJets in the final state for the QCD and SUSY LM4 sample.
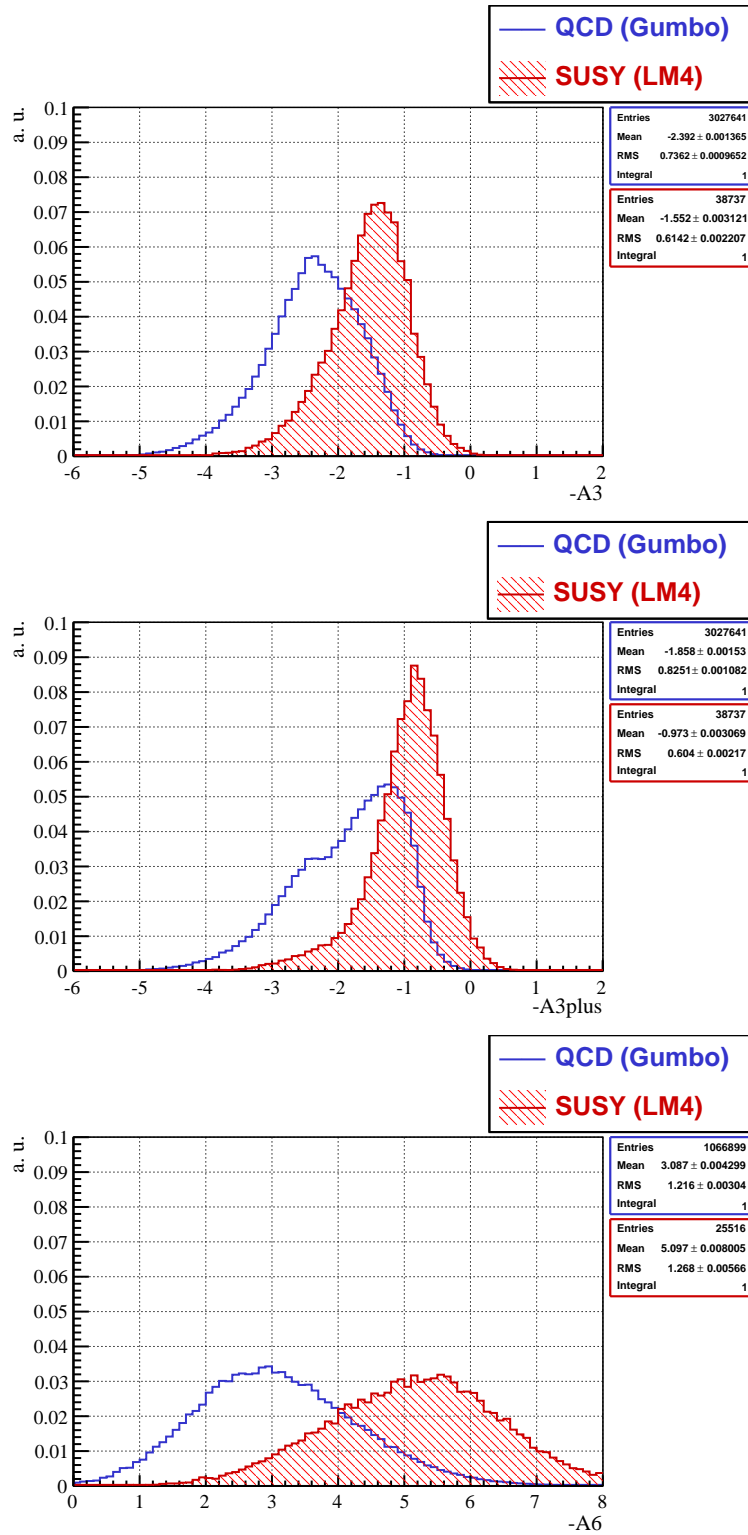
Figure 6.27: Normalised distributions of the negative A_3, A_{3plus} and A_6 variables computed from CaloJets for the QCD and SUSY LM4 sample.
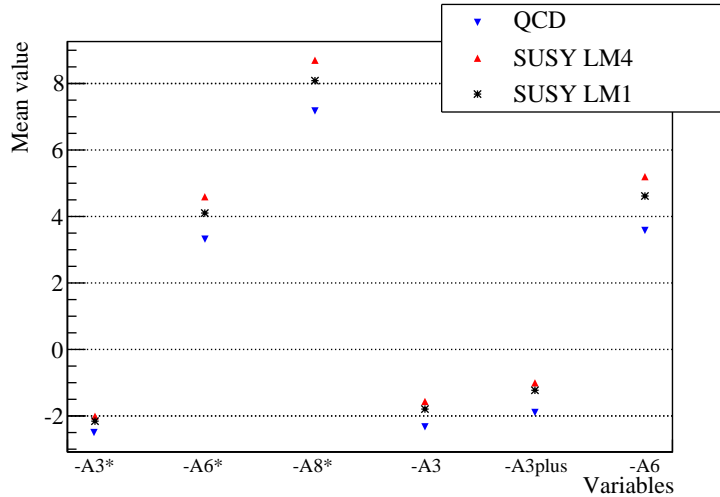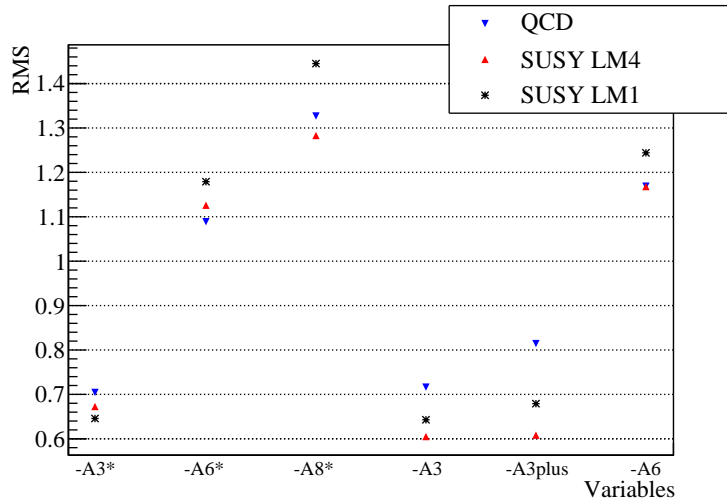
Figure 6.28: Mean values of the negative A_{3*}, A_{6*}, A_{8*}, A_3, A_{3plus}, and A_6 antenna distributions computed from QCD, SUSY LM4, and SUSY LM1 events on hadron-jets level.

number of GenJets. For this reason, only inclusive A_3, A_{3plus} and A_6 variables will be used in the following studies.

6.7   Summary plots

In order to systematise the results presented so far, the mean and RMS values of different antenna distributions are compared in this section. Figure 6.28 shows the mean values of the A_{3*}, A_{6*}, A_{8*}, A_3, A_{3plus}, and A_6 antenna distributions computed from QCD, SUSY LM4, and SUSY LM1 events on hadron-jets level. Figure 6.29 shows the RMS values of the A_{3*}, A_{6*}, A_{8*}, A_3, A_{3plus}, and A_6 distributions computed from QCD, SUSY LM4, and SUSY LM1 events. The general behaviour of the mean and RMS values on hadron-jets level was discussed in section 6.4.

Figure 6.30 shows the mean values of the A_{3*}, A_{6*}, A_{8*}, A_3, A_{3plus}, and A_6 antenna distributions computed from QCD and SUSY LM4 events on detector level. The RMS of the corresponding distributions are shown as errors of the mean values. The impact of jet resolution and reconstruction was discussed in the section 6.5, while section 6.6 presented the distributions of the antenna variables on detector-jets level.

6.8   Description of correlations

Important characteristics of the antenna variables are their possible correlations with other variables sensitive to the form of the events: the event shape variables. Also important are correlations of the antenna variables with the typical kinematic variables, which are used for the signal selection in the all-hadronic channel (if the signal is assumed to be SUSY) and are discussed in the next chapter.

Usually a correlation coefficient ρ_{xy} is introduced, in order to describe linear correlations between two variables x and y :

$$\rho_{xy} = \frac{cov(x, y)}{\sigma_x \sigma_y}, \tag{6.19}$$

Figure 6.29: RMS values of the negative A_{3*}, A_{6*}, A_{8*}, A_3, A_{3plus}, and A_6 antenna distributions computed from QCD, SUSY LM4, and SUSY LM1 events on hadron-jets level.
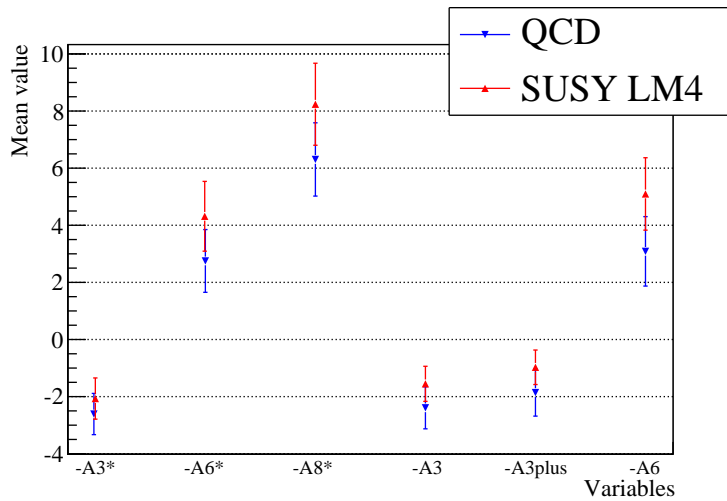
Figure 6.30: Mean values of the negative A_{3*}, A_{6*}, A_{8*}, A_3, A_{3plus}, and A_6 antenna distributions computed from QCD and SUSY LM4 events on detector-jets level. The RMS values of the antenna distributions are shown as errors of the mean values.

where $cov(x, y)$ is the covariance between x and y:

$$cov(x, y) = \iint (x - \langle x \rangle)(y - \langle y \rangle) \, dx dy. \tag{6.20}$$

$\langle x \rangle$ and $\langle y \rangle$ are the means of the distributions, while σ_x, σ_y are the standard deviations. The correlation coefficient has the value 1 (-1) for strongly correlated (anticorrelated) variables, and the value 0 if the variables are not correlated.

Being a single number for a two-dimensional distribution the correlation coefficient is often insufficient to understand the relationship between the two variables. Profile histograms offer often a more comprehensive description of the correlation of two quantities X and Y. The histogram displays the mean value of Y and its RMS for each bin in X. If the quantities are uncorrelated the distribution of the mean values is typically flat, otherwise the plot can reveal the functional dependency of Y on X.

In the following both techniques will be used to investigate the characteristics of the antenna variables.

6.9 Antenna as event shape variable

This section investigates the correlations between the antenna and the event shape variables. The event shape variables sphericity and thrust [75] are applied in the present approach to jets rather than to the single particles in order to describe the topologies of the events. These variables are defined by:

- Sphericity:
$$S = \frac{3\lambda_3}{\lambda_1 + \lambda_2 + \lambda_3}, \tag{6.21}$$

  where $\lambda_i (i = 1, 2, 3,)$ are the eigenvalues of the tensor

$$I_{\alpha\beta} = \sum_{i=1}^{N} (p_i^2 \delta_{\alpha\beta} - p_{i\alpha} p_{i\beta}) \tag{6.22}$$

  constructed in analogy to a tensor of inertia. The sum runs over all jets in the event. The eigenvalue λ_3 is the smallest among the three. The eigenvector belonging to λ_3 is called the sphericity axis of the event.

- Thrust:
$$T = \max_{\hat{n}} T(\hat{\mathbf{n}}), \tag{6.23}$$

  where

$$T(\hat{\mathbf{n}}) = 2U \sum_{i=1}^{N} \Theta(\mathbf{p}_i \cdot \hat{\mathbf{n}})(\mathbf{p}_i \cdot \hat{\mathbf{n}}), \tag{6.24}$$

  where

$$1/U = \sum_{i=1}^{N} |\mathbf{p}_i|, \tag{6.25}$$

  and Θ denotes the Heaviside step-function. The direction $\hat{\mathbf{n}}$ fulfilling Eq. 6.23 is called the thrust axis.

Sphericity is a measure of the summed $p_\perp^2$ with respect to the event axis. The range of the sphericity values is $0 \leq S \leq 1$. A pencil-like event corresponds to $S \approx 0$ and an isotropic event to $S \approx 1$. The allowed range of thrust is $1/2 \leq T \leq 1$, with a pencil-like event corresponding to $T \approx 1$ and an isotropic event to $T \approx 1/2$. First both event shape variables were selected for the present study, since they have different characteristics [75]. Sphericity is non linear in the momentum, weighting a single jet with large momentum higher than a group of jets with the same momentum. Thrust is linear and points always into the direction of the two subsets of the jets with the largest (and opposite) total momenta.

The antenna variables are also sensitive to the topology and the energy content of the events and are expected to be correlated with the event shape variables. Figure 6.31 shows the correlations between the three inclusive antenna variables and sphericity for the QCD and for the SUSY LM4 sample, while the corresponding correlation plots with thrust are shown in Fig. 6.32. As it can be inferred from the plots, thrust and sphericity are anticorrelated variables, which is also shown in Fig. 6.33. In spite of the different definition and characteristics, the correlation plots of the antenna variables with thrust do not entail much additional information with respect to the correlation plots with sphericity and vice versa. The discussion deals in the following only with sphericity, since correlation plots with thrust do not offer new information. In general the antenna variables computed from QCD events are stronger correlated with the event shape variables than the corresponding variables computed from SUSY events. However, there is also a correlation in the SUSY case.

The antenna variables computed from the first three leading jets of QCD events show strong correlation with sphericity and thrust in the domain of the low (high) sphericity (thrust) values. The correlation between the antenna variables computed from SUSY events and the event shape variables show similar pattern, the correlation being however not so much pronounced. The bulk of the SUSY events extends over a large domain of the sphericity values, contrary to the QCD events which are concentrated in the regions of low sphericity. This concentration roots in the dominance of the three-jet QCD events, which have often pencil-like structure and hence small sphericity values. SUSY events are not so much dominated by a single jet multiplicity bin with particular jet structure and thus can have various sphericity values. The correlation between small sphericity values and antenna variables occur in both distributions (computed from QCD and SUSY events) being more pronounced for QCD events, due to larger population in this region. The origin of the correlation lies in the pencil-like events which populate this sphericity region and lead also to very small values of the antenna variables, due to the close by jets. With increasing sphericity the correlation decreases. For a given large sphericity value the antenna variables can embrace very different values, the value being governed by the topology of the third jet, which has not so large contribution to the sphericity.

The A_6 variable, which is independent of the number of low jet multiplicity events, has lower correlation coefficient with both event shape variables, especially in the case of the SUSY distribution. Additionally the two dimensional distribution is broader in comparison with distributions of the both variables utilising 3 jets. This behaviour is due to the fact, that the event shape variables are most sensitive to the leading jets, while the antenna variables are also sensitive to the relative angular separation of the jets irrespective of the magnitude of their momenta. For a given
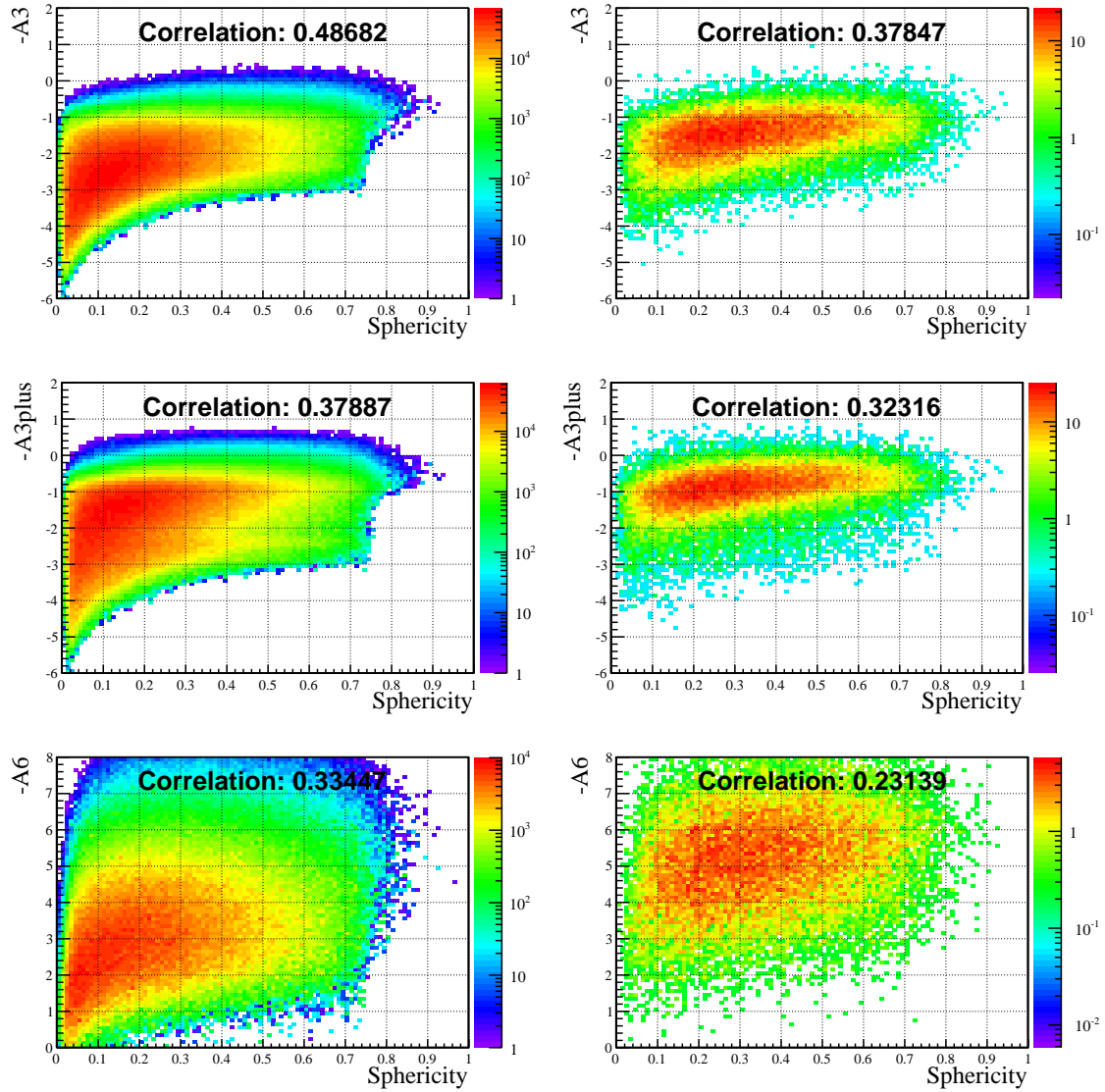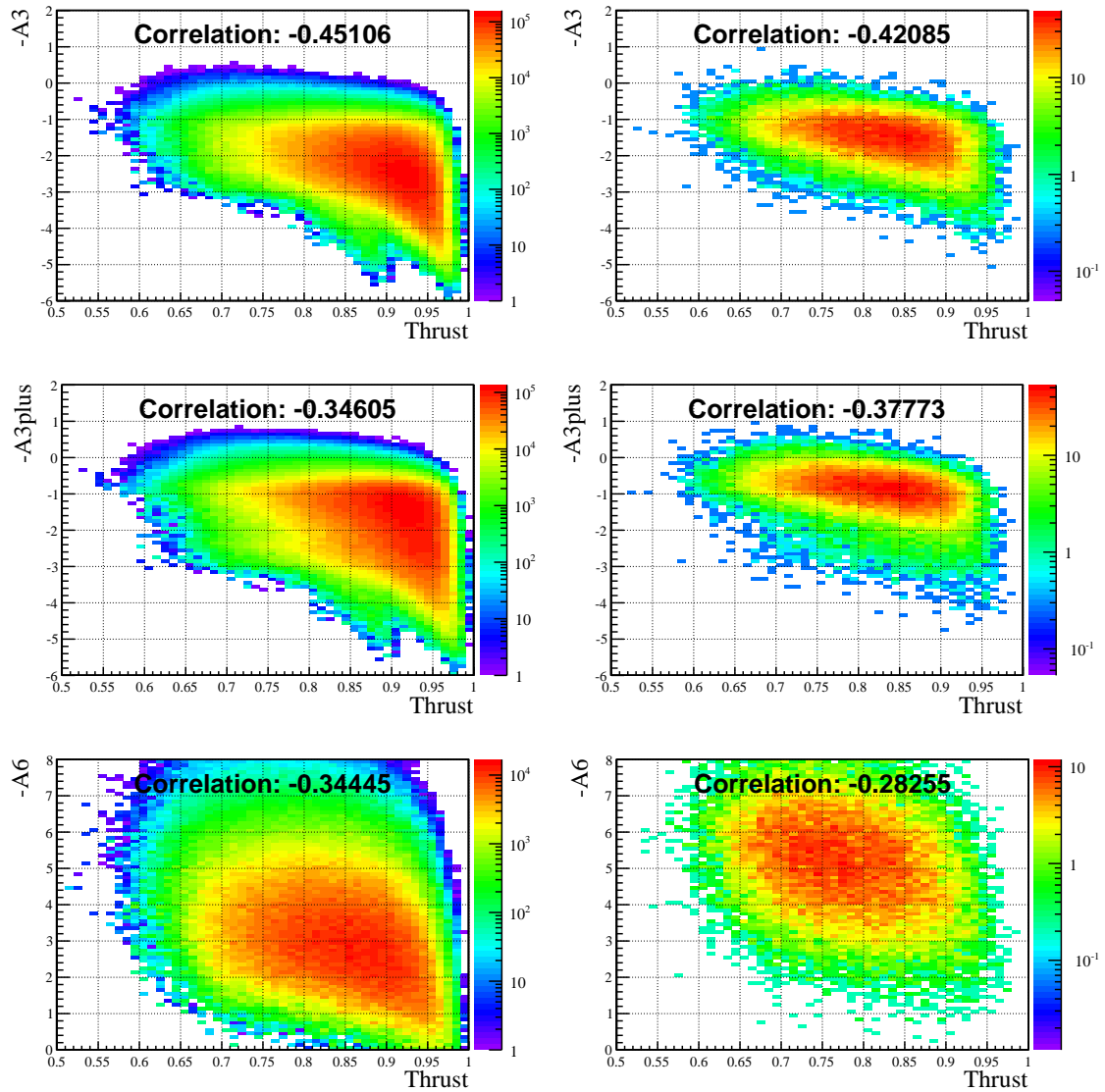
Figure 6.31: Distributions of the negative inclusive A_n variables computed from CaloJets vs. sphericity, for the QCD (**left**) and for the SUSY LM4 sample (**right**). Colour code indicates the number of events.

value of the sphericity, which is determined by the leading jets, the A_6 variable can have large variation of its values, which are determined by the arrangement of the additional jets in the event. In contrast, the values of the A_3 and the A_{3plus} variables cannot vary so much in a given sphericity bin, since the variation depends only on the third jet. In order to investigate the possible impact of the event shape variable cuts on the antenna variables, profile plots of the two dimensional histograms are shown in Fig. 7.14. Only the correlation with sphericity is examined, since correlation plots with thrust deliver no new information. At low sphericity values distributions computed from QCD and SUSY events reveal the same correlation, anticipated in the previous paragraphs: the mean values of the antenna variables rise with increasing sphericity, since increasing sphericity corresponds to better separated leading jets, which lead to larger invariant masses and hence larger values of the antenna variables. The strong rise in the 0 to 0.1 range of sphericity becomes slow increase in the region of larger sphericity values for both distributions. This

Figure 6.32: Distribution of the negative inclusive A_n variable computed from Calo-Jets vs. thrust, for the QCD (**left**) and for the SUSY LM4 sample (**right**). Colour code indicates the number of events.
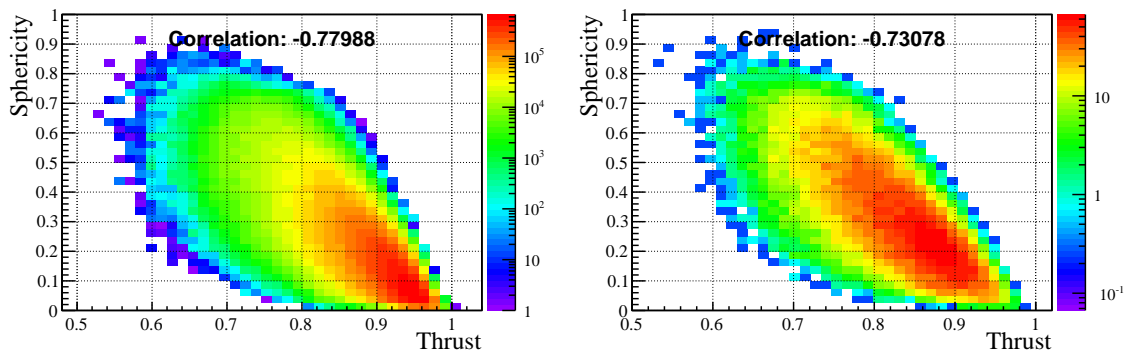
Figure 6.33: Correlation between thrust and sphericity in the QCD events (**left**) and in the SUSY LM4 events (**right**).

increase continues for $\left\langle -A_n^{SUSY} \right\rangle$ up to large sphericity values with low statistics. In the QCD case a new rise begins after the sphericity value of ca. 0.7. The QCD antenna distribution becomes more and more SUSY-like, if only events with large sphericity values are selected. The plots confirm, that the mean values of $-A_n^{QCD}$ and $-A_n^{SUSY}$ distributions are displaced with respect to each other over almost the whole range of sphericity. This displacement approves the discrimination power of the antenna variables independent from the sphericity of the events.

The rise of the negative antenna values computed from QCD events having large sphericity can be understood by examining the distribution of the HT variable across sphericity. Figure 6.35 shows the mean value of the HT distribution in QCD and SUSY events in bins of sphericity. While there is almost no correlation between HT and sphericity for SUSY events, the mean value of HT rises extremely fast for QCD events with high sphericity values. This rise of the HT distribution explains the rise of the antenna distribution, due to the correlation between the values of antenna variables and HT, examined in the following chapter[8] 7.1.1.

The extreme rise of the HT values in spherical QCD events, and the absence of such a rise in SUSY events, can be explained by different origins of jets in SUSY and QCD. The SUSY jets are the end products of the decays of heavy particles and are only loosely correlated to each other. The QCD jets, aside from the two leading jets, arise in most events from gluon radiation. Selecting well separated jets resulting from gluon radiation, one selects automatically high energetic events, since only such events can lead to the gluon radiation under large angles.

In summary, the antenna variables are correlated with the measures of the event shapes, but provide independent discrimination power. The antenna variables can complement the event shape variables providing additional information of the close by aspects of the event. In case of QCD events, the event shape variables are correlated with the HT in the domain of almost spherical events.

Having described some of the characteristics of the antenna variables, they are applied in the next chapter to the cut-based SUSY searches in the all-hadronic channel as an example of use.

---

[8]The larger the HT of the event the lager are the values of the antenna variables, due to larger four products of momenta in the denominators of the antenna structures.
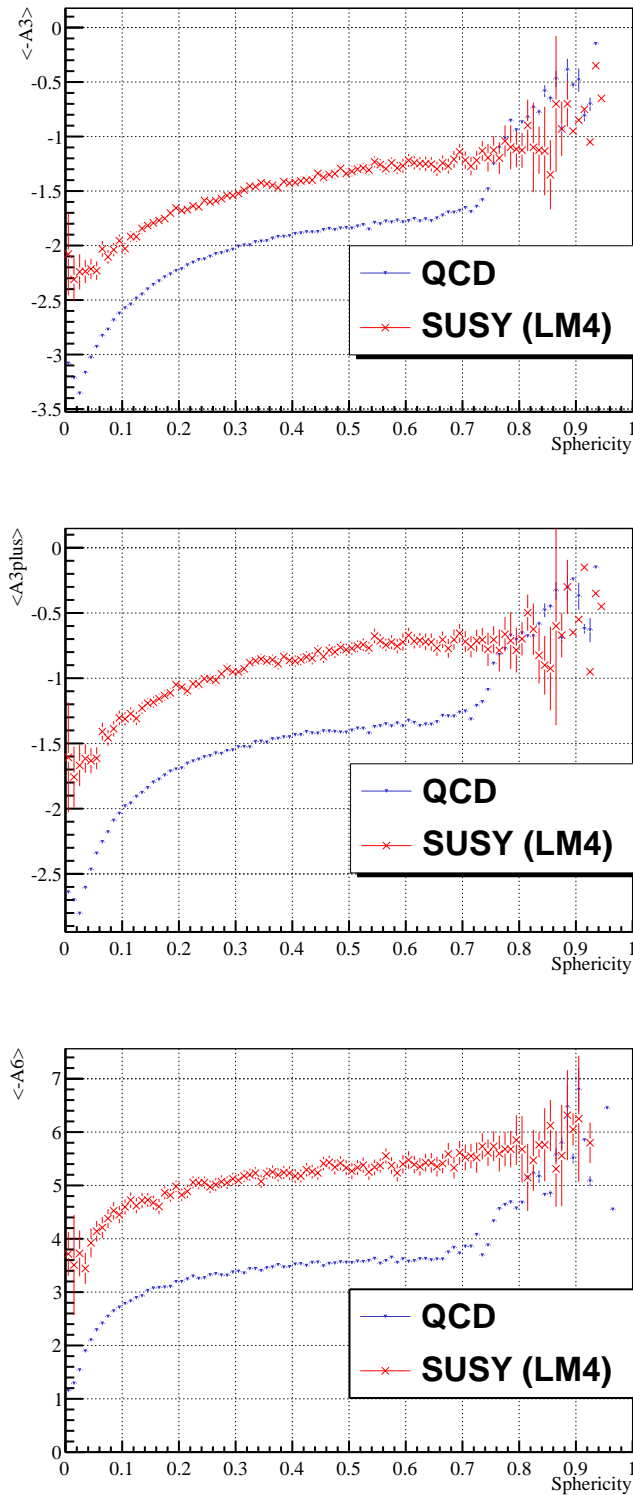
Figure 6.34: Mean values of the $-A_3$, $-A_{3plus}$, and $-A_6$ distributions in each bin of sphericity. Blue lines indicate the entries for the QCD and red lines for the SUSY LM4 sample.
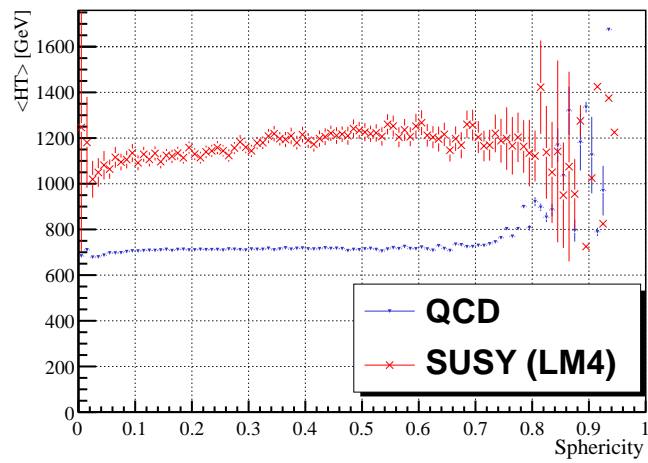
Figure 6.35: Mean value of the *HT* distribution in each bin of sphericity. Blue line indicates the entries for the QCD and red line for the SUSY LM4 sample.

7

Application to SUSY Searches

The antenna variables, defined in the previous chapter, can have a manifold field of application. First of all, one of the variables can be used as an additional discriminative variable in a cut-based search or as an additional input variable in a multivariate search for the signals of physics beyond the standard model in the all-hadronic channel. The sensitivity of the antenna variables to the shape of the events and the invariant masses present therein suggests the use of the antenna variables in a multivariate approach for the determination of the underlying parameters of the possible signal, for example for the identification of the mSUGRA parameters in case of SUSY. Another imaginable example of use could be the data-driven QCD multijet background estimation, provided that one of the antenna variables is uncorrelated to some other kinematic variable with separation power.

The previous chapter showed that the antenna variables are able to distinguish between QCD and SUSY multijet events. In order to assess the feasibility of the antenna variables for SUSY searches, this chapter examines the correlations between commonly used kinematic and antenna variables. First, a rudimentary cut-based analysis is introduced and the impact of successive cuts on various kinematic variables on the discrimination power of the antenna variables is investigated. Then a comparison between the different antenna variables is carried out. In the last step the discrimination power of the most promising antenna variable is studied assuming different SUSY signal scenarios. This chapter will also show that the antenna variables are correlated with other discriminating variables which are used in SUSY searches and are therefore not suited for the data-driven background estimation in this case.

7.1 QCD multijet background reduction

Various studies of possible SUSY searches with the CMS experiment have been done so far [4, 5, 69]. These studies use optimised sequences of cuts on different variables to suppress SM backgrounds and to find the signal.

The approach in the present section is inspired by those studies. Specifically, the present analysis examines the possibility to suppress background from QCD multijet

events. In order to be compatible with the previous studies only inclusive antenna variables (A_3, A_{3plus}, A_6) are used.

7.1.1 Kinematic variables

The following definitions of kinematic variables are used in the present work:

- The missing transverse energy (MET) vector:

$$\text{MET} = -\sum_i (E_i \sin \theta_i)\hat{n}_i, \tag{7.1}$$

  where E_i is the energy of the i-th calorimeter tower, $\hat{n}_i$ is a transverse unit vector pointing to the centre of each tower, and θ_i is the polar angle of the tower.

- Minimum $\delta\phi$ between the MET and the 3 leading jets:

$$\Delta\phi = \min\{\delta\phi_i\}, \tag{7.2}$$
$$\delta\phi_i = \delta\phi(\text{MET}, jet_i). \tag{7.3}$$

  where $\delta\phi_i$ is evaluated for the three leading jets.

As introduced in chapter 5, it is assumed, that the colliding partons inside the protons have negligible intrinsic transverse momenta. Therefore, the transverse momentum of the initial state is taken to be zero. Momentum conservation thus implies that the sum of the transverse momenta of all final states vanishes. In case of a perfect or uniform detector, MET would thus indicate that particles which do not interact, or interact only weakly, with the detector material were created. This study deals only with pure QCD background processes, in which no MET is produced in the hard scattering process. Therefore, assuming a perfect detector, events with MET and many jets could be classified as SUSY event candidates, see chapter 2. However, the detector is not perfect and even pure QCD processes can lead to *fake* MET because of the mismeasurements of the jets and a possible neutrino content. In general SUSY events will contain more MET than QCD events, since primary SUSY particles are heavy and can lead to very large transverse momenta of the lightest supersymmetric particles.

The large fake MET in QCD events is generated mainly by the mismeasurement of energy of the one of the three leading jets. As a result, the fake MET is pulled in ϕ in the direction of the mismeasured jet, which leads to small values of the $\Delta\phi$ variable, contrary to the case of SUSY events, in which there is no special constraint on the real MET direction.

The benchmark studies [4, 5] were based on the cuts on MET and $\Delta\phi$ variables, which are expected to have the largest discrimination power between SUSY and QCD. Figure 7.1 shows the distribution of MET in QCD and SUSY LM4 events. Figure 7.2 shows the distribution of $\Delta\phi$ in QCD and SUSY LM4 events after a cut on MET (MET > 200 GeV) was performed.
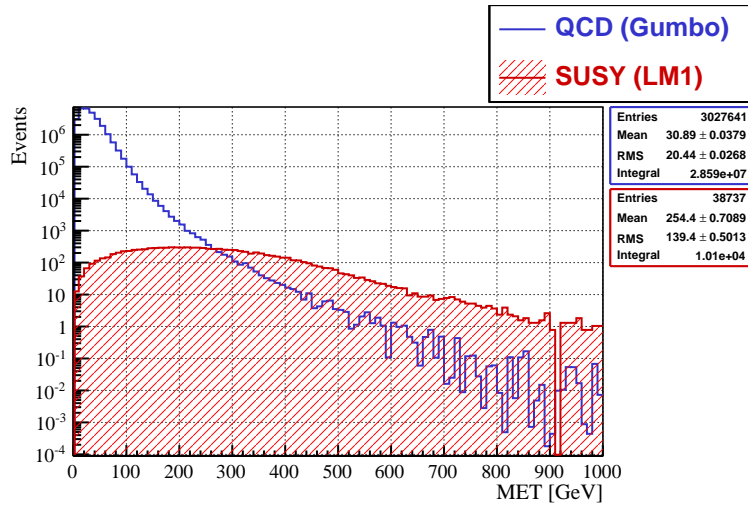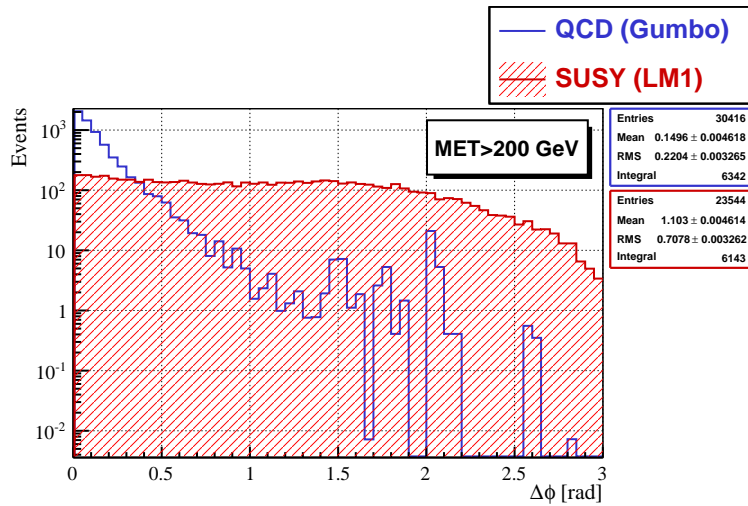
Figure 7.1: Distribution of MET in QCD and SUSY LM4 events.

Figure 7.2: Distribution of $\Delta\phi$ in QCD and SUSY LM4 events after a cut on MET (MET > 200 GeV) was performed.

7.1.2   Impact of kinematic cuts on the antenna variables

Inspired by the studies of possible SUSY searches and the contemporary study of the data driven QCD background estimation [76] following cuts on the kinematic variables were chosen for the present work:

- $E_T^{miss} > 200 \; GeV$

- $\Delta\phi > 0.3 \; rad$

These cuts are applied in addition to the cuts on the p_T, E_T, and η of the jets, defined in the previous chapter.

Figure 7.3 shows the distributions of the A_3, A_{3plus}, A_6 antenna variables after the cut on the MET. Contrary to the plots in the previous chapter, the histograms are not normalised to unit area but show event numbers, assuming an integrated luminosity of $1 \; fb^{-1}$. The distributions of the antenna variables computed from the QCD and SUSY events lie on top of each other. In order to understand this outcome, which is different from the one in the previous chapter, two-dimensional histograms of the antenna variables computed from QCD and SUSY events vs. MET and the corresponding correlations coefficients are shown in Fig. 7.4, Fig. 7.5, and Fig. 7.6. The two-dimensional distributions reveal that SUSY events are uniformly distributed in MET reaching values of almost 1000 GeV, while QCD events mostly lie in the region MET $< 200 \; GeV$. Thus, the cut on MET suppresses most of the QCD background making the event numbers comparable.

After this cut the antenna variables have obviously lost most of their discrimination power, due to the suppression of the QCD events with small values of the antenna variables. This suppression appears in the plots in Fig. 7.3 as a shift of the QCD distributions in the SUSY-like region. The high MET tail of the A_n^{QCD} distributions is classified as SUSY-like by the antenna variables. The antenna variables computed from QCD events are correlated with the MET as it can be seen in the two dimensional correlation plots. These plots confirm also the relative displacement of the QCD and SUSY distributions with respect to the antenna variables. The correlation coefficients indicate, that the antenna variables computed from QCD events are stronger correlated with MET in comparison with the antenna variables computed from SUSY events, which can be considered to be independent of MET. In order to exemplify the correlation, profile histograms of the two dimensional plots from Fig. 7.4, Fig. 7.5, and Fig. 7.6 are shown in Fig. 7.7. The profile histograms reveal the extreme difference between QCD and SUSY events in the dependence of the antenna variables computed from this events on MET. Antenna variables in SUSY events do not depend on MET. All antenna variables computed from QCD events appear to be linearly correlated with MET up to MET $\approx 230 \; GeV$, becoming more and more SUSY-like. It follows, that the MET cut selects only the SUSY-like parts of the QCD antenna distributions.

The origin of such a selection effect lies in the dependence of the antenna variable not only on relative angles between the jets, but also on the energies present in the event. Figure 7.8 shows the profile histogram of the $-A_6$ variable as a function of HT. The larger the HT of the event the larger is the value of both the $-A_6^{QCD}$ and the $-A_6^{SUSY}$ variables, due to larger four momenta products in the denominators of

the antenna structure. However, both curves are displaced, because of the different angular structure (topology) of the QCD and SUSY events. Figure 7.9 shows the HT distribution in the QCD and SUSY samples (only events which entered the $-A_6$ computation having at least 6 jets were selected) before and after the MET cut. The mean value of the HT variable doubles in case of QCD events after the MET cut (from ca. 900 GeV to ca. 1800 GeV), while it stays constant in the case of SUSY events.

The origin of the fake MET in the QCD events are jet energy mismeasurements. The absolute jet energy resolution worsens with the increasing jet energy. In addition punch-through effects[1] occur more frequently if the energy of the jets is large. Therefore, selecting only events with high MET, one selects primarily QCD events with high values of HT as it is illustrated in Fig. 7.9. This selection effect does not affect much the SUSY events, which have real MET. Because of the dependence of $-A6$ and similarly other antenna variables on HT, the demand of a lot of MET in QCD events pushes especially the QCD antenna variables to higher values, while leaving the values of the SUSY antenna variables mostly unchanged.

In the next step the $\Delta\phi$ dependence of the antenna distributions is explored. Figure 7.10 shows the distributions of the antenna variables after MET and $\Delta\phi$ cuts. The impact of the combined $\Delta\phi$ and MET cut is very large, since after both cuts SUSY events dominate in the regions of the low antenna values, while the remaining QCD events populate the high antenna domain. This behaviour is especially pronounced for the $-A_3$ and $-A_{3plus}$ variables. Thus, antenna variables are assumed to be correlated with $\Delta\phi$. Similarly to the MET case, Fig. 7.11 , Fig. 7.12 , and Fig. 7.13 show the two dimensional correlation plots and correlation coefficients. As expected, there is no restriction on values of $\Delta\phi$ for SUSY events, while the values of $\Delta\phi$ in QCD case barely exceed $\Delta\phi \approx 1$. The sign of the correlation coefficients suggest, that A_n^{SUSY} variables are anticorrelated with $\Delta\phi$, while there is a positive correlation in the A_n^{QCD} case. In order to examine this correlation, Fig. 7.14 shows the mean values of the antenna variables computed from QCD and SUSY events in bins of $\Delta\phi$ in the domain of interest.

Firs of all, the plots reveal the correlation between the values of the antenna variables computed from QCD events and $\Delta\phi$ occurring in the region $0 < \Delta\phi < 0.5$. This correlation is important, since a cut in this domain is usually performed to find the signal. The QCD antenna variables become more and more SUSY-like with the increasing$\Delta\phi$. Almost no correlation between the values of the antenna variables and $\Delta\phi$ can be seen in the case of SUSY events. The anticorrelation seen in the two dimensional plots kicks in for very large values of $\Delta\phi$ ($\Delta\phi \approx 1.5$), as it can be seen in the Fig. 7.15 showing the mean value of the $-A_3^{SUSY}$ variable in bins of $\Delta\phi$.

While the cut on MET selects mainly the high energetic QCD events, the $\Delta\phi$ cut rejects events with particular angular structure. Since the origin of the fake MET in QCD are jet energy mismeasurements, and the previous MET cut has selected only events having large fake MET, the $\Delta\phi$ cut rejects almost all three jet events, in particular the three jet events with pencil-like structures, because in such cases MET will almost always point in the direction of the one of the jets. But precisely

---

[1] If a high energetic jet penetrates the whole calorimeter and deposits a part of its energy outside, one is speaking of a punch-through effect.

these events are responsible for the low values of the antenna variables. Furthermore, all events, in which all but the high energetic jets are close to each other will be preferentially rejected, due to the topology of their four momenta. This selection effect leads to the observed correlation and to the apparent transposition of the signal-like and the background-like regions.

The impact of the $\Delta\phi$ cut on the number of jets can be seen in Fig. 7.16, which supports the explanation given above, showing strong suppression of the 3-jet and other low jet multiplicity QCD events after the $\Delta\phi$ cut.

The origin of the anticorrelation between the antenna variables computed from SUSY events and $\Delta\phi$ variable occuring at very high values of $\Delta\phi$ ($\Delta\phi > 1.5$[2]) after the MET cut, lies in the selection of the events where the three leading jets are forced to lie in a small region of the detector (approximately one half plane). This region becomes ever smaller with the higher cut. Such events tend to have small values of the antenna variables, due to small angular separation of the leading jets. This effect is especially strong for the events with exact three jets and is reduced for the events with higher jet multiplicity, since no restriction is imposed on the additional jets.

In summary, the antenna variables are highly correlated with the MET and the $\Delta\phi$ variable. These correlations lead to the fact, that the signal— and background— regions of the antenna variables change places. The domains of low antenna values are populated after both cuts by almost pure SUSY events. Because of this behaviour, the cuts on other discriminating variables have to be performed before the cut on the antenna variable. The usefulness of the cuts on the antenna variables after previous cuts on MET and $\Delta\phi$ is inspected in the next section.

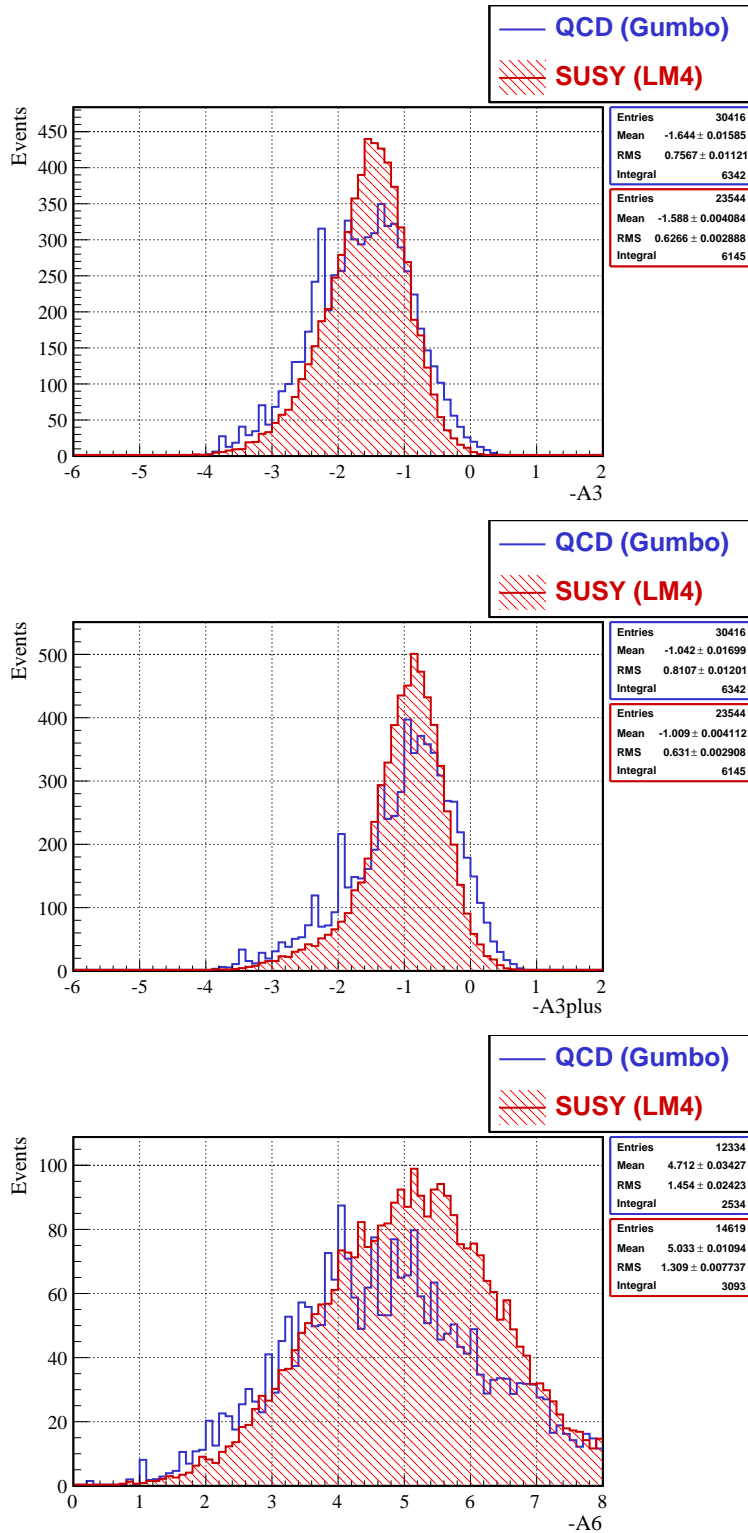[2]In this region there are no QCD events

Figure 7.3: Distributions of the negative A_3, A_{3plus} and A_6 variables computed from CaloJets for the QCD and SUSY LM4 sample after the cut on MET (MET>200 GeV).
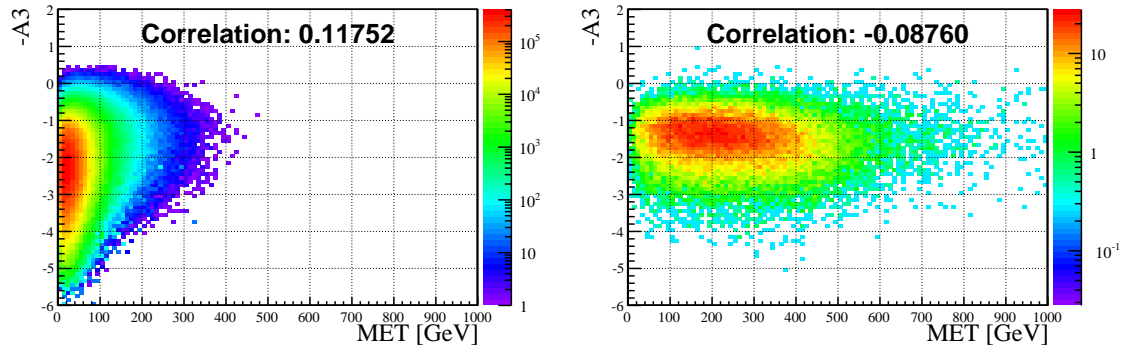
Figure 7.4: Distribution of the negative A_3 variable computed from CaloJets vs. MET, for the QCD (**left**) and for the SUSY LM4 sample (**right**). Colour code indicates the number of events.
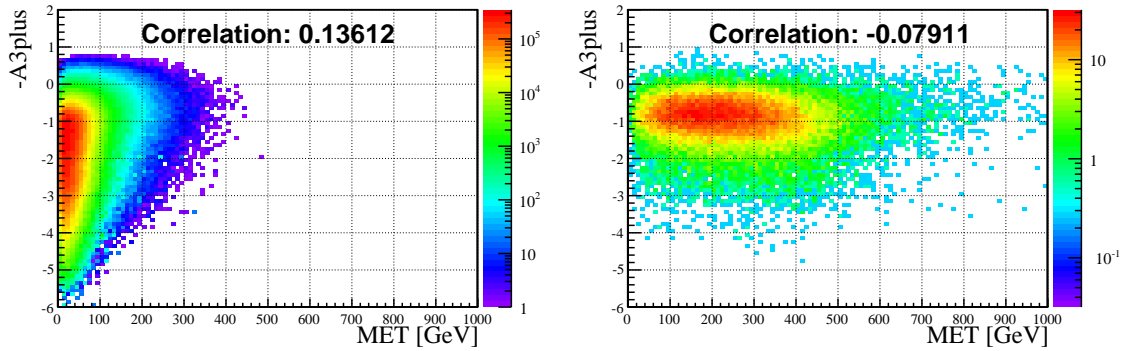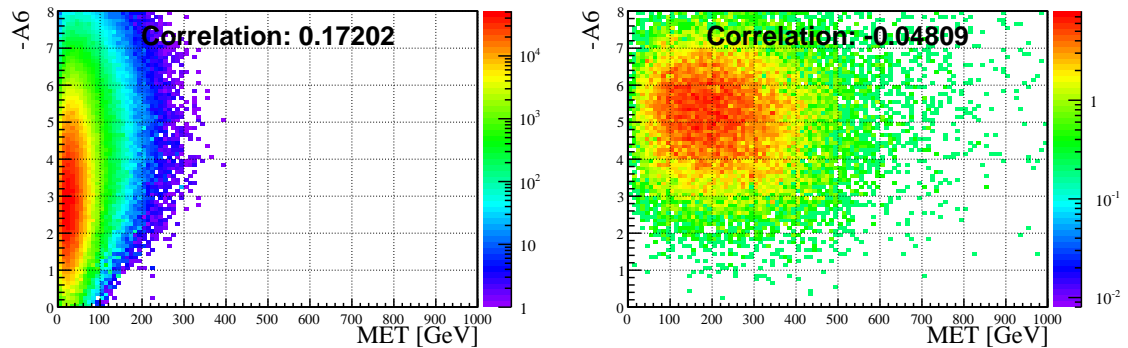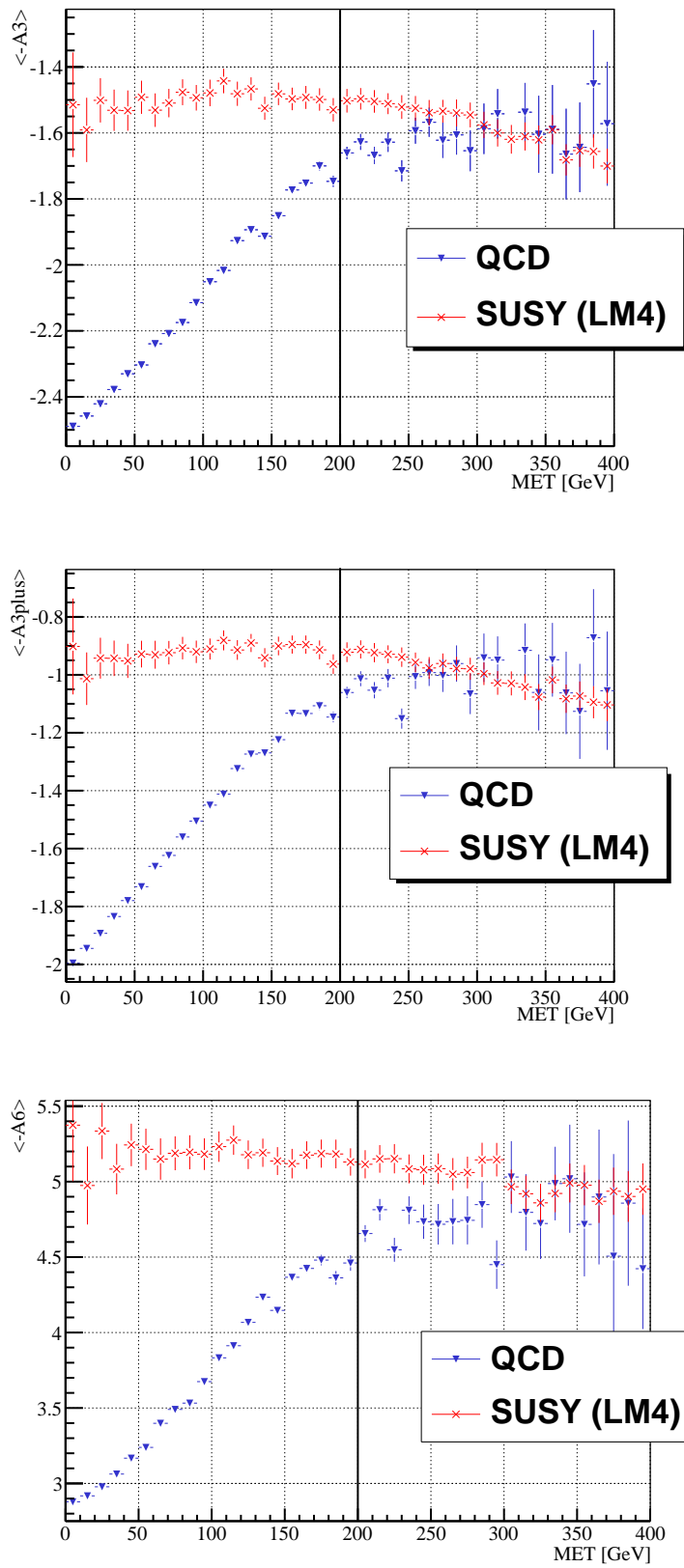

Figure 7.5: Distribution of the negative A_{3plus} variable computed from CaloJets vs. MET, for the QCD (**left**) and for the SUSY LM4 sample (**right**). Colour code indicates the number of events.

Figure 7.6: Distribution of the negative A_6 variable computed from CaloJets vs. MET, for the QCD (**left**) and for the SUSY LM4 sample (**right**). Colour code indicates the number of events.

Figure 7.7: Mean values of the $-A_3$, $-A_{3plus}$, and $-A_6$ distributions in each bin of MET. Blue lines indicate the entries for the QCD and red lines for the SUSY LM4 sample. The black vertical line indicates the MET cut.
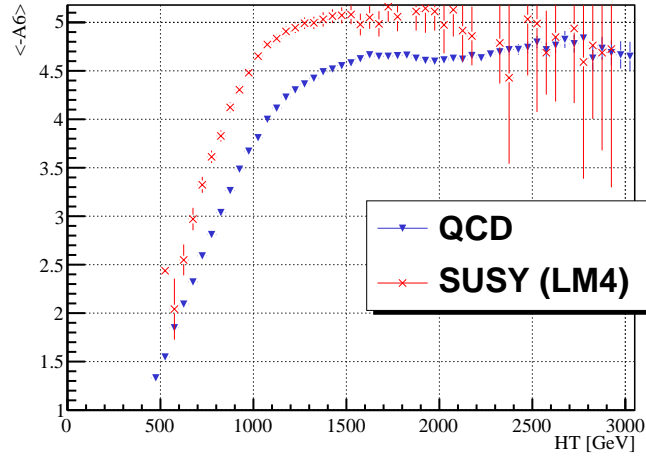
Figure 7.8: Mean values of the A_6 distribution in each bin of HT. Blue lines indicate the entries for the QCD and red lines for the SUSY LM4 sample.
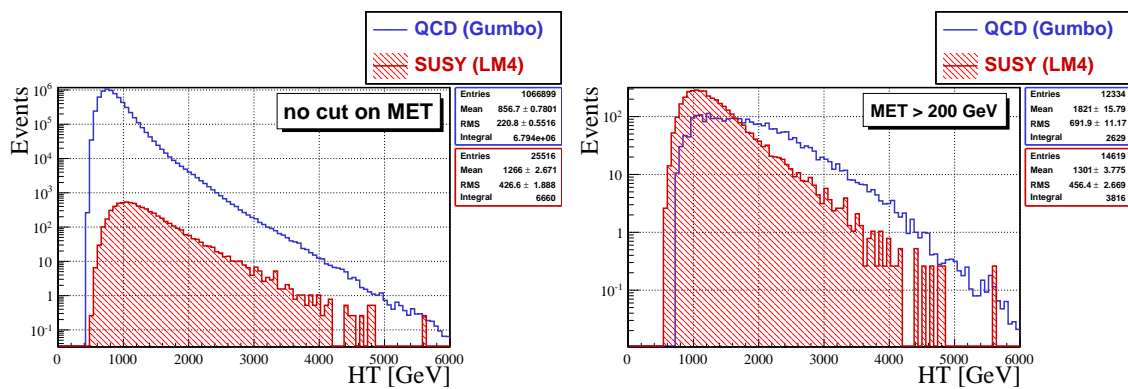

Figure 7.9: Distribution of the HT variable in QCD (blue line) and SUSY (red line) events having at least 6 jets before (**left**) and after (**right**) the MET cut.
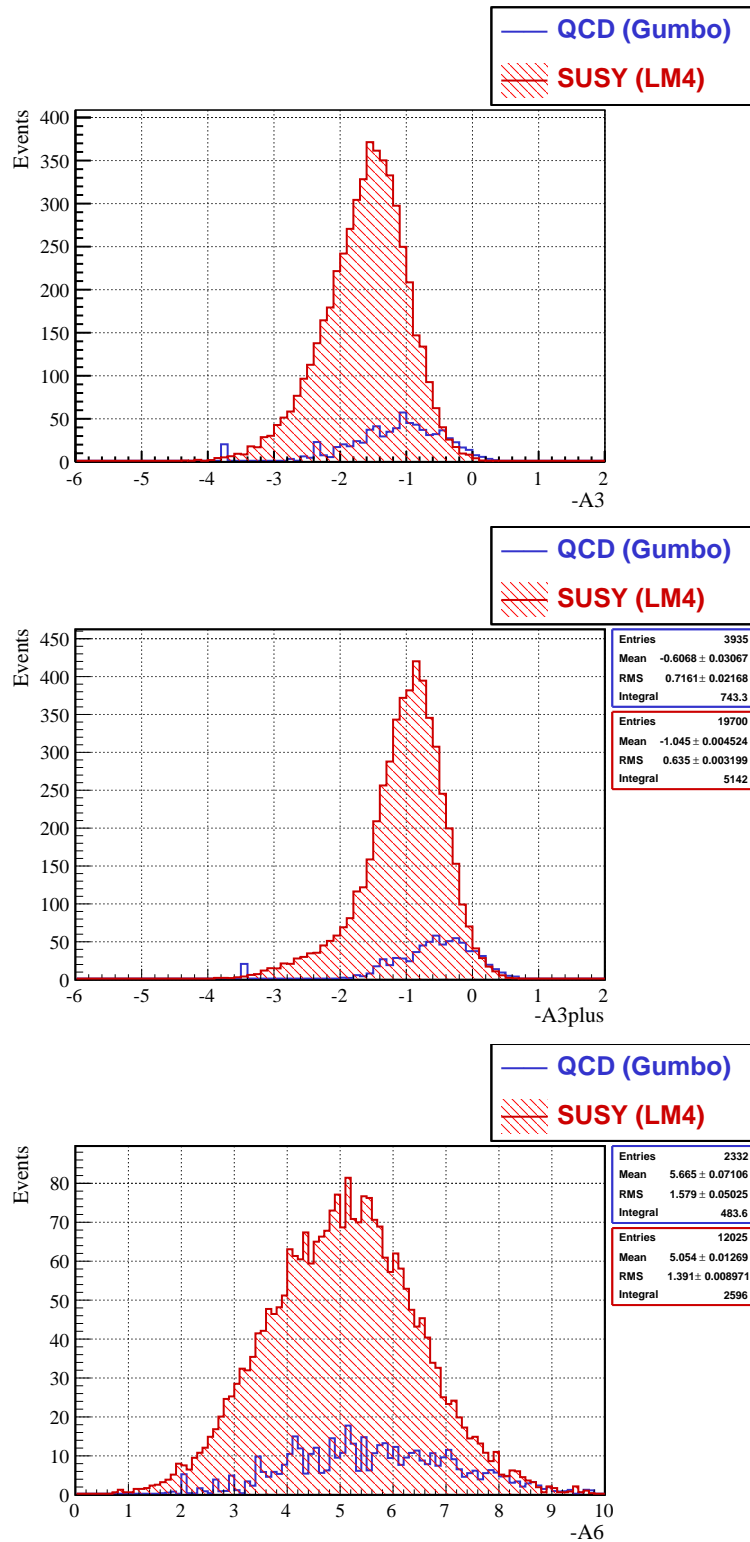
Figure 7.10: Distributions of the negative A_3, A_{3plus} and A_6 variables computed from CaloJets for the QCD and SUSY LM4 samples after the cut on MET (MET>200 GeV) and $\Delta\phi$ ($\Delta\phi > 0.3\ rad$).
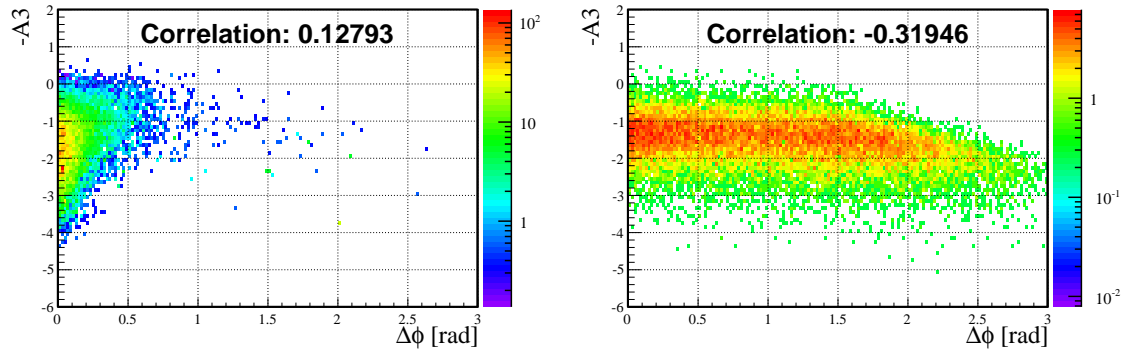
Figure 7.11: Distribution of the negative A_3 variable computed from CaloJets vs. $\Delta\phi$, for the QCD (**left**) and for the SUSY LM4 sample (**right**). Colour code indicates the number of events.
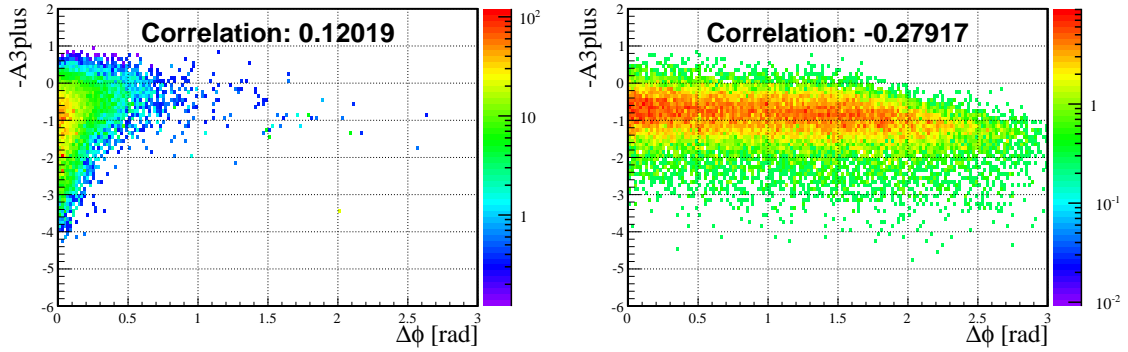

Figure 7.12: Distribution of the negative A_{3plus} variable computed from CaloJets vs. $\Delta\phi$, for the QCD (**left**) and for the SUSY LM4 sample (**right**). Colour code indicates the number of events.

Figure 7.13: Distribution of the negative A_6 variable computed from CaloJets vs. $\Delta\phi$, for the QCD (**left**) and for the SUSY LM4 sample (**right**). Colour code indicates the number of events.
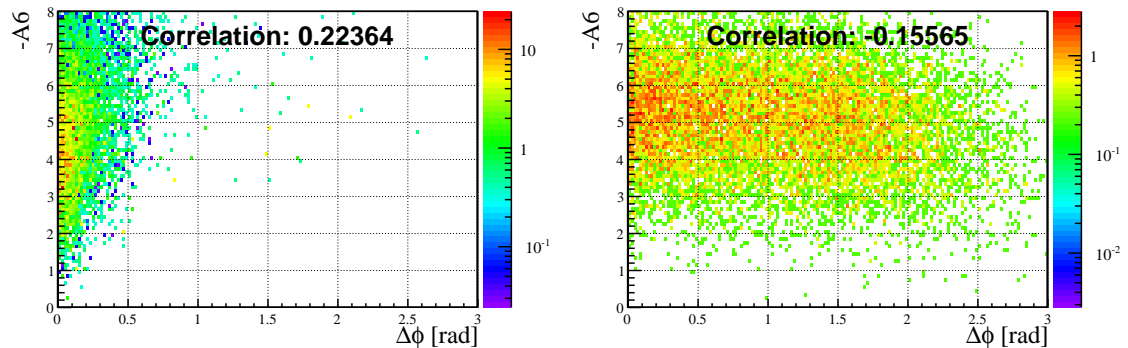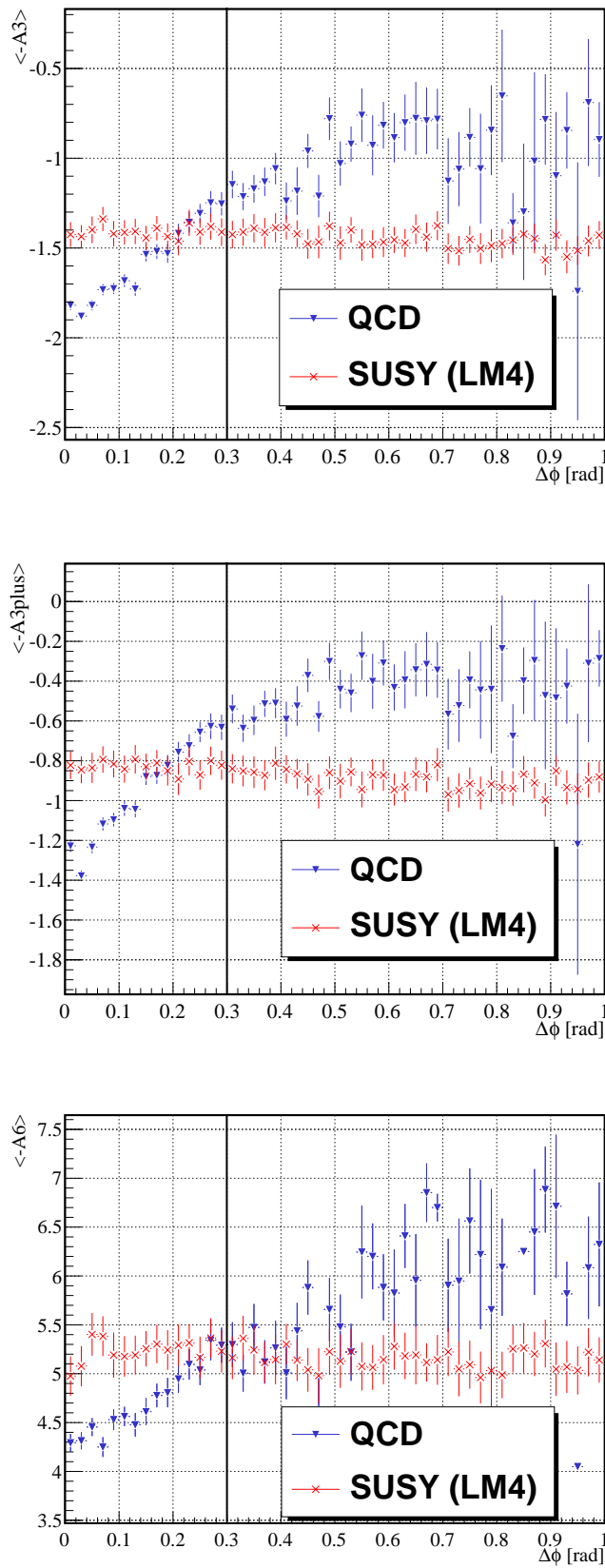
Figure 7.14: Mean values of the $-A_3$, $-A_{3plus}$, and $-A_6$ distributions in each bin of $\Delta\phi$. Blue lines indicate the entries for the QCD and red lines for the SUSY LM4 sample. The black vertical line indicates the $\Delta\phi$ cut.
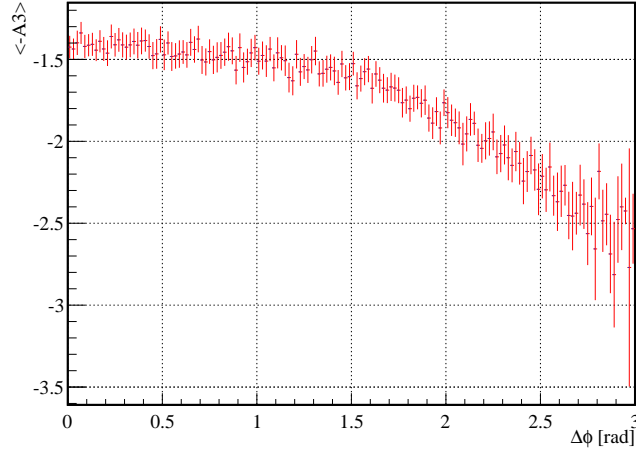
Figure 7.15: Mean value of the $-A_3^{SUSY}$ variable in bins of $\Delta\phi$.
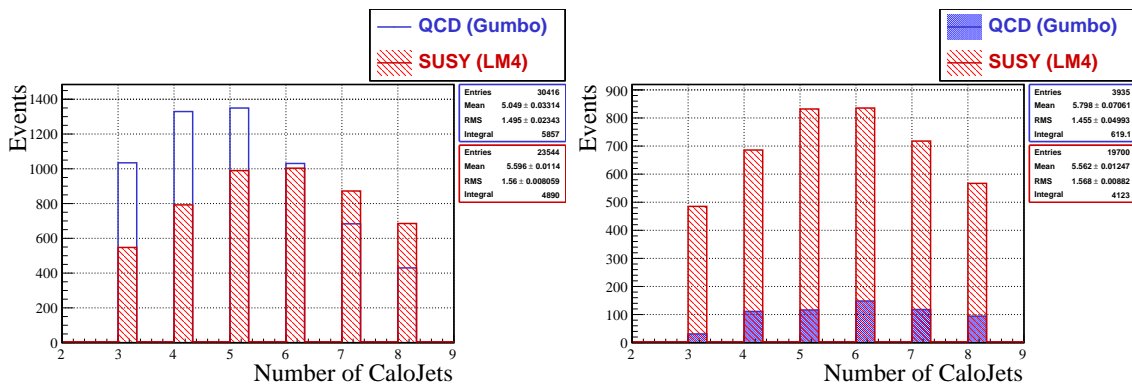

Figure 7.16: Jet multiplicity distributions in QCD and SUSY events after the MET cut **left plot**, and after both MET and $\Delta\phi$ cuts **right plot**.

7.2 Comparison of the antenna variables

Assuming that the effect of the vanishing QCD population in the high antenna regions is truly physical, cuts on the antenna variables can be defined, and the discrimination power of the different variables can be compared. The signal sample is SUSY LM4, cf. chapter 2. The following variables were chosen to compare the quality of the variables:

- The ratio Q of the signal to background ratios after and before the cut on the antenna variable

$$Q = \frac{(Signal/Background)_{\text{after the cut}}}{(Signal/Background)_{\text{before the cut}}} \quad (7.4)$$

- The ratio S of the significances after and before the cut on the antenna variable

$$S = \frac{(Signal/\sqrt{Background})_{\text{after the cut}}}{(Signal/\sqrt{Background})_{\text{before the cut}}} \quad (7.5)$$

The ratio Q is important if one is dominated by the systematic errors, in which case it is important to maximise the signal to background ratio . The variable S is important if the statistical errors dominate, and it is crucial to improve the significance. The results of the comparison of the $\Delta\phi$, $-A_3$ and $-A_{3plus}$ variables, as well as their threshold values are summarised in the Tab. 7.1. The $-A_6$ variable has to be treated separately, since it requires at least 6 jets and the result for this variable is given in Tab.7.2. The events have to have the values of the antenna variables below the threshold values, in order to be selected. These threshold values were determined, after several test-cuts, by choosing the cut value which maximised the ratio S.

All antenna variables improve the signal to background ratio by up to a factor of 2.1. The A_3 and A_{3plus} variables hold the significance $(Signal/\sqrt{Background})$ constant, while it drops after the cut on A_6 to 0.7. Hence the cut on the A_6 variable is not useful if one is dominated by the statistical errors. In summary the A_{3plus} variable performs best closely followed by the A_3 variable. As a comparison the values of the Q and S variable are also given for $\Delta\phi$, which performs much better as the antenna variables, improving not only the signal to background ratio but also the significance.

	MET > 200	$\Delta\phi > 0.3$	$-A_3 < -1.5$	$-A_{3plus} < -1$
N^{QCD}	6342	743	182	168
N^{SUSY}	6145	5142	2374	2416
Q	-	7.1	1.9	2.1
S	-	2.4	0.9	1

Table 7.1: Comparison of the discrimination power of the antenna variables A_3 and A_{3plus}. The cut on MET is given in GeV, while the cut on $\Delta\phi$ is given in rad. N^{QCD} and N^{SUSY} are the numbers of the background and signal events after the corresponding cut. The cuts on MET and $\Delta\phi$ are applied sequentially. The cut on only one antenna variable is performed at a time, but always on top of the MET and $\Delta\phi$ cuts.

	MET > 200	$\Delta\phi$ > 0.3	A_6 < 4
N^{QCD}	2534	484	86
N^{SUSY}	3093	2596	760
Q	-	4.4	1.6
S	-	1.9	0.7

Table 7.2: Comparison of the discrimination power of the antenna variable A_6. The cut on MET is given in GeV, while the cut on $\Delta\phi$ is given in rad. N^{QCD} and N^{SUSY} are the numbers of the background and signal events after the corresponding cut. The cuts on MET and $\Delta\phi$ are applied sequentially. The cut on A_6 is performed on top of the MET and $\Delta\phi$ cuts.

	LM1	LM4	LM8	HM3
N^{SUSY}_{before}	9756	5142	2174	19
N^{SUSY}_{after}	5536	2416	829	5
Q	4.4	2.1	1.7	1.2
S	2.1	1	0.8	0.6

Table 7.3: Comparison of the discrimination power of the antenna variable A_{3plus} assuming different signal scenarios but using the same threshold value. The cuts on MET and $\Delta\phi$ were applied beforehand.

However, $\Delta\phi$ is expected to be the second best variable after MET, and it is difficult to find variables having additional separation power. The discrimination power of the antenna variables can be further optimised by scanning over possible cut values to find the optimal working point. Additionally antenna variables can be used as an additional input for a multivariate approach.

7.2.1 Discrimination power in dependence on the SUSY parameters

The cuts on antenna variables were optimised assuming the SUSY LM4 signal scenario. In this subsection the performance of the A_{3plus} variable, which performed best in the previous comparison, is tested on different SUSY mSUGRA test points. The cuts are performed with the constant cut value of -1 simulating a scenario independent search. The cuts on the kinematic variables (MET and $\Delta\phi$) were performed beforehand. The effect of these cuts on QCD events can be read out from the Tab. 7.1:

- $N^{QCD}_{before} = 743$

- $N^{QCD}_{after} = 168$

Table 7.3 summarises the results of the comparison for the different SUSY test points. The effect of the cut on the A_{3plus} variable depends on the SUSY scenario under consideration. The performance of the variable worsens with increasing mass of the SUSY particles contrary to the situation before the MET and $\Delta\phi$ cuts, since higher SUSY masses shift the distributions of the $-A_n^{SUSY}$ variables in the domain of large antenna values containing, after the kinematic cuts, the bulk of the QCD

distribution. However, the variable improves the signal to background ratio for all scenarios holding the significance constant or even improving it at the mSUGRA LM1 test point. At this point the signal to background ratio can be quadrupled while the significance can be doubled. The significance worsens only for the high mass point reaching 0.6, which should be taken into account if the antenna variables are used for a scenario independent searches.

Theoretical, it would be possible to optimise the antenna cut values, in the case where the antenna variables are used for SUSY search at a particular test point. Fig. 7.17 shows the distributions of the antenna variables computed from QCD- and SUSY events at different test points after the cuts on the kinematic variables (MET and $\Delta\phi$). The numbers of events and the shapes of the distributions reflect the falling cross sections of SUSY test points (9756 LM1 events compared to 2174 LM4 events or even 19 HM3 events) and the shift to larger antenna values (-1.18 for LM1 vs. -0.69 for HM3), mentioned above. These plots suggest and test cut results confirmed, that the cut value of -1 chosen for a inclusive search is also a reasonable cut for the searches at the particular signal point. This result suggests that the A_{3plus} variable should not be used for the SUSY searches at high mass points.

The A_6 variable performed worst in the discriminator test in the previous section, due to the approximate uniform distribution of the variable values for QCD events. However, the A_6 variable incorporates the most information on the close-by structure of the events, as stated in the section 6.9. Therefore, the shape of the distribution of this variable could be probably used to discriminate between the different possible SUSY signals. Figure 7.18 shows the distributions of the $-A_6$ variable computed from QCD, SUSY LM1, SUSY LM4, and SUSY HM3 events. Figure 7.19 shows the same distributions normalised to the unit area and on a linear scale, in order to exemplify the different shapes. The mean of the $-A_6^{SUSY}$ distributions tends to larger values with increasing masses of the SUSY particles. Additionally the distributions computed from QCD and different SUSY test points have different shapes. The $-A_6^{QCD}$ distribution falls rapidly for small antenna values, while it decreases at a slower rate towards high values. The shapes of the $-A_6^{SUSY}$ distributions are different for each point. This behaviour of the $-A_6$ variable suggests their use in a multivariate approach in order to estimate the parameters of the SUSY signal.

In summary, the antenna variables offer additional discrimination power for the all-hadronic SUSY searches, in particular at the low mass points, provided, that the extinction of the QCD population in the low antenna regions after combined MET and $\Delta\phi$ cuts can be confirmed by further studies with different event generators. The deployment of the A_6 variable as an additional input in a multivariate estimation of the SUSY parameters should be investigated in further studies. The correlations of the antenna variables with all kinematic variables discussed so far, impede the use of the antenna variables in a data-driven background estimation method.
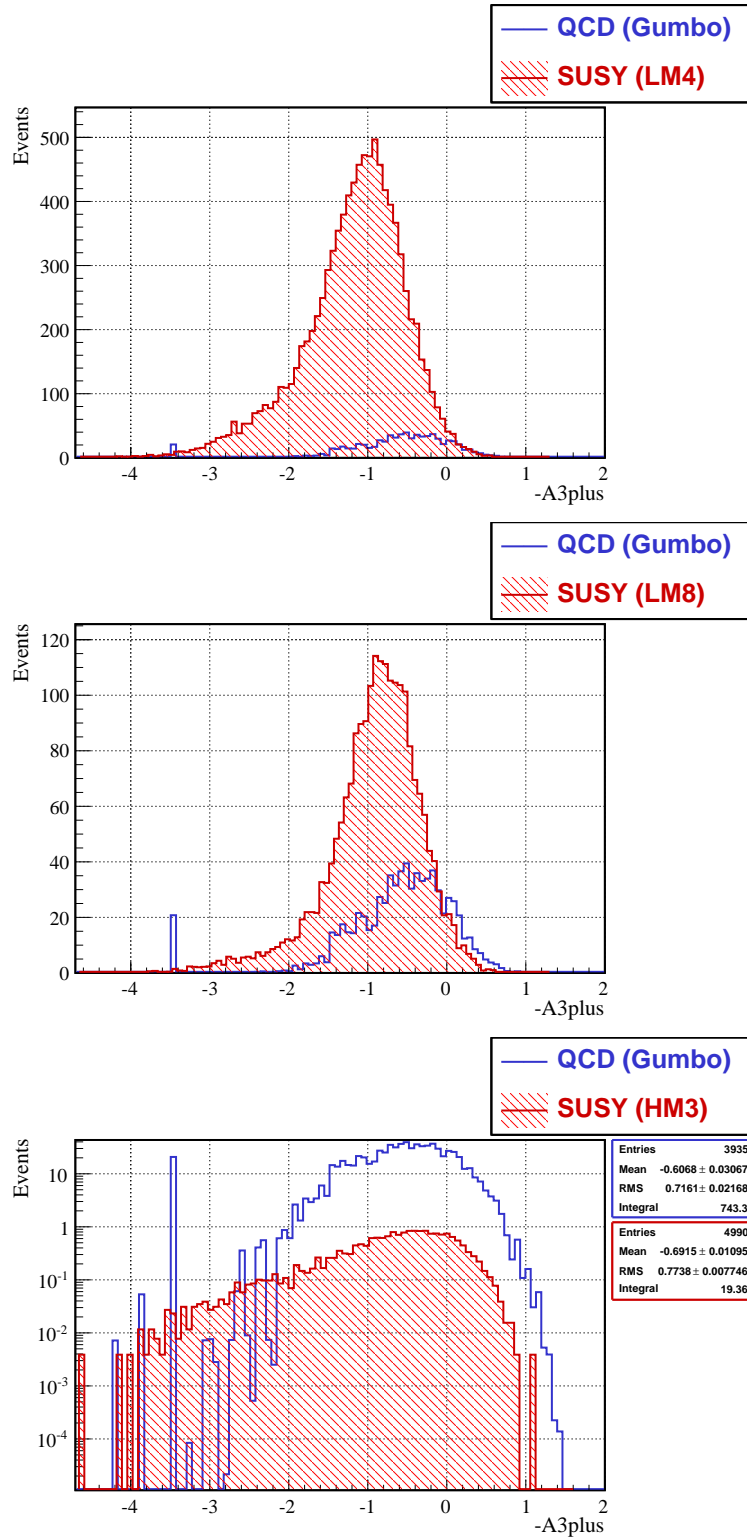
Figure 7.17: Distributions of the negative A_{3plus} variable in QCD and SUSY LM1, LM8 and HM3 datasets. The cuts on MET (MET>200 GeV) and $\Delta\phi$ ($\Delta\phi > 0.3\ rad$) were applied beforehand.
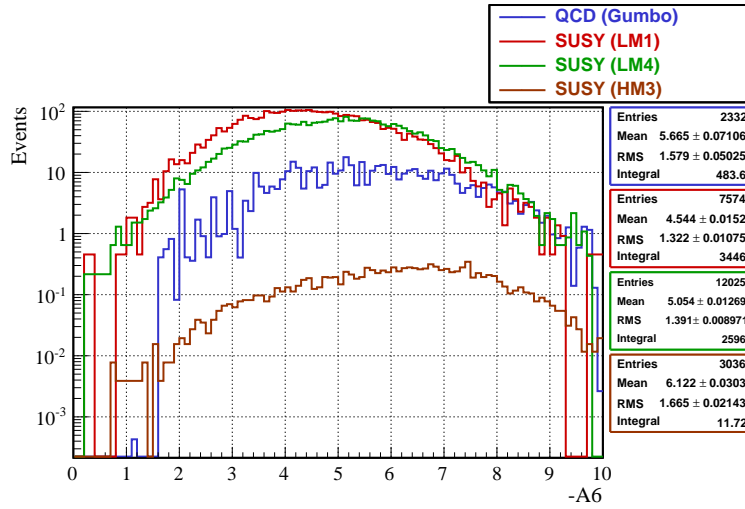
Figure 7.18: Distributions of the negative A_6 variable in QCD and SUSY LM1, LM4 and HM3 datasets. The cuts on MET (MET>200 GeV) and $\Delta\phi$ ($\Delta\phi > 0.3\ rad$) were applied beforehand.
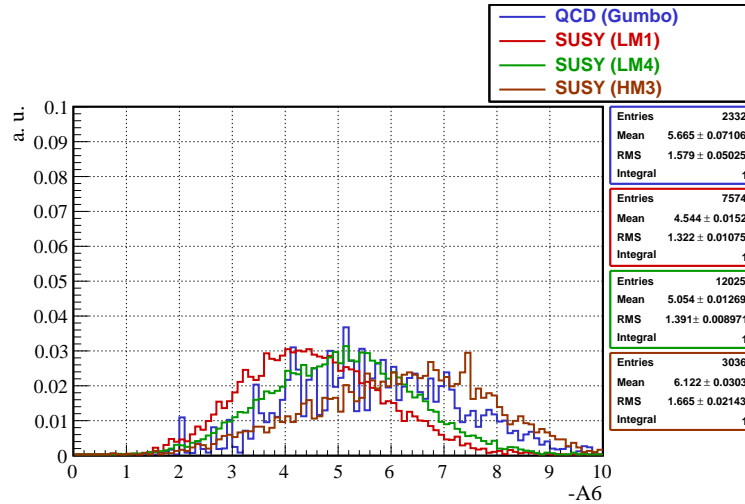

Figure 7.19: Normalised distributions of the negative A_6 variable in QCD and SUSY LM1, LM4 and HM3 datasets. The cuts on MET (MET>200 GeV) and $\Delta\phi$ ($\Delta\phi > 0.3\ rad$) were applied beforehand.

8

Conclusion and Outlook

The main purpose of this thesis has been the investigation of QCD-antenna inspired variables, which could be used as additional discriminators for the all-hadronic searches of physics beyond the standard model, as it was shown using the example of R-parity conserving SUSY.

QCD-antennas are special patterns of the four momenta products in QCD scattering amplitudes. The so called antenna variables introduced in the present work are observables build on the structure of the gluon scattering QCD-antenna. The antenna variables can be divided in two groups. Exclusive variables use all jets present in the event and can be interpreted, if applied to QCD events, as crude approximation to the tree-level gluonic amplitude, which would lead to the particular, observed jet structure. However, the definition of the exact jet number is fragile and depends much on the applied cuts, the jet algorithm, and detector response. Inclusive antenna variables use only the n leading jets of each event for the computation and lead to the best results.

In general the observables (inclusive and exclusive) are measures of the averaged inverse invariant mass of jet pairs present in the event. The discrimination power of the observables originates from their sensitivity to the topology of the jets from which they are constructed. The QCD events have in general more close-by jets originating mostly from gluon radiation, while jets from the cascade decay of heavy particles are in general better separated thus leading to larger invariant masses and hence to larger values of the observables.

This work shows that the construction of such observables is possible. Furthermore, the behaviour of the simplest observable in the case of $gg \rightarrow gg$ scattering on parton level is shown to follow closely the theoretical predictions.

The present study applies the antenna variables to the case of the mSUGRA SUSY model with R-parity conservation as signal. The variables computed from simulated jets show the expected discrimination power between QCD and SUSY events. The discrimination power depends on the SUSY scenario under consideration. Without additional cuts, the discrimination power of the variables increases with increasing

masses of the primary SUSY particles. The antenna variables can also be constructed on the detector level showing comparable behaviour to the variables on the Monte Carlo level, with good resolution if the number of hadron jets and detector jets is the same.

The antenna variables can be related to the event shape variables like thrust and sphericity. In contrast to the event shape variables, which are mainly sensitive to the jets with the largest momenta, the antenna variables offer additional sensitivity to the close-by structure of the jets.

The behaviour of the antenna variables changes if cuts on other kinematic variables are applied beforehand. The cut on missing transverse energy, which is essential for the reduction of the number of QCD events, favours the QCD events containing mostly high energetic jets, while leaving the composition of SUSY events mostly unchanged. The remaining high-energetic QCD events have SUSY-like values of the antenna variables. The additional cut on the minimal angle between missing transverse energy and the three leading jets rejects mostly all QCD events with pencil-like structure. As a consequence of these two cuts the QCD-dominated and SUSY-dominated regions of the antenna distribution change places.

After the swap of the QCD- and SUSY-like regions, cuts on the antenna variables can be carried out. The $-A_{3plus}$ variable constructed out of two leading jets and an additional object, the vector sum of all other jets in the event, performed best. Assuming that the signal would be described by the SUSY LM1 test point, the cut on the $-A_{3plus}$ variable could improve the signal to background ratio by a factor of 4 and double the significance. The $-A_{3plus}$ variable can be also used for the improvement of the signal to background ratios at all low-mass SUSY points. In summary, the present thesis examined new variables, which are able to discriminate between QCD and SUSY events and are only weakly correlated to the event shape variables.

A possible extension of this work would be to use one of the antenna variables as an additional input to a multivariate approach for the QCD background reduction not only for SUSY but also for various different searches of the physics beyond the standard model. The possible use of the variable for searches of the signals without MET should be also further investigated. Additionally, the variable constructed out of the first six leading jets is very sensitive to the close-by angular structure of the events. A further study could investigate the feasibility of the distinction between different SUSY scenarios or other signals using this variable among other things. Moreover the impact of the jet algorithm on the number of detector jets in each event should be investigated. It could be probably possible to make the jet number a more robust variable by using another jet algorithm or by varying the parameters of the k_t jet finder.

A possible limitation of the present study is the deployment of the QCD events generated with the Pythia Monte Carlo generator, which uses only $2 \rightarrow 2$ hard scattering matrix elements and creates additional jets by parton showers. To overcome this obstacle the study should be redone with different QCD samples generated with a Monte Carlo generator using different parton shower techniques, like HERWIG, and a Monte Carlo generator using matrix elements of more complex scattering processes, like MadGraph.

Bibliography

[1] L. Smolin, "A crisis in fundamental physics," *NYAS magazine* (2006) .

[2] B. Schroer, "String theory and the crisis in particle physics,"
`arXiv:physics/0603112`.

[3] H. Baer and X. Tata, *Weak scale supersymmetry: From superfields to scattering events.* Cambridge, UK: Univ. Pr. (2006) 537 p.

[4] **CMS** Collaboration, G. L. Bayatian *et al.*, "CMS technical design report, volume II: Physics performance," *J. Phys.* **G34** (2007) 995–1579.

[5] J. Thomsen, "Search for supersymmetric particles based on large missing transverse energy and high pt jets at the CMS experiment." November, 2007.

[6] K. Fredenhagen, "Quantenfeldtheorie I."
http://unith.desy.de/research/aqft/lecture_notes/.

[7] D. L. Fraser, *Haag's theorem and the interpretation of quantum field theories with interactions.* PhD thesis, University of Pittsburgh, 2006.
http://etd.library.pitt.edu/ETD/available/etd-07042006-134120/unrestricted/
D_Fraser_2006.pdf.

[8] G. Roepstorff, "Einführung in die Quantenfeldtheorie," 2000.
http://www.physik.rwth-aachen.de/fileadmin/user_upload/www_physik/
Bibliothek/Skripte/Roepstorff/qft-2000.pdf.

[9] K. Fredenhagen, K.-H. Rehren, and E. Seiler, "Quantum field theory: Where we are," *Lect.NotesPhys.* **721:61-87,2007** (Lect.NotesPhys.721:61-87,2007) ,
`hep-th/0603155`.

[10] D. Buchholz and R. Haag, "The quest for understanding in relativistic quantum physics," *J.Math.Phys.* **41** (2000) 3674–3697, `hep-th/9910243`.

[11] M. E. Peskin and D. V. Schroeder, *An Introduction to quantum field theory.* Westview Press, 1995.

[12] S. Weinberg, *The Quantum theory of fields volume I : Foundations.* Cambridge University Press, 2005.

[13] R. P. Feynman, "Space-time approach to quantum electrodynamics," *Phys. Rev.* **76** (1949) 769–789.

[14] E. C. G. Sudarshan and R. E. Marshak, "Chirality invariance and the universal Fermi interaction," *Phys. Rev.* **109** (1958) 1860–1860.

[15] S. Weinberg, "The making of the standard model," *Eur.Phys.J. C* **34** (2004) 5–13, `hep-ph/0401010`.

[16] G. 't Hooft, "The conceptual basis of quantum field theory." www.phys.uu.nl/~thooft/lectures/basisqft.pdf.

[17] J. Glimm and A. M. Jaffe, "A lambda (phi**4) quantum field theory without cutoff: 1," *Phys. Rev.* **176** (1968) 1945–1951.

[18] J. Glimm and A. Jaffe, "A lambda (phi**4) in two-dimensions. Quantum field theory without cutoffs: 2,".

[19] J. Glimm and A. Jaffe, "The lambda (phi**4) in two-dimensions. Quantum field theory without cutoffs: 3. The physical vacuum,".

[20] L. D. Landau and E. M. Lifshitz, *The classical theory of fields.* Butterworth Heinemann, 1987.

[21] P. W. Higgs, "Broken symmetries and the masses of gauge bosons," *Phys. Rev. Lett.* **13** (1964) 508–509.

[22] P. W. Higgs, "Broken symmetries, massless particles and gauge fields," *Phys. Lett.* **12** (1964) 132–133.

[23] J. Goldstone, "Field theories with superconductor solutions," *Nuovo Cim.* **19** (1961) 154–164.

[24] G. Altarelli, "A qcd primer," `arXiv:0204179 [hep-ph]`.

[25] R. Ellis, W. J. Stirling, and B. Webber, *QCD and collider physics*, vol. 8 of *Cambridge Monographs on Particle Physics, Nuclear Physics and Cosmology.* Cambridge University Press, 2003.

[26] A. Smilga, *Lectures on quantum chromodynamics.* World Scientific Press, 2001.

[27] J. G. M. Kuijf, *Multiparton production at hadron colliders.* PhD thesis, Universiteit Leiden, 1991.

[28] F. Zwicky, "Die Rotverschiebung von extragalaktischen Nebeln," *Helvetica Physica Acta* **6** (1933) 110–127.

[29] C. Quigg, "The coming revolutions in particle physics," November, 2008. http://lutece.fnal.gov/Talks/CQHelmholtzTerascale.pdf. Talk given at the 2nd Annual Workshop of the Physics at the Terascale Helmholtz Alliance.

[30] Y. A. Golfand and E. P. Likhtman, "Extension of the algebra of poincare group generators and violation of p invariance," *JETP Lett.* **13** (1971) 323–326.

[31] D. V. Volkov and V. P. Akulov, "Possible universal neutrino interaction," *JETP Lett.* **16** (1972) 438–440.

[32] J. Wess and B. Zumino, "Supergauge transformations in four-dimensions," *Nucl. Phys.* **B70** (1974) 39–50.

[33] A. Neveu and J. H. Schwarz, "Factorizable dual model of pions," *Nucl. Phys.* **B31** (1971) 86–112.

[34] P. Ramond, "Dual theory for free fermions," *Phys. Rev.* **D3** (1971) 2415–2418.

[35] S. Dimopoulos and H. Georgi, "Softly broken supersymmetry and SU(5)," *Nucl. Phys.* **B193** (1981) 150.

[36] U. Amaldi, W. de Boer, and H. Furstenau, "Comparison of grand unified theories with electroweak and strong coupling constants measured at LEP," *Phys. Lett.* **B260** (1991) 447–455.

[37] G. Jungman, M. Kamionkowski, and K. Griest, "Supersymmetric dark matter," *Phys. Rept.* **267** (1996) 195–373, `arXiv:hep-ph/9506380`.

[38] S. R. Coleman and J. Mandula, "All possible symmetries of the S matrix," *Phys. Rev.* **159** (1967) 1251–1256.

[39] R. Haag, J. T. Lopuszanski, and M. Sohnius, "All possible generators of supersymmetries of the S matrix," *Nucl. Phys.* **B88** (1975) 257.

[40] S. P. Martin, "A supersymmetry primer," `arXiv:hep-ph/9709356`.

[41] F. E. Paige, "Supersymmetry signatures at the CERN LHC," `arXiv:hep-ph/9801254`.

[42] A. Hermann, J. Krige, U. Mersits, and D. Pestre, "History of CERN. Vol. 1: Launching the European Organisation for Nuclear Research,". Amsterdam, Netherlands: North-Holland (1987) 600 p.

[43] A. Hermann, J. Krige, U. Mersits, D. Pestre, and L. Weiss, "History of CERN. Vol. 2: Building and running the laboratory, 1954 - 1965,". Amsterdam, Netherlands: North-Holland (1990) 880 p.

[44] e. . Evans, Lyndon and e. . Bryant, Philip, "LHC machine," *JINST* **3** (2008) S08001.

[45] **ALICE** Collaboration, K. Aamodt *et al.*, "The ALICE experiment at the CERN LHC," *JINST* **3** (2008) S08002.

[46] **ATLAS** Collaboration, G. Aad *et al.*, "The ATLAS experiment at the CERN LHC," *JINST* **3** (2008) S08003.

[47] **CMS** Collaboration, R. Adolphi *et al.*, "The CMS experiment at the CERN LHC," *JINST* **3** (2008) S08004.

[48] **LHCb** Collaboration, A. A. Alves *et al.*, "The LHCb detector at the LHC," *JINST* **3** (2008) S08005.

[49] **CMS** Collaboration, G. L. Bayatian *et al.*, "CMS physics: Technical design report,". CERN-LHCC-2006-001.

[50] J. Collins, "Light-cone variables, rapidity and all that," `hep-ph/9705393`.

[51] H. Weyl, "Electron and gravitation," *Z. Phys.* **56** (1929) 330–352.

[52] R. Penrose and W. Rindler, *Spinors and space-time. 1. Two spinor calculus and relativistic fields.* Cambridge Monographs On Mathematical Physics. Cambridge University Press, 1984.

[53] M. Srednicki, *Quantum field theory.* Cambridge University Press, 2007.

[54] G. Sterman and S. Weinberg, "Jets from quantum chromodynamics," *Phys. Rev. Lett.* **39** (1977) 1436.

[55] S. Catani, Y. L. Dokshitzer, M. Olsson, G. Turnock, and B. R. Webber, "New clustering algorithm for multi-jet cross-sections in e+ e- annihilation," *Phys. Lett.* **B269** (1991) 432–438.

[56] S. Catani, Y. L. Dokshitzer, M. H. Seymour, and B. R. Webber, "Longitudinally invariant K(t) clustering algorithms for hadron hadron collisions," *Nucl. Phys.* **B406** (1993) 187–224.

[57] S. D. Ellis and D. E. Soper, "Successive combination jet algorithm for hadron collisions," *Phys.Rev. D* **48** (1993) 3160–3166, `hep-ph/9305266`.

[58] M. Cacciari and G. P. Salam, "Dispelling the N**3 myth for the k(t) jet-finder," *Phys. Lett.* **B641** (2006) 57–61, `arXiv:hep-ph/0512210`.

[59] M. H. Seymour, "Jets in hadron collisions," `hep-ph/0007051`.

[60] B. L. Combridge, J. Kripfganz, and J. Ranft, "Hadron production at large transverse momentum and QCD," *Phys. Lett.* **B70** (1977) 234.

[61] L. Dixon, "Unveiling the structure of amplitudes in gauge theory and gravity." Talk given at the Strings 2008 Conference, CERN.

[62] Z. Kunszt and W. J. Stirling, "Multi - jet cross-sections in hadronic collisions," *Phys. Rev.* **D37** (1988) 2439.

[63] A. van Hameren and R. Kleiss, "Generating qcd-antennas," *Eur.Phys.J.C* **17:611-621,2000** (Eur.Phys.J.C17:611-621,2000) , `hep-ph/0008068`.

[64] S. Catani, "Aspects of QCD, from the Tevatron to the LHC," `arXiv:hep-ph/0005233`.

[65] https://twiki.cern.ch/twiki/bin/view/CMS/SusyPat. Last access on 25.02.1009.

[66] M. Mozer *et al.*, "Description of the CSA07 SUSYBSM Skims." CMS IN-2008/009, 2008.

[67] T. Sjöstrand, L. Lönnblad, and S. Mrenna, "Pythia 6.2 physics and manual," `hep-ph/0108264`.

[68] https://wiki.lepp.cornell.edu/lepp/bin/view/CMS/DatasetInfo. last access on 12. Februar 2009.

[69] U. Gebbert, "Kinematische Analyse von Squark-Zerfällen im vollhadronischen Kanal bei CMS." Diplomarbeit, Universität Hamburg, 2008.

[70] https: //twiki.cern.ch/twiki/bin/view/CMS/GeneratorProduction2007CSA07Signal. Last access on 25.02.2009.

[71] J. M. Campbell, J. W. Huston, and W. J. Stirling, "Hard interactions of quarks and gluons: A primer for LHC physics," *Rept. Prog. Phys.* **70** (2007) 89, `arXiv:hep-ph/0611148`.

[72] Private communication with Prof. Dr. Peter Zerwas.

[73] http://www.phys.psu.edu/~cteq/. Last access on 13. April 2009.

[74] Wolfram Research Mathematica 8.

[75] S. Brandt and H. D. Dahmen, "Axes and scalar measures of two-jet and three-jet events," *Zeit. Phys.* **C1** (1979) 61.

[76] Private communication with Torben Schum.

[77] V. Blobel and E. Lohrmann, *Statistische und numerische Methoden der Datenanalyse.* Teubner Verlag, 1998.

Danksagung

Zuerst möchte ich mich bei Prof. Peter Schleper bedanken, der es mir ermöglicht hat, diese interessante und herausfordernde Diplomarbeit unter seiner Anleitung anzufertigen, und dessen Anregungen und Ideen diese Arbeit sehr bereichert haben. Seine ansteckende Begeisterung für die Teilchenphysik motivierte mich während der gesamten Zeit sehr. Zusätzlich möchte ich mich bei JProf. Johannes Haller bedanken, der sich bereit erklärt hat, den Posten des Zweitkorrektors zu übernehmen.

Ich bedanke mich bei Prof. Peter Zerwas für das Treffen in der netten Atmosphäre und seine Hilfe bei den kniffligen theoretischen Fragen.

Mein ganz besonderer Dank gilt Dr. Christian Autermann und Dr. Christian Sander für die hervorragende Betreuung und für die vielen Hinweise und Ideen, welche diese Arbeit vorangetrieben haben.

Ich danke Torben Schum für die Zusammenarbeit und seine Hilfe bei den schwierigen Fragen des QCD Untergrunds. Ich danke auch Florian Bechtel und Benedikt Mura für die Beantwortung meiner unzähliger Fragen und die Unterstützung bei den Computerproblemen. Allen anderen Mitgliedern der Gruppe danke ich für die angenehme Atmosphäre und große Hilfsbereitschaft.

Ich danke meinen Freunden Stella, Caro, Jan, Philipp, Karsten und Manu, die immer an meiner Seite standen.

Ein ganz besonderer Dank und meine Liebe gilt meiner Freundin Norina für ihre Unterstützung, Geduld und die Hilfe bei den Korrekturen.

Zum Schluss möchte ich mich bei meinen Eltern bedanken, denen ich alles verdanke und die ein so großes Opfer, wie das Verlassen ihrer Heimat, für meine Zukunft gebracht haben.

Erklärung gemäß Diplomprüfungsordnung

Hiermit erkläre ich, dass ich diese Arbeit selbstständig verfasst und außer den angegebenen keine weiteren Quellen und Hilfsmittel verwedet habe. Die Arbeit wurde bisher weder in dieser noch in einer ähnlichen Form einer Prüfungskommission vorgelegt. Mit der Veröffentlichung der Arbeit bin ich einverstanden.

Sergei Bobrovskyi
Hamburg, den 27.03.2009